April 2019

Tissue Equivalent Gellan Gum Gel Materials for Clinical MRI and Radiation Dosimetry

Pawel Brzozowski
The University of Western Ontario

Supervisor
Mequanint, Kibret
The University of Western Ontario

Graduate Program in Biomedical Engineering
A thesis submitted in partial fulfillment of the requirements for the degree in Master of Engineering Science

Abstract

Hydrogels contain high amount of water allowing their use as surrogates to human tissues with specific properties that can be tuned by additives. Gellan gum is a gel-forming material of interest and is a replacement for other common gelling agent with limited use as a tissue phantom. Therefore, this thesis examines the application of gellan gum gels as a novel magnetic resonance imaging (MRI) phantom with a design of experiments model to obtain tunable properties. The analysis was extended to include mechanical and electrical properties with a separate design of experiment. Gels doped with synthesized superparamagnetic iron oxide nanoparticles (SPIONs) and $MnCl_2$ or $GdCl_3$ were scanned using magnetic strengths ranging from 230 µT to 3 T. Nineteen distinct gel samples were formulated determining the linear, quadratic, and interactive effects of each contrast agent by a central composite design of experiments. For mechanical and electrical characterization, the gellan gum gels were doped with LiCl to induce crosslinking and to match the electrical properties of tissues. Additionally, the concentration of gellan gum and propylene glycol (PG) were varied. The models were analyzed with ANOVA and was able to accurately predict the desired properties from the concentration seen by the adjusted R^2 values. Therefore, novel gellan gum gels were prepared with controllable magnetic relaxation, electrical conductivity, and mechanical strength.

Keywords

Tissue equivalent phantoms, hydrogels, gellan gum gels, SPIONs, design of experiments, MRI phantoms, mechanical properties, relative permittivity, electrical conductivity.

Acknowledgment

I would like to thank all those who have supported me during my studies and in my life. Firstly, I want to thank my supervisor Dr. Kibret Mequanint for his continued support and wisdom even when he was travelling. During my time as a graduate student, he has motivated me to work hard and smart to get the most from my studies.

I would like to thank all my lab members who have listened and provided feedback on my research direction and objectives. I especially want to give credit to Dr. Kalin Penev who provided invaluable support and guidance whenever I had questions. His passion and strive for excellence in research motivated me to discover new topics I was once ignorant to.

I would like to thank my advisory committee who gave guidance and constructive criticism to my research. The input and advice gained from the meetings gave me focus on the most prevalent topics and to systematically explore the unknowns in my research.

I also would like to thank Dr. Francisco (Paco) Martinez and Dr. Timothy Scholl at Robarts Imaging who collaborated with me in my first publication and who provided insight and expertise with topics involving MRI. I would like to thank the members in the Department of Chemical and Biochemical Engineering and the School of Biomedical Engineering at Western for providing support throughout my undergraduate and graduate studies. Specifically, I want to thank Dr. Armin Rizkalla for helping on mechanical testing. I want to thank Lyudmil Marinov for his help on the electrical analysis and Dr. Dimitre Karamanev for access to the devices and the space to conduct the dielectric analyses.

I would like to thank everyone at Modus QA for their expertise in medical physics and their warm welcome into their meetings discussing our collaborations.

Lastly, I would like to thank my friends and family who have always supported my endeavours and allowed me to pursue my ambitions. Especial thanks to my parents who have provided a strong foundation for me to build upon, and to my siblings who both challenge and support me while giving me something to aspire.

Table of contents

List of figures

List of tables

List of appendices

List of abbreviations

3D	Three-Dimensional
AC	Alternating current
ANOVA	Analysis of variance
BNC	Bisnitrotetrazolium chloride
DoE	Design of experiment
DTPA	Diethylenetriaminepentaacetic acid
EPR	Electron paramagnetic resonance
gn	Gellan gum
Gy	Gray
Hz	Hertz
MBtPFP	3-(6-methoxybenzothiazol-2-yl)-5-phenyl-2-(3-trifluoromethylphenyl) tetrazol-3-ium chloride
min	Minutes
MRI	Magnetic resonance imaging
NMR	Nuclear magnetic resonance
NMRD	Nuclear magnetic relaxation dispersion
Pa	Pascal
PG	Propylene glycol
R_1	Longitudinal relaxation rate
R_2	Transverse relaxation rate
ROI	Region of interest
rad	Radians
s	Seconds
S	Siemens
SBM	Solomon-Bloembergen-Morgan
SPION	Superparamagnetic iron oxide nanoparticle
T	Tesla
T_1	Longitudinal relaxation time

T_2	Transverse relaxation time
TEM	Transmission electron microscope
TMA	Tetramethylammonium
v/v	Volume per volume
VSM	Vibrating sample magnetometer
w/v	Weight per volume
XRD	X-ray diffraction dispersion
ZFS	Zero-field splitting

Chapter 1

1 Introduction

1.1 Overview

The main concepts discussed in the thesis are introduced in the following chapter. This includes discussing the use of hydrogels as a tissue mimicking material to study the performance of medical physics devices and treatment procedures. Gellan gum gels are introduced and are compared to other gelling agents. The uses of phantoms for medical physics applications, including those in magnetic resonance imaging (MRI), are discussed. Then, the use of mathematical models derived from multifactorial design of experiments characterizing the effect of the composition of a phantom on its properties is described. Finally, the motivations of the work are presented with potential applications.

1.2 Hydrogels as tissue equivalent materials

Tissue-mimicking or tissue equivalent materials are commonly used to evaluate the effectiveness and performance of medical procedures including medical imaging and treatments. For example, advancements in imaging techniques have allowed clinicians the ability to more accurately measure and diagnose patients leading to more effective and directed treatments, but these techniques need to be evaluated prior to ensure quality assurance (QA) of the patient and device [1]. Tissue mimicking materials allow the quality assurance of the procedure without adding harm or discomfort to patients. Here, quality assurance refers to any process that can provide a required level of performance of a given procedure before a patient is subjected to it. By contrast, quality control may be required in some procedures after the treatment or imaging procedure. The use of cadaver or animal tissues for QA presents ethical and practical problems, associated with sourcing, storage, spoilage and disposal of medical waste [2]. This would only exacerbate the already high costs and stringent time constraints associated with the evaluation of medical devices, including MRI [3]. By contrast, tissue mimicking materials can be prepared from a variety of materials solving most of the issues associated with the use of real tissues [4]. These tissue equivalent materials are often referred to as tissue phantoms and are useful in calibration, testing of operators, defining new procedures, and evaluating existing procedures [5]. Many soft tissues contain a high-

water content requiring the corresponding phantoms to also contain or mimic the properties of water. Hydrogels, which are comprised of a hydrophilic polymer matrix dispersed in water, may act as a phantom. Such polymer-water system can generally exist in two forms: in a free-flowing *sol* or in a semi-rigid *gel* structure, in which the polymer matrix preserves a three-dimensional (3D) structure without precipitating from solution and while retaining high water concentrations. The properties of hydrogels are similar to water allowing their use as a basis for many soft tissue phantoms. Hydrogels may be formed by a wide range of gelling agents and additives allowing for a variety of soft tissues to be mimicked [6]. The amount of gelling agent and water content, the presence of a co-solvent, crosslinking agents, and other additives may be used to enhance and control the properties to match those of a desired tissue. Gellan gum is a gelling agents which was developed as an alternative to gelatin and agar in the pharmaceutical industry and has applications in the food industry [7]. Gellan gum is an anionic polysaccharide produced from the microbe *Sphingomonas elodea* (formerly *Pseudomonas elodea*) [8]. Gellan gum is able to form transparent to translucent gels with high water content, good thermal stability, large range of mechanical properties, and simple preparations [9].

1.3 Tissue phantoms in medical physics

The requirements for any tissue phantom depend on the procedure; therefore, a single phantom cannot generally be used for all purposes. If used in MRI, the magnetic properties of the proton dipoles need to be controlled. In addition, the gel compressive modulus and electrical conductivity may also be of specific interest. Outside of imaging, hydrogels have additional application as a tissue equivalent material in radiation therapy as *dosimeters*. Dosimeters are devices used to measure the total ionizing radiation dose delivered. Our group has previously studied gellan gum hydrogels as tissue equivalent materials with the addition of dose sensitive additives [10,11]. The thesis focuses on the MRI application of similar phantoms which may have future benefit with the combination of both MRI and radiation therapy in MRI-guided radiation therapy. Due to the high water content of the hydrogels, their intrinsic MRI properties are similar to liquid water which differs from most soft tissues. Therefore, to mimic the tissue properties, MRI contrast agents are added to hydrogel phantoms. To efficiently determine the effect of the contrast agents, a multifactorial design of experiments is implemented relating concentration to magnetic properties. This allowed the effects to be modeled in a mathematical equation allowing for tunable MRI properties, or more precisely proton relaxation times (as explained in Chapter 2.2.1 of this thesis).

Whenever a magnetic wave is generated, an electrical wave is also generated orthogonally to the magnetic wave and travelling in the same direction. Therefore, the phantoms electrical properties in an MRI scanner can be an important factor influencing image quality. Additionally, having tissue equivalent electrical properties of phantoms is of interest in other applications such as induced hyperthermia in cancer treatment [12,13], gel capacitors [14], soft robots [15], stretchable ionic conductors [16], liquid separation [17], and electromechanical actuators [18]. The conductivity of most soft tissue is due to the presence of electrolytes. To properly model this phenomenon, salts of monovalent cations were tested in the gellan gum gels. As the mechanical integrity of the hydrogels will vary with composition, mechanical properties were also examined. The mechanical tests were focused on blunt impacts that a phantom may experience in use or transport. Having tunable mechanical properties has further applications in ultrasound imaging where gellan gum phantoms were used and in magnetic resonance elastography [9,19]. Therefore, an additional multifactorial design of experiments was used to model both the electrical and mechanical properties of the hydrogel to the concentration of the additives and gelling agent concentration, in order to better match tissue and have tunable properties.

1.4 Motivation and background/scope

Due to their water content and tunable properties, hydrogels have the potential to mimic tissue in a variety of disciplines by optimizing additive concentrations. To account for the addition of various additives, mathematical models can be built to quantify the effects and to have tunable properties fitting various tissues. Gellan gum's high-water content, thermal stability, optical clarity, low cost, ready availability, and simple preparation are of great interest for hydrogels as tissue mimicking materials.

The main goal of this thesis was to investigate gellan gum materials as tissue mimicking MRI phantoms. Tunable properties were developed to cover a wide range of soft tissues. The mechanical and electrical properties of the hydrogel were also studied as the mechanical properties affect the durability of the phantoms to be scanned repeatedly and electrical properties affects how the electromagnetic fields will permeate through the hydrogel medium during MRI. The properties of the gel were modified with the addition of various additives and the gels concentration itself in order to characterize the mechanical and electrical behaviour of the gels.

Chapter 2 of the thesis covers a literature review of hydrogels as tissue-mimicking phantoms for magnetic, mechanical, and electrical properties and includes some background on their analysis. Chapter 3 focuses on the results of the MRI studies conducted that was published in the *Magnetic Resonance Imaging* journal. Chapter 4 contains the results for the electrical and mechanical studies with a further design of experiments. Lastly, Chapter 5 concludes on the main results of the thesis and discusses future work.

1.5 Bibliography

[1] Ihalainen TM, Lönnroth NT, Peltonen JI, Uusi-Simola JK, Timonen MH, Kuusela LJ, et al. MRI quality assurance using the ACR phantom in a multi-unit imaging center. Acta Oncol (Madr) 2011;50:966–72. doi:10.3109/0284186X.2011.582515.

[2] Balcombe J. The use of animals in higher education: problems, alternatives, & recommendations. Washington, DC: Humane Society Press; 2000.

[3] Chen CC, Wan YL, Wai YY, Liu HL. Quality assurance of clinical MRI scanners using ACR MRI phantom: Preliminary results. J Digit Imaging 2004;17:279–84. doi:10.1007/s10278-004-1023-5.

[4] Culjat MO, Goldenberg D, Tewari P, Singh RS. A review of tissue substitutes for ultrasound imaging. Ultrasound Med Biol 2010;36:861–73. doi:10.1016/j.ultrasmedbio.2010.02.012.

[5] Ohno S, Kato H, Harimoto T, Ikemoto Y, Yoshitomi K, Kadohisa S, et al. Production of a Human-Tissue-Equivalent MRI Phantom: Optimization of Material Heating. Magn Reson Med Sci 2008;7:131–40. doi:JST.JSTAGE/mrms/7.131 [pii].

[6] Hoffman AS. Hydrogels for biomedical applications. Adv Drug Deliv Rev 2012;64:18–23. doi:10.1016/j.addr.2012.09.010.

[7] Bajaj IB, Survase SA, Saudagar PS, Singhal RS. Gellan gum: Fermentative production, downstream processing and applications. Food Technol Biotechnol 2007;45:341–54.

[8] Mao R, Tang J, Swanson BG. Texture properties of high and low acyl mixed gellan gels. Carbohydr Polym 2000;41:331–8. doi:10.1016/S0144-8617(99)00108-3.

[9] Chen RK, Shih AJ. Multi-modality gellan gum-based tissue-mimicking phantom with targeted mechanical, electrical, and thermal properties. Phys Med Biol 2013;58:5511–25. doi:10.1088/0031-9155/58/16/5511.

[10] Penev KI, Wang M, Mequanint K. Tetrazolium salt monomers for gel dosimetry I: Principles. J Phys Conf Ser 2017;847. doi:10.1088/1742-6596/847/1/012048.

[11] Penev KI, Mequanint K. Multifactorial study and kinetics of signal development in ferrous-methylthymol blue-gelatin gel dosimeters. Med Phys 2017;44:1948–57. doi:10.1002/mp.12201.

[12] Ma M, Zhang Y, Gu N. Estimation the tumor temperature in magnetic nanoparticle hyperthermia by infrared thermography: Phantom and numerical studies. J Therm Biol 2018;76:89–94. doi:10.1016/j.jtherbio.2018.07.004.

[13] Cheng B, Chatzinoff Y, Szczepanski D, Bing C, Shaikh S, Wyman O, et al. Remote acoustic sensing as a safety mechanism during exposure of metal implants to alternating magnetic fields. PLoS One 2018;13. doi:10.1371/journal.pone.0197380.

[14] Han Y, Shen M, Zhu J, Wu Y, Zhang X. Preparation and capacitive performances of PEDOT/indigo carmine composite hydrogel. Polym Compos 2013;34:989–96. doi:10.1002/pc.

[15] Bauer S, Bauer-Gogonea S, Graz I, Kaltenbrunner M, Keplinger C, Schwödiauer R. 25th anniversary article: A soft future: From robots and sensor skin to energy harvesters. Adv Mater 2014;26:149–62. doi:10.1002/adma.201303349.

[16] Keplinger C, Sun J-Y, Foo CC, Rothemund P, Whitesides GM, Suo Z. Stretchable, transparent, ionic conductors. Science 2013;341:984–7.

[17] Teng C, Lu X, Ren G, Zhu Y, Wan M, Jiang L. Underwater Self-Cleaning PEDOT-PSS Hydrogel Mesh for Effective Separation of Corrosive and Hot Oil/Water Mixtures. Adv Mater Interfaces 2014;1:1–5. doi:10.1002/admi.201400099.

[18] Aouada FA, Guilherme MR, Campese GM, Girotto EM, Rubira AF, Muniz EC. Electrochemical and mechanical properties of hydrogels based on conductive poly(3,4-ethylene dioxythiophene)/poly(styrenesulfonate) and PAAm. Polym Test 2006;25:158–65. doi:10.1016/j.polymertesting.2005.11.005.

[19] Troia A, Cuccaro R, Schiavi A. Independent tuning of acoustic and mechanical properties of phantoms for biomedical applications of ultrasound Independent tuning of acoustic and mechanical properties of phantoms for biomedical applications of ultrasound. Biomed Phys Eng Express 2017.

Chapter 2

2 Literature review

2.1 Overview

A review of current literature on tissue-equivalent materials is presented. The principles behind MRI imaging is provided with a review of MRI phantoms, including gels and MRI contrast agents. The theory associated with the use of contrast agents is explained. The concepts for electrical and mechanical measurements of the phantoms are introduced and how the electrical and mechanical properties impact the phantoms use is discussed. The design of experiments to obtain tunable properties is also discussed.

2.2 Hydrogels as tissue mimicking materials

Different tissue mimicking gels are often prepared from either polysaccharides and proteins (e.g. agarose, and gelatin) or synthetic materials such as polyvinyl alcohol (PVA) [1]. Biopolymers such as polysaccharides are produced by living organisms and often contain secondary or tertiary structures from folding (e.g. extensive hydrogen bonding and supramolecular structure) [2]. However, the properties of biopolymers can vary between batches depending on their preparation conditions and are more difficult to predictably control [3]. Biopolymers are also subjected to microbial growth requiring antimicrobial agents to sustain long-time use. In general, synthetic gelling agents allow for a greater degree of control on properties, allow for a greater flexibility in their synthesis, and do not promote microbial growth, but lack some features (e.g. stable gel formation at low concentration and optical clarity). Gellan gum, produced from *Sphingomonas elodea* (formerly *Pseudomonas elodea*) [4] is an anionic polysaccharide biopolymer consisting of four repeating units of β-D-glucose in positions 1 and 3, β-D-glucuronic acid in position 2 and α-L-rhamnose in position 4. Hydrogel structure is formed during cooling of a gellan gum solution and is caused by aggregation. A thermally reversible random ordering from a single-stranded coil to a double helix transition occurs and further aggregation of the double helical molecules leads to junction zones of the structure [5]. The transition at low gel concentrations is ionotropic and therefore the presence of cations is required for the formation of stable hydrogels as the helix aggregation and network formation are induced by the presence of cations. Therefore, the gelation

properties are related to the nature of the cations with divalent cations allowing stronger gels than monovalent from the additional binding between pairs of carboxyl groups on neighboring helices [6]. Gellan gum can be further categorized into two types corresponding to the amount of acyl functional groups, as seen in Figure 2-1.

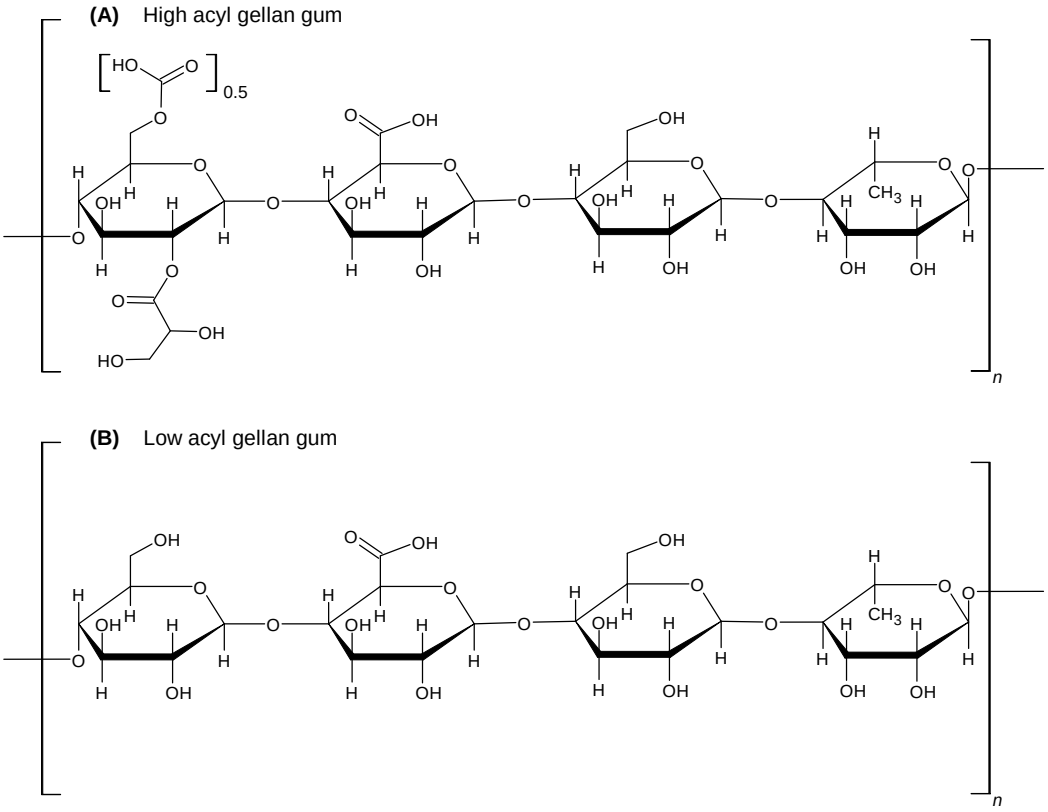

Figure 2-1 The chemical structure of high acyl gellan gum (A) and low acyl gellan gum (B)

When produced, the gellan gum contains a high concentration of acyl functional groups. With an alkali treatment, the acyl groups are hydrolyzed and the gellan gum is deacetylated to form the low acyl variety. High acyl gellan gum forms translucent gels, produces a sol at higher temperatures and the increase acyl groups hinder the packing and associations between chains making the gels weaker [4]. Low acyl gellan gum forms transparent gels and dissolves in deionized water at 90 ºC. Therefore, due to the tissue equivalency, high water content, high gelling efficiency, strength range, and transparency, low acyl gellan gum gels [7] were chosen to be modified as a tissue phantom in this work. Gellan gum has been used as a tissue mimicking phantom in research for

other modalities [8–12]. However, gellan gums use as a tissue mimicking phantom for MRI applications is limited.

2.2.1 Magnetic resonance imaging (MRI) principles

Due to its non-invasive nature, absence of ionizing radiation, and high tissue contrast, magnetic resonance imaging (MRI) is a major diagnostic tool, aiding clinicians in both disease diagnosis and patient treatment planning. MRI signal is generated from the induced voltage by internal radiofrequency coils that detect the shift in the magnetic moments of atomic nuclei. Atomic nuclei consist of nucleons (protons and neutrons), and all nucleons have an intrinsic spin. If the nuclei contains an odd number of either protons and/or neutrons, then the nuclear spin is greater than 0 which induces a weak magnetic moment, whereas if there is an even number of both protons and neutrons the total spin will be equal to 0. Any nucleus with a non-zero spin subjected to a magnetic field at a strength of **B** will have a precession of its magnetic moment at a frequency *f*, known as the Larmor frequency (2-1).

$$f = \frac{\gamma}{2\pi} B \qquad (2\text{-}1)$$

Where γ is the gyromagnetic ratio, specific to that nucleus.

Due to the high-water content and since each water molecule contains two hydrogen atoms, the ^{1}H nuclei (protons) are targeted in many MRI scanners. Protons have a gyromagnetic ratio of 42.576 MHz/T. Under a strong magnetic field, some protons will orient parallel to the main magnetic field with a minor contingency aligning antiparallel to the main magnetic field (dependent on the magnetic field strength and temperature) and will reach a state of thermal equilibrium with its environment. In this thermal equilibrium state, the protons will have a precession around the main magnetic field at the Larmor frequency out of phase from another such that their total magnetic field is aligned in plane with the main magnetic field and no net magnetic component exists for the transverse plane. Addition of a second applied magnetic field at the proton's Larmor frequency will perturb each proton's spin tilting the proton's magnetic moment away from the net magnetic field and into the transverse plane, causing the proton to precess coherently. When the applied magnetic field is released, the proton's magnetic moment will return and align with the main magnetic field out of phase. This applied magnetic field duration is an important factor in the reorientation time of the protons and is often delivered in short pulses. The applied magnetic field

is provided by a radiofrequency pulse from radiofrequency coils housed within the MRI device. The time required for reorientation of the proton with the main magnetic field to the thermal equilibrium state after the radiofrequency pulse is referred to as the relaxation time with both the longitudinal (in the plane of the main magnetic field) and transverse (in the orthogonal plane to the main magnetic field) differing. The longitudinal relaxation times are also referred to as the spin-lattice relaxation time, thermal relaxation or T_1, where the protons magnetic moment is increasing to its thermal equilibrium state by its interaction with the environment. The transverse relaxation times also referred to as the spin-spin relaxation time or T_2 differs from T_1 as the proton's transverse magnetic moment decreases to zero after the radiofrequency pulse, due to interactions with other protons in the surrounding environment. The relaxation times are graphically defined as first-order constants in an exponential growth or decay and occur for T_1 when the net magnetization returns to approximately 63% [(e – 1)/e] of its thermal equilibrium value and for T_2 occurs when the induced magnetic moment is reduced to by approximately 37% (1/e), as seen in Figure 2-2. The different relaxation times between tissues enables a difference in signal intensity and contrast in the final image. A tissue with longer relaxation time will return to a lower magnetic moment compared to tissues with shorter T_1 relaxation times during the same timeframe. This magnetic moment differences allow the MRI device to generate an image showcasing the different tissues in the final image. Due to the intrinsic difference of T_1 and T_2, short T_1 times create bright images, whereas short T_2 times cause darker images as the magnetic moment degrades faster.

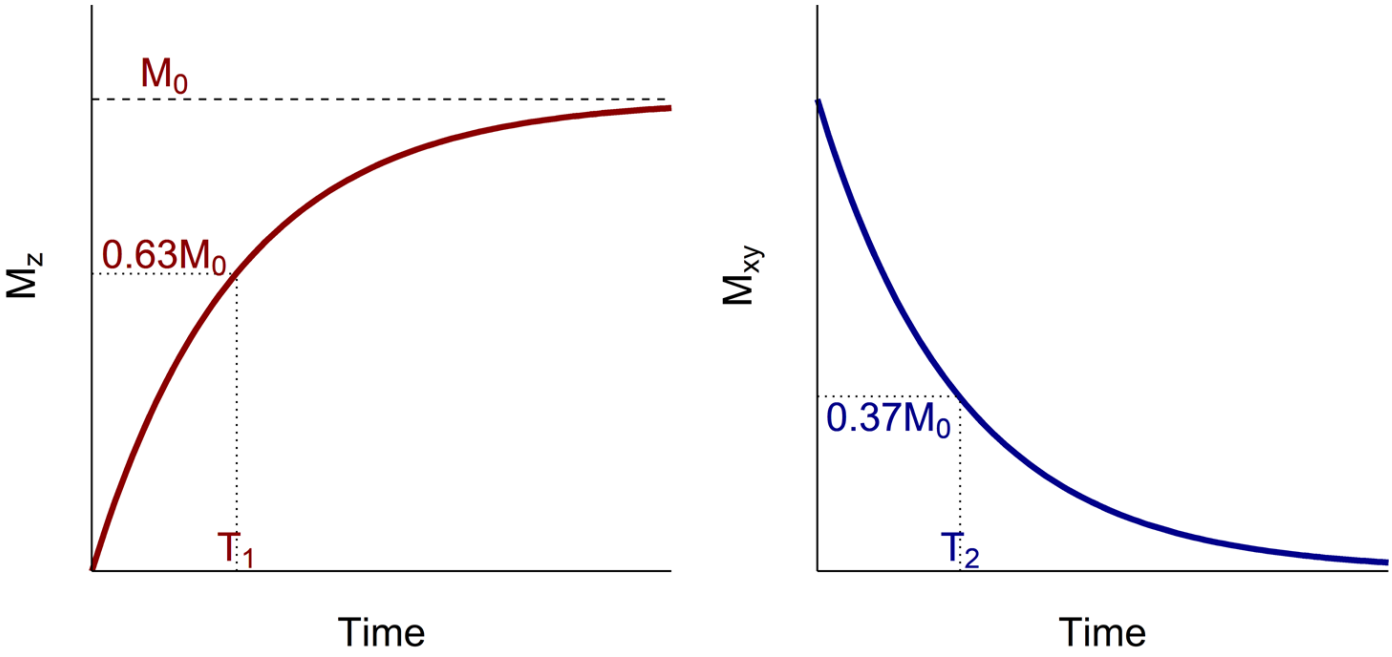

Figure 2-2 Graphical representation of the T_1 and T_2 relaxation times for MRI scans where M_0 is the steady state magnetization at thermal equilibrium, M_z is the value of longitudinal magnetization during relaxation, and M_{xy} is the value of transverse magnetization during relaxation.

Although MRI provides high contrast imaging of tissues without the use of harmful ionizing radiation, it requires complicated and precise imaging parameters. Additionally, MRI scanners have large capital and operating expenses from the device itself, to the duration of scan times requiring trained professionals, and to the limited availability of MRI scans. Therefore, quality assurance is recommended to ensure optimal performance and alleviate the large wait times and operating expenses [13]. Optimal MRI performance occurs when scanning parameters including contrast, signal to noise ratio, spatial resolution, and total scan time are properly controlled [14]. However, differences between manufacturers and imaging conditions create unwanted variations in the final images, especially within a healthcare facility where consistency between scanners is expected [15]. To ensure high image quality and consistency between measurements, as well as for training and research purposes, MRI phantoms are usually employed [16,17]. All of these quality assurance or control techniques can be performed with a tissue equivalent phantom instead of the more risky, varied, and costly human trials. Further enhancements in MRI imaging occur by

new pulse sequences allowing novel and unique images to be generated allowing for new techniques to be developed. To develop new pulse sequences a need to test with a tissue equivalent material exists. Other usage of phantoms includes training of operators, testing equipment, correcting image quality, tuning operational conditions, and in research.

2.2.2 MRI phantoms

MRI phantoms are physical systems that provide near tissue-equivalent MRI signals typically used in calibration and ensuring consistent image quality between MRI scanners. Common requirements for an effective MRI phantom include tissue-equivalent homogenous relaxation times, tissue-equivalent electrical properties, homogeneity, ease of shaping, dimensional stability without reinforcement, simple preparation, low toxicity, and physical, temporal, chemical, and biological stability [17–19]. However, as each tissue within the body is structurally and chemically different, their relaxation times also differ. Furthermore, the pathological health of a tissue and the conditions it is exposed to at the moment of imaging affect its magnetic relaxation properties. Therefore, no one phantom is able to match the properties of all soft tissues and the need for tunable magnetic relaxation times presents itself. Typical MRI phantom materials include aqueous solutions or hydrogels doped with appropriate contrast agents [13]. Doped aqueous solutions have simple preparations, ease of use, long-term stability, and homogeneous properties, but they lack the ability to form and retain shapes, are not tissue equivalent, and are plagued with internal vibrations which, if misused, will generate imaging artifacts. Additionally, the similar T_1 and T_2 relaxation times for aqueous solutions are not tissue equivalent. Doped aqueous solutions are used clinically to calibrate MRI devices due to the homogeneous relaxation properties and their simplicity. By contrast, hydrogels alleviate some of these issues due to quickly diminishing internal vibrations, simple preparations, homogenous properties, ability to retain shape, physical and chemical stability. Previously, synthetic and biopolymer hydrogels have been used as MRI phantoms, including PVA [20,21], gelatin [22], agar [23,24], agarose [25–28], carrageenan [17,29,30], polyacrylamide gels [31], TX-151 [32], carbomer-980 and carbopol-974P [33], with agarose gels being the most common. However, agarose gels is similar to most polysaccharides requiring high-temperature preparation (80-100 ºC) [33], often form trapped bubbles, and are either translucent or opaque due to light scattering. Often, the gelling agent concentration is varied in an attempt to mimic the magnetic properties of tissues, as T_1 and T_2 are affected by the concentration [28]. However, the concentration of agarose also affects the gel integrity and the

relaxation properties creating structural issues when targeting specific tissues relaxation times. Modifying the gelling agent concentration will cause changes to the gel structure, strength, optical transparency, and will adversely affect the consistency of the scans between different concentrations. As a biopolymer, the properties of agarose hydrogels will vary between starting batches expediting the large dependency of relaxation time to gel concentration issue [33]. Additives may be used instead as a means to modify the relaxation properties of the hydrogel.

Gellan gum use as a tissue equivalent material for MRI applications has so far been limited to our publication [34], which is also the subject of this thesis. However, due to gellan gum's beneficial properties, it may be an interesting alternative to agarose and gelatin hydrogels. Gellan gum gels preparation is relatively simple with lower temperatures than other polysaccharides, without the requirements of specialized equipment containing, with no degassing phase or freeze-drying procedure, as in gels based on Tx-151 and PVA respectively. Gellan gum has a high gelling efficiency (low amount of gelling agent forms a gel), high thermal stability, and forms bubble-free and optically transparent to translucent gels. Compared to agarose gels, gellan gum gels show a wider range of mechanical properties that are highly adjustable [35] while having reasonable thermal stability [8,36]. Although gellan gum has been used to form phantom materials that mimic the acoustic and thermal properties of human tissues [8,35,37], its utilization within MRI is limited. With homogenous gel properties, dimensional stability, low cost, thermal stability, safe handling, transparency, simple preparation, tissue equivalence, and potential compatibility with additives, gellan gum could be used as an alternative to fabricate MRI phantoms.

To counteract the long relaxation times in the high-water content hydrogels, the addition of T_1 and T_2-modifiers is needed in hydrogel phantoms. These can include paramagnetic ions and superparamagnetic nanoparticles. Common T_1-modifiers for doped gel phantoms include salts of manganese and gadolinium, such as $MnCl_2$ and $GdCl_3$. Their solubility in aqueous environments allow easy integration to both aqueous and gelled phantoms. Gadolinium-based contrast agents are the most common metal salts used clinically to aid image contrast and as a paramagnetic ion to lower the phantom relaxation times. However, the use of gadolinium raises well-known environmental and health concerns, requiring careful use during handling or disposal [38], so the

metal is usually used in a chelated form [39], commonly with diethylenetriaminepentaacetic acid (DTPA). Unlike gadolinium, manganese is not a heavy metal, lessening its health concerns and environmental impact [40]. Other metal salts include nickel-based or copper-based contrast agents; however, their usage is more limited and nickel salts is a known carcinogen [41]. T_2-modifiers are often added alongside the metal salts to independently adjust both relaxation times. T_2 modification can be achieved by changing the gelling agent concentration [29,30], addition of metal powders [32] or superparamagnetic nanoparticles, such as superparamagnetic iron oxide nanoparticles (SPIONs) [42,43]. By modifying T_2 with the gelling concentration, the material's mechanical integrity will also change meaning that the hydrogel may become too weak or too stiff at certain conditions resulting in inconsistency to the gel's physical properties. The physical properties in these hydrogels would be dependent on the T_2 relaxation times. The addition of metal powders or SPIONs avoids the structural concerns while also providing notable change of the T_2 within the gel. Since SPIONs can be conveniently produced in a repeatable manner using a modified co-precipitation technique [44], they were chosen to modify T_2 relaxation times to ensure consistent hydrogel properties.

Gel stability is a crucial factor for MRI phantoms as they are expected to undergo repeated use, and therefore, must retain physical, chemical and biological stability over an extended period. Ideally, the relaxation times of the phantom will not vary over time [13]. Additionally, temperature shifts may occur during long scan times within the gantry. Large shifts in temperature may affect the gel's integrity which may alter the relaxation properties of the gel causing errors. The relaxivity of the contrast agents is also dependent on temperature further complicating the system [45]. Biopolymer can experience microorganism growth which will cause discrepancies in the scans; therefore, a preserving agent is required. Sodium azide is a powerful antiseptic often used in MRI phantoms; however, it is lethal to humans at moderate concentrations requiring careful consideration when used and disposed of [46]. Other possible antiseptics include methyl 4-hydroxybenzoate (methylparaben) and propylene glycol. Methylparaben is a common antiseptic used in pharmaceuticals and as a preservative in the food industry [47]. Propylene glycol is not directly toxic to microbes but decreases the water activity, and therefore shows antibacterial properties [48]. Additionally, propylene glycol aids in the homogeneity and stability of gellan gum

gels by acting as a co-solvent. MRI scanners are characterized by the size of the gantry and the magnetic field strength induced. Typical clinical scanners range from 0.35 to 3T while research scanners can exceed 7T. However frequency dependency on MRI properties exist for materials including tissues [49]; therefore a unique model is needed for each magnetic field strength to have certain tunable relaxation properties.

2.2.3 Nuclear magnetic relaxation dispersion (NMRD) modelling

In the development of novel contrast agents, often materials are compared based on the magnetic field strength effect on the materials relaxation rates per unit concentration (relaxivity). The dependency of the relaxivity to the magnetic field strengths is referred to as nuclear magnetic relaxation dispersion (NMRD) profiles. The profile is measured at a range of field strengths allowing the molecular dynamics of the contrast agent to be assessed. However, low field strength measurements are coupled with poorer image quality with a decrease in signal to noise ratio. To measure the longitudinal relaxation rates at low field strengths a fast field cycling relaxometer is often employed. These devices operate similarly to conventional scanners with the manipulation of magnetic fields causing the precession and relaxation of nuclei. Briefly, a sample is placed within the device and a magnetic field is applied to polarize the protons boosting signal intensity. The magnetic field is then relaxed to a lower magnetic field causing the sample to begin relaxing, and after a set time the magnetic field is increased to acquire the signal produced from the precessing protons. The duration and magnetic field strength applied during the relaxed state is modified to obtain the longitudinal magnetization as a function of time. The NMRD of a material can then be modelled with non-empirical equations to evaluate the physical parameters governing the material's ability to alter the magnetic environment of a nearby proton. One such model is the Solomon-Bloembergen-Morgan (SBM) theory [50] which fits a mathematical model to parameters relating to the physical relaxation of the inner sphere protons bound to the contrast agent, shown in Figure 2-3. The initial development to relate the relaxation rates in the presence of dissolved paramagnetic ions was developed by Solomon, Bloembergen, and others [51,52]. The equations are divided into the sum of their scalar and dipole coupling of the nuclear and electron spins. Further development occurred relating the feasibility of paramagnetic ions for practical use. However, the joint Solomon-Bloembergen theory was found to be inadequate for describing both longitudinal and transverse relaxivity in aqueous solutions of contrast agents. Therefore,

Bloembergen and Morgan added further theory for the discrepancy with the field dependency to the electron relaxation [52]. For paramagnetic ions with spins greater than ½, the collisions of the water molecules in the inner sphere to the ion leads to distortions of the electron spin levels leading to a transient zero-field splitting (ZFS). Zero-field splitting is the splitting of spin levels in the absence of magnetic field in molecules with more than one unpaired electron. This induces electron relaxation from the changes in the ZFS and their inclusion completes the SBM theory.

SBM theory is based on paramagnetic ions with high symmetry other models are useful with other materials. One example includes the Rosch model for SPIONs [53,54]. R_2 relaxation rates are difficult to measure on fast field-cycling systems and require specialized equipment to measure [55]. The most accurate interpretation of NMRD profiles can only be completed through referencing other information gleaned from additional studies. Two of these tests are electron paramagnetic resonance (EPR) and ^{17}O nuclear magnetic resonance (^{17}O NMR) which can be used to directly obtain parameters important to the protons relaxivity. EPR can provide the transverse electronic relaxation rates and ^{17}O NMR can measure the chemical shifts over a range of magnetic fields and as a function of temperature or pressure, it also enables the estimation of the number of inner-sphere water molecules, the rotational time and the longitudinal electronic relaxation rate [56]. These techniques, while interesting were not used in this thesis as it was deemed that the simpler SBM modelling could provide adequate results.

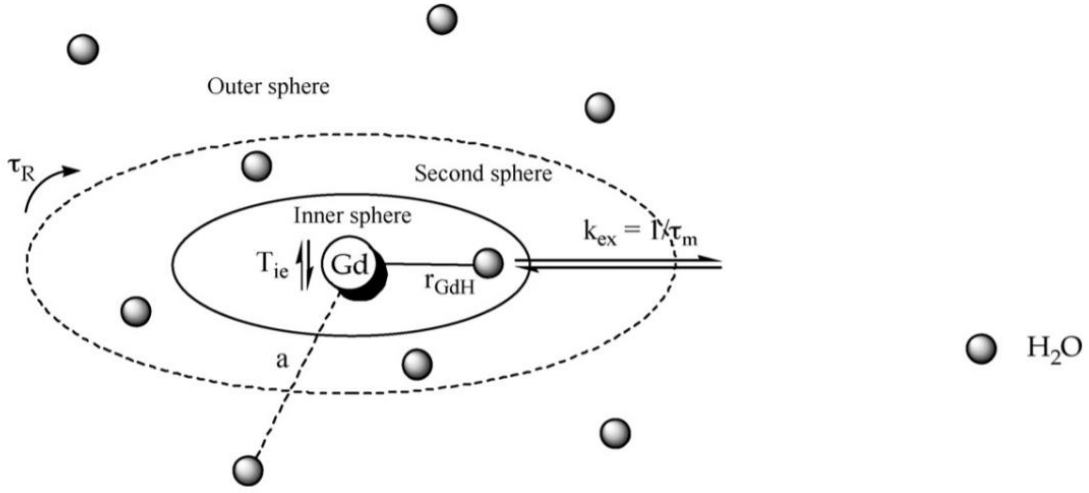

Figure 2-3 Schematic illustration of the parameters in longitudinal relaxation of water protons in the presence of gadolinium. From reference [57] with permission from Elsevier.

However, the model generates problems with paramagnetic ions with low symmetry causing a static ZFS of the electron spin level requiring a more complex form which have been accounted for in other models. In SBM theory outer sphere relaxations are often ignored due to the complex behaviour and requiring empirical parameters that do not relate to the physical parameters of the material. Furthermore, if the correlation time of the inner sphere proton is large compared to the correlation time of the outer sphere proton, the outer sphere can be ignored. Additionally, experimental data has shown that the outer sphere effects can be negligible compared to the inner for gadolinium ions in some complexes but are significant in others [58,59]. Another limitation of the SBM models is that it may not properly model very low magnetic fields and for large slowly rotating compounds [56,60]. The SBM model coefficients are related to the relaxation characteristics of the nearby protons; however limitations exist especially for slowly rotating objects [61]. The following is the SBM theory equations (2-2) determining the relaxivity (r_1 and r_2) of the contrast agent used (M)[58].

$$r_1 = \frac{P_m}{[M]} \frac{q}{T_{1,m} + \tau_m} \qquad (2\text{-}2)$$

Where P_m represents the mole fraction of the contrast agent M, q is the number of inner sphere bounded protons to the contrast agents, $T_{1,m}$ is the longitudinal relaxation times of the bounded

protons found in (2-3), and τ_m represents the fitted water correlation time (the duration of the attachment of a water molecule to the contrast agent).

$$T_{1,m} = C_{DD}\left(\frac{3\tau_{c1}}{1+(\omega_I\tau_{c1})^2}+\frac{7\tau_{c2}}{1+(\omega_S\tau_{c2})^2}\right) + \frac{2}{3}S(S+1)(A_{iso})^2\left(\frac{\tau_e}{1+{\omega_S}^2{\tau_e}^2}\right) \quad (2\text{-}3)$$

Where C_{DD} is a term containing physical constants, which govern the dipole-dipole interactions in τ_{c1} found in (2-4), τ_{c1} and τ_{c2} are the dipolar coupling relaxation correlation times and is a combination of other relaxation times seen in (2-5) and (2-6), ω_I and ω_s represents the angular Larmor frequency of the water protons nuclear spin and the paramagnetic metal electron spin respectively in rad/s and are related by (2-7) and (2-8). *S* is the total electron spin: for gadolinium the value is 7/2 and for manganese the value is 5/2. A_{iso} is the hyperfine coupling constant that can be found in the fitted and is approximately is 37.9×10^6 and 3.9×10^6 rad/s for Mn and Gd-DTPA, respectively [56,62,63], τ_e is the scalar coupling correlation time and is a combination of other relaxation times seen in (2-9).

$$C_{DD} = \frac{2}{15}\frac{{\gamma_I}^2 g^2 {\mu_B}^2}{r_{M-H}^6}\frac{\mu_0}{4\pi}S(S+1) \quad (2\text{-}4)$$

Where γ_1 is the gyromagnetic constant for protons which is 2.675×10^8 ($T^{-1}s^{-1}$), g is the electronic g factor which is 2, μ_B is the Bohr magneton at 9.275×10^{-24} J/T, $r_{M\text{-}H}$ is the distance of the contrast agent to proton bound which may be fitted in the NRMD model by nonlinear fitting but previous results show that for gadolinium the value is approximately 3.13 nm and for manganese the value is approximately 2.9 nm [56,62,63], and μ_0 is the permittivity of free space.

$$\frac{1}{\tau_{c1}} = \frac{1}{T_{1,e}}+\frac{1}{\tau_r}+\frac{1}{\tau_M} \quad (2\text{-}5)$$

$$\frac{1}{\tau_{c2}} = \frac{1}{T_{2,e}}+\frac{1}{\tau_r}+\frac{1}{\tau_M} \quad (2\text{-}6)$$

$$\omega_I = 2\pi f \quad (2\text{-}7)$$

$$\omega_S = 658\omega_I \quad (2\text{-}8)$$

$$\frac{1}{\tau_e} = \frac{1}{T_{2,e}}+\frac{1}{\tau_M} \quad (2\text{-}9)$$

Where τ_r represents the rotational tumbling correlation time which is found in the fitting the NMRD profile with nonlinear fitting, $T_{1,e}$ and $T_{2,e}$ represents the relaxation effectiveness of the paramagnetic centre which are related to the electron relaxation shown in (2-10) and (2-11) respectively.

$$\frac{1}{T_{1,e}} = \frac{{\Delta_t}^2}{5}\left(\frac{\tau_v}{1+{\omega_s}^2{\tau_v}^2} + \frac{4\tau_v}{1+4{\omega_s}^2{\tau_v}^2}\right) \quad (2\text{-}10)$$

$$\frac{1}{T_{2,e}} = \frac{{\Delta_t}^2}{10}\left(3\tau_v + \frac{5\tau_v}{1+{\omega_s}^2{\tau_v}^2} + \frac{2\tau_v}{1+4{\omega_s}^2{\tau_v}^2}\right) \quad (2\text{-}11)$$

Where Δ_t^2 is related to the zero-field splitting magnitude which is found by nonlinear fitting of the NMRD profile and τ_v represents the correlation time of the fluctuations in the ZFS which is also found in the nonlinear fitting of the NMRD profile. With equation (2-2) the equations from (2-3 to 2-11) can be substituted and nonlinear least square fittings can be solved to find the values for the physical quantities of τ_m, A_{iso}, τ_r, τ_v, and Δ_t^2 by the known relaxivity and Larmor frequencies after setting initial conditions.

2.2.4 Electrical properties of tissue equivalent phantom

The electrical properties of hydrogels can be a crucial factor for various phantom types including but not limited to MRI. When a magnetic wave is generated, an electric wave perpendicular and moving in the same direction is also generated. When the electromagnetic wave interacts with tissues, its wavelength is decreased, currents are generated in the tissue, and possible reflection and refraction of the electromagnetic wave at the interfaces of the tissues may occur [64]. The interaction of a material to the electric component in an electromagnetic wave is known as the dielectric effect. This effect can lead to dielectric artifacts that cause a pattern of abnormal bright and dark spots on the MRI image due to the combination of constructive and destructive interference from electric standing waves. Electric standing waves may arise from the electric wave entering at two opposite ends of the anatomic region flowing in the opposite direction causing the constructive (bright spots) and destructive interference (dark spots) at a quarter wavelength apart. To an observer, the interference waves seem to not move in the direction of the wave giving them the name of standing waves similar to those produced in a large tank of water with ripples or in a microwave. It is still unknown to what degree the dielectric effects have on these bright and dark artifacts as the causes and effects of these artifacts in MRI are still not fully

understood. However, these artifacts are more common at high magnetic field strengths as the wavelength for the radiofrequency pulse is decreased. For magnetic field strengths under 1.5 T, the wavelength is larger than the anatomic region imaged, but as the magnetic field strength increases, they become the same size or smaller than the anatomic region imaged. The decrease in wavelength can generate uneven and observable errors in a sample with insufficient conductivity. Soft tissues contain relatively high conductivity compared to pure water due to the electrolyte compositions which also dampens the standing wave phenomena. The concentration of electrolytes differ between tissues and the tissue conditions also varies causing a range of electrical properties in soft tissues. Therefore, to mimic a range of soft tissue electrical properties, tunable electrical properties are needed in the phantoms. That can be fulfilled with hydrogels doped with various concentrations of additives. However, central brightening has been demonstrated in highly conductive phantoms where the dielectric artifacts should be minimal [65]. Due to the complexity and the current unknown mechanism of dielectric artifacts, careful control of dielectric properties should be warranted with MRI phantoms.

Whereas the conductivity in solids is typically due to a flow of electrons and/or holes, liquids tend to have ionic conductivity. Pure water has a very low self-ionization constant (10^{-14}) and is, therefore, an insulator with a resistivity of 18 MΩ cm. More specifically, water is a dielectric: at equilibrium with no electric field the water dipoles are orientated randomly, but if exposed to an electric field the dipoles will turn to reorient to the electric field, shifting their relative position inducing a dipole moment which is called dielectric polarization. Due to their high-water content, hydrogels also tend to be dielectric. The electric properties of a material, including hydrogels, can be determined by dielectric spectroscopy [66] which measures the dielectric properties on an alternating electric field as a function of angular frequency. To quantify the dielectric material property, the relative electric permittivity (also referred to as the dielectric constant) and the conductivity are found. Relative electric permittivity is the ability of a material to store electrical energy of an electrical field by the polarization of the medium. The relative electric permittivity of a material is defined in (2-12) and (2-13).

$$\varepsilon_e = \frac{C}{C_0} \tag{2-12}$$

$$\varepsilon_e = \varepsilon_e' + i\varepsilon_e'' \quad (2\text{-}13)$$

Where,

$$C = \varepsilon_e * \varepsilon_{e,0} * \frac{A}{d} \quad (2\text{-}14)$$

Where C and C_0 are the capacitance when filled with the dielectric material or with free space respectively, $\varepsilon_{e,0}$ is the permittivity of free space at $8.85418782 \times 10^{-12}$ m^{-3} kg^{-1} s^4 A^2, ε_e' and ε_e'' represent the real and imaginary components of the permittivity. The real part of the permittivity is related to the energy storage of the material and is also known as relative permittivity, whereas the imaginary part is related to the energy consumption/dissipation. The permittivity of a material is dependent on the applied frequency [66], where the effects are dominated by distinct phenomenon at differing frequency ranges [67]. The dielectric spectrometer determines the complex permittivity of a material by measuring the complex opposition of current in an alternating current (AC) circuit, also known as the *impedance*. The complex impedance of a dielectric material can be modelled by an equivalent electric circuit design. One such design contains a resistor and capacitor in series (Figure 2-4) such that the equivalent impedance (Z) is defined as (2-15).

$$Z = R_x - \frac{i}{w * \varepsilon_e * X_x} \quad (2\text{-}15)$$

Where the real part is representative of the pure resistance (R_x) of the material which consumes the electrical energy, and the imaginary part is the reactance (X_x) is represented by a capacitor which stores the electrical energy, ω represents the angular frequency measured in rad/s. The response over a range of frequencies is then used to measure the complex impedance (schematic is shown in Figure 2-4). The schematic shows a waveform generator capable of multifrequency is placed in a circuit containing a known resistor **R1** in series with a capacitor cell filled with the dielectric material. The voltage drop across the entire circuit and the capacitor is measured by an

oscilloscope that is phase sensitive. With the two voltages drops known and the phase separation between voltages also known, the equivalent circuit impedance can be calculated.

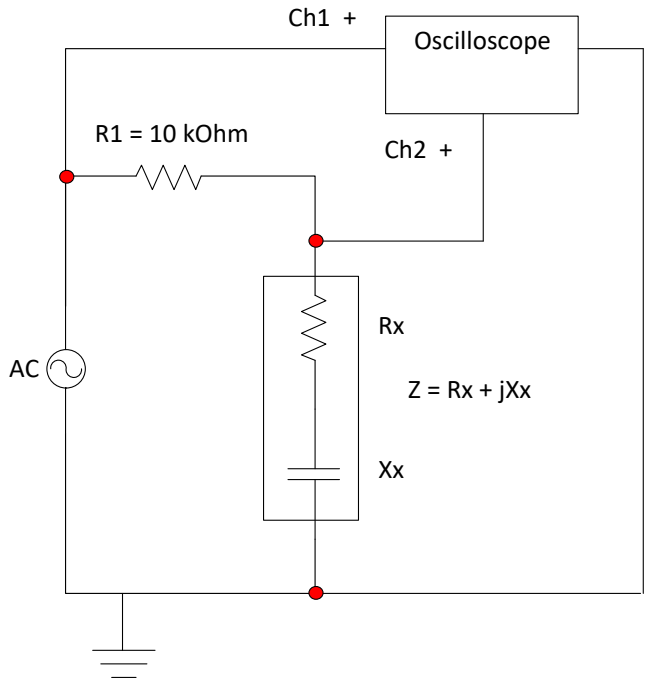

Figure 2-4 Dielectric spectrometer setup with an AC waveform generator in series with a known resistor (R1) and dielectric material (shaded region) measured with an oscilloscope. The materials equivalent circuit design is with both resistance (R_x) and reactance (X_x).

The equivalent circuit calculations shown in Figure 2-5 incorporates the root mean square voltage (V_{rms}) from both channels for the calculations. The V_{rms} of both channels are found from the peak voltage drop across the channels corresponding to V_T for the circuit and V_x for the voltage drop across the dielectric material as shown by equations (2-17) and (2-18). The values are then incorporated into the two sides of a triangle with a separation angle equal to their phase difference (ϕ).

$$V_{rms} = \frac{V_{peak}}{\sqrt{2}} \tag{2-16}$$

$$V_T = \frac{V_{peak,\ ch,1}}{\sqrt{2}} \tag{2-17}$$

$$V_x = \frac{V_{peak,\ ch,2}}{\sqrt{2}} \tag{2-18}$$

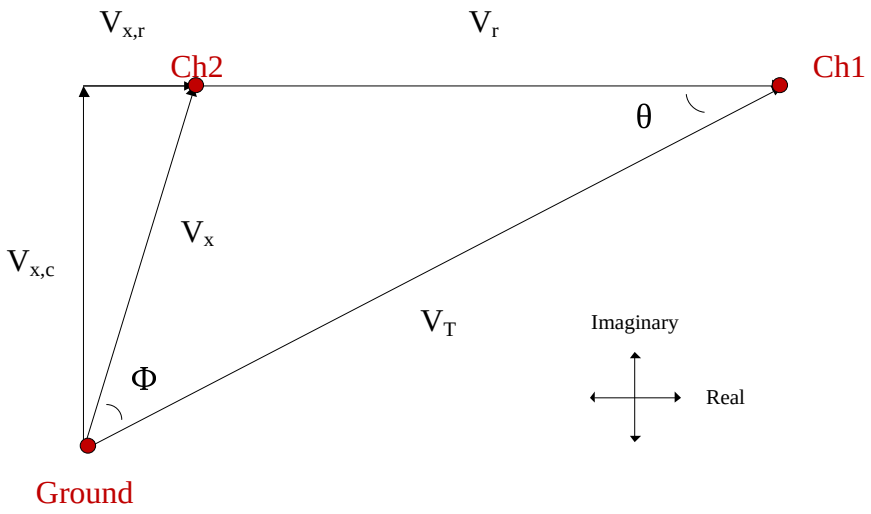

Figure 2-5 Illustration of the equivalent circuit design calculations with voltage represented as side of a triangle in a real-imaginary plane. Channels for the oscilloscope are labeled in red.

Where V_{peak} represents the peak voltage. V_{rms} is the equivalent direct current voltage and its used to evaluate the magnitude of the real and imaginary components to represent the total voltage drop. Applying the cosine law will result in the third triangle side which is the voltage drop across the resistor (2-19).

$$V_r{}^2 = V_T{}^2 + V_x{}^2 - 2 * V_T * V_x * \cos(\phi) \tag{2-19}$$

Where the voltages represent the sides of a triangle. With the voltage across the resistor and the resistance known the current through the circuit is calculated (2-20).

$$I = \frac{V_r}{R1} \tag{2-20}$$

The current (I) for all units is equal and therefore the impedance of the entire circuit (Z_T) can be calculated (2-21).

$$Z_T = \frac{V_T}{I} \tag{2-21}$$

And the impedance of the dielectric material is Z_x in (2-22),

$$Z_x = \frac{V_x}{I} \tag{2-22}$$

The angle θ in Figure 2-5 can also be calculated with the sine law allowing for the equivalent circuit complex impedance to be calculated (2-23).

$$Z_{T,r} = \cos(\theta) * Z_T \tag{2-23}$$

Where $Z_{T,r}$ represents the total real part of the impendence of the entire circuit. Since the exterior resistor (R1) is known the equivalent resistor of the dielectric material ($Z_{x,r}$) is then calculated (2-24).

$$Z_{x,r} = Z_{T,r} - R1 \tag{2-24}$$

The equivalent reactance of the dielectric material ($Z_{x,c}$) is then (2-25)

$${Z_{x,c}}^2 = {Z_{x,T}}^2 - {Z_{x,r}}^2 \tag{2-25}$$

With the equivalent circuit design for the dielectric material known the complex impedance is also known allowing for the calculation of the complex permittivity as a function of angular frequency (2-26).

$$\varepsilon_e(\omega) = \frac{1}{i * w * Z(\omega) * C_0} \tag{2-26}$$

The conductivity of a dielectric material can be found through (2-27)

$$\sigma_e(\omega) = \varepsilon_{e,0} * \varepsilon_e'' * \omega \tag{2-27}$$

Where ε_e" is the imaginary component of the electric permittivity. The dielectric loss tangent or dissipation factor can be found by (2-28) which is related to the electric relaxation time of the material.

$$\mathrm{Tan}(\delta) = \frac{\varepsilon_e'}{\varepsilon_e''} \tag{2-28}$$

The electrodes used to house the dielectric material may be the source of experimental errors due to the polarization of the dielectric material which has been seen in other setups [66]. The electrodes are polarized by an electric field when electric charges accumulate on the interface between two materials referred to as interfacial polarization [68]. Electrode polarization occurs when the charge accumulates at the interface of two electrodes and a dielectric material. If there is an imbalance of mobility of mobile charge carriers such as electrons, holes, or ions the more mobile

charge carrier may accumulate at their opposing electrode. Due to the electrode polarization and the accumulation of charge on the electrode surface, additional electrons may be attracted or repelled increasing the charge causing the permittivity of the material to increase. Sufficient time is required for charge accumulation electrode polarization to occur. Therefore, at lower frequencies polarization of the electrodes becomes more of an issue with an increase apparent permittivity.

2.2.5 Mechanical properties of tissue equivalent phantoms

A phantom should sustain external forces to resist deformation under normal operating conditions including its shipping and handling. Unlike aqueous phantoms, hydrogels may deform, and changes may occur to their properties when subjected to large external force. Additionally, hydrogels should not flow to ensure spatial and temporal stability. Further applications for gellan gum hydrogels include mimicking the mechanical properties of tissues for ultrasound imaging [69] or other applications such as magnetic resonance elastography [70]. As with MRI, ultrasound imaging may benefit from the use of tissue equivalent materials that mimic the viscoelastic properties of a tissue. The deformation of a viscoelastic material contains both a viscous and elastic behavior with mechanical properties that are dependent on the rate of deformation. These properties have been mimicked by hydrogel phantoms with gels formed from gelatin [71], agar [72], and high acyl gellan gum gels [8]. These hydrogels have been shown to show similar viscoelastic behaviour as tissues but require additives to better mimic tissue behaviour.

Gels may experience blunt compressive forces in its general use requiring sufficient strength to absorb the energy without deforming significantly. Similar to most hydrogels, low-acyl gellan gum gels are also viscoelastic with the rate of deformation affecting the mechanical properties [6]. The amount of deformation is indicated by the engineering strain (ε_m) seen in (2-29).

$$\varepsilon_m = \frac{\Delta l}{l} \tag{2-29}$$

Where l and Δl represent the total length of the sample and the deformation of the sample respectively. The engineering stress (σ_m) is measured by the force applied (F_a) divided by the initial cross-sectional area perpendicular to the load (A) of the material (2-30) in units of pressure. The fracture stress occurs when a material reaches maximum stress and fails.

$$\sigma_m = \frac{F_a}{A} \tag{2-30}$$

The compressive modulus of a material is defined by the instantaneous change of stress versus strain of a material in units of pressure. When a material is deformed within its elastic region the compressive modulus of the materials is constant. However, viscoelastic materials are dependent on strain rate and their moduli is determined by taking this into account according to the following equations.

$$E = \frac{\Delta\sigma_s}{\Delta\varepsilon_s} \tag{2-31}$$

$$E(\varepsilon_s) = \frac{d(\sigma_s(\varepsilon_s))}{d(\varepsilon_s)} \tag{2-32}$$

The conditions of the hydrogel during the mechanical characterization tests may dictate the behaviour. These conditions include whether the hydrogel is constrained in its mold or is taken out of the mold for unconstrained compressive analysis or the hydrated state of the hydrogel. During constrained tests, the hydrogel is kept in a container to ensure constant cross-sectional area; however, the results will be influenced by the container walls and the mechanical properties of the container also need to be accounted for. The stress the material faces as the material tends to push onto the container will add mechanical stress seen by the actuator increasing the apparent strength of the gels. For unconstrained gels, as the mechanical load is applied to the sample the material will begin to deform both in direction of load and transversely increasing the cross-sectional area as a function of force. This can lead to errors in the stress value calculated as the instantaneous cross-sectional area changes. The degree of hydration will impact the mechanical properties of a gel as water which helps resists compression. Depending on the state of the hydrogel during its intended use, testing the mechanical properties in the dehydrated state may be more appropriate.

As mentioned, various additives have been used to modify the mechanical properties of the gels. The most apparent method to modify the mechanical integrity of the hydrogels is to modify the concentration of gelling agent or co-gelling agent. The reduction of the gelling agent will reduce the gels mechanical integrity up to a minimum value where the hydrogel structure is unstable and dissolves in the aqueous solution. Additionally, the gel may still flow even in a gel state due to the degradation of mechanical properties meaning temporal instability. However, the increase of

gelling agent will produce a more crosslinked structure that can reduce the optical transmittance of the gel and eventually form inhomogeneities in the gel from uneven gelling. Therefore, the optimal mechanical properties of the gel may not be adequate by varying the gelling agent concentration alone as a gel too weak to form or too strong gaining heterogenous properties may form. Additives for gellan gum phantoms to induce crosslinking are often done with mono- or divalent metal salts [6,73], and the effects are dependent on the nature of the cation with divalent leading to stronger gels. Due to the anionic structure of gellan gum the addition of a cationic ion will induce further aggregation of the order to the double helix gellan gum molecules which stiffen the resulting gel [73].

2.3 Multifactorial design of experiments

Multifactorial design of experiments evaluates the effect of individual compositions to the hydrogels ability to mimic tissue properties and can obtain tunable properties to match various soft tissues. Design of experiment is an effective means to study the effects and interactions of multiple variables. Full factorial designs are the simplest form of designs where a certain number of factors are varied to another certain number of levels [74]. The most basic form of a design of experiment is a 2 factor by 2 level design or 2^2, and where two parameters are varied at two values, seen in Figure 2-6.

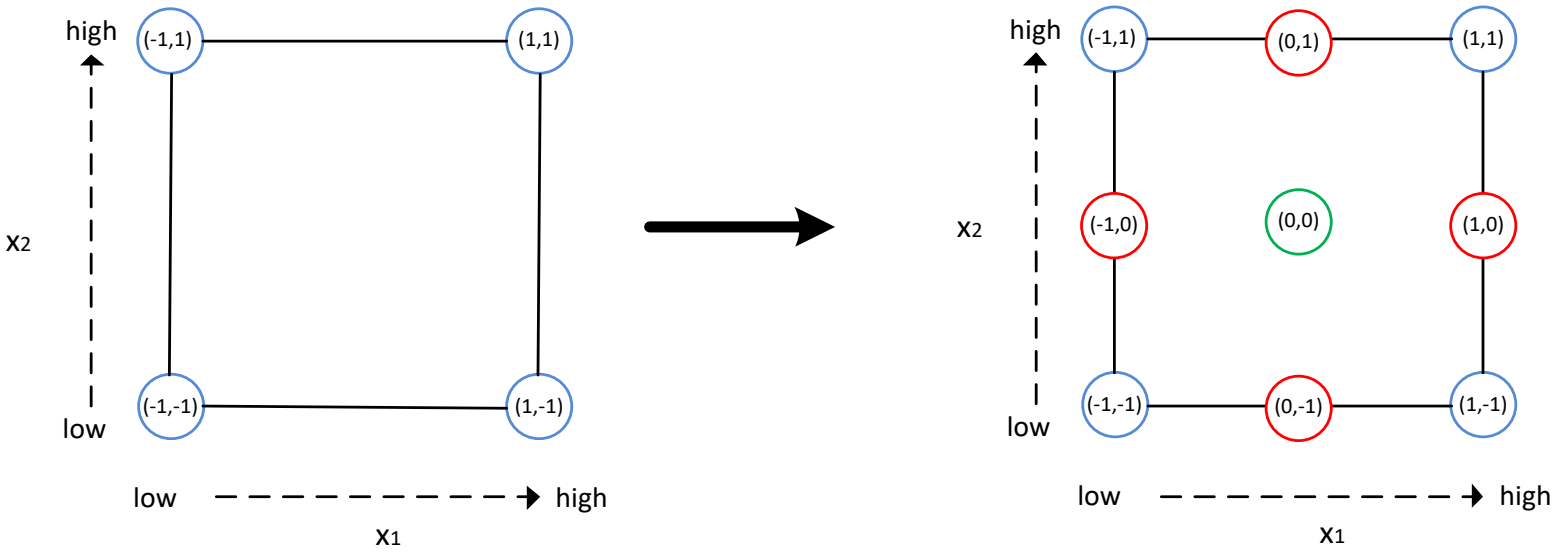

Figure 2-6 Multifactorial design of experiments with a two factor two level (2^2) experiment on the left and a face centred composite design on the right. Blue circles are for 2^2, red for the intermediate points, green for the centre points.

More generally, a multifactorial design is defined as l^k where k is the number of factors and l is the number of values. By comparing the results at each combination, the effect of both parameters and the interaction of the two can be determined and deemed significant or not. The effect of factor A in a 2^k is calculated from the difference in means (Contrast) between the high and low levels of a factor shown in (2-33)

$$Contrast_A = \bar{y}_{A^+} - \bar{y}_{A^-} \tag{2-33}$$

Where $\bar{y}_{A^+}$ is the mean value at the high concentration of A, and $\bar{y}_{A^-}$ is the mean value at the low concentration of A. The interactive effect of factors A and B for a two level two factor design are then defined as (2-34)

$$Contrast_{A:B} = \frac{A^+B^+ + A^-B^-}{2 \cdot n} - \frac{A^+B^- + A^-B^+}{2 \cdot n} \tag{2-34}$$

Where A^+B^+ is the sum of all n repetitions at the high concentrations of both A and B, A^-B^- is the sum of all n repetitions at the low concentrations of both A and B, A^+B^- is the sum of all n repetitions at the high concentrations of A and the low concentration of B, A^-B^+ is the sum of all n repetitions at the low concentrations of A and high concentration of B. However, when translated

into a model, the coefficients are defined as the difference in the marginal mean and the overall mean. Therefore, the $Contrast_A$ is twice the size of the estimated coefficient in the model defined in (2-35) for a 2^2 design, and the relation of contrast to effect is more generally defined as (2-35).

$$y_{A,B} = \beta_0 + \beta_A \cdot x_A + \beta_B \cdot x_B + \beta_{A-B} \cdot x_A \cdot x_B + error_{A,B} \quad (2\text{-}34)$$

$$Effect_A = \beta_A = \frac{1}{2^{k-1} \cdot n} \cdot Contrast_A \quad (2\text{-}35)$$

Where $y_{A,B}$ is the measured response, β_0 is the predicted value when all compositions are zero, β_A, β_B, and β_{A-B} is the model coefficient also referred to as the effect of A, B, and the interaction between A and B respectively, x_A and x_B are the concentration of A and B respectively, and $error_{A,B}$ is the error component between the measured response and treated means indicating the variation not explained by the model. It is assumed that the error follows a normal distribution with a mean of zero. The error component also accounts for any effect not modeled whether insufficient design or an intentional disregard of effect due to low significance. The significances of the effect are determined via ANOVA or a *t*-test which compares the overall effect of the factor over the square root of the estimated variance.

By the addition of intermediate points located between the two current levels a central composite design can be generated allowing for the analysis of the quadratic effect and enhancing the variance calculations. The location and position relative to the design space of the intermediate points, also known as alpha points, determines the type of central composite design. With alpha points equal to 1, the values are located on at the centre edges of the design shown in Figure 2-6 and is called a face centred design. The general central composite design allows for any nonlinear effects to be determined and strengthens the design space analysis. With face centred composite designs, the maximum and minimum conditions set initially are not surpassed which is useful for designs with specific concentration constraints of individual parameters; furthermore, the design is able to accurately predict the conditions set within the entire design space. Additionally, the degree of variation can be accounted for with no or few central points where other designs require many center points. However, as the points are not equal distance from the centre it is not rotatable meaning the variance at each point is not equivalent resulting in less accurate variance calculation. The addition of centre points in the middle of the design aids in the variance calculations and the

calculation of the quadratic effect of each parameter. A linear regression model can be conducted relating the parameters to their effects. ANOVA can be used to determine the significance of each coefficients in the regression model. Once the significance is known, the regression model can be redone with only the significant coefficients.

A design of experiment can be expanded to include multiple factors raising the number of experiments by a degree. Therefore, a two-level three-factor design of experiment (2^3) requires eight compositions for complete analysis seen in Figure 2-7.

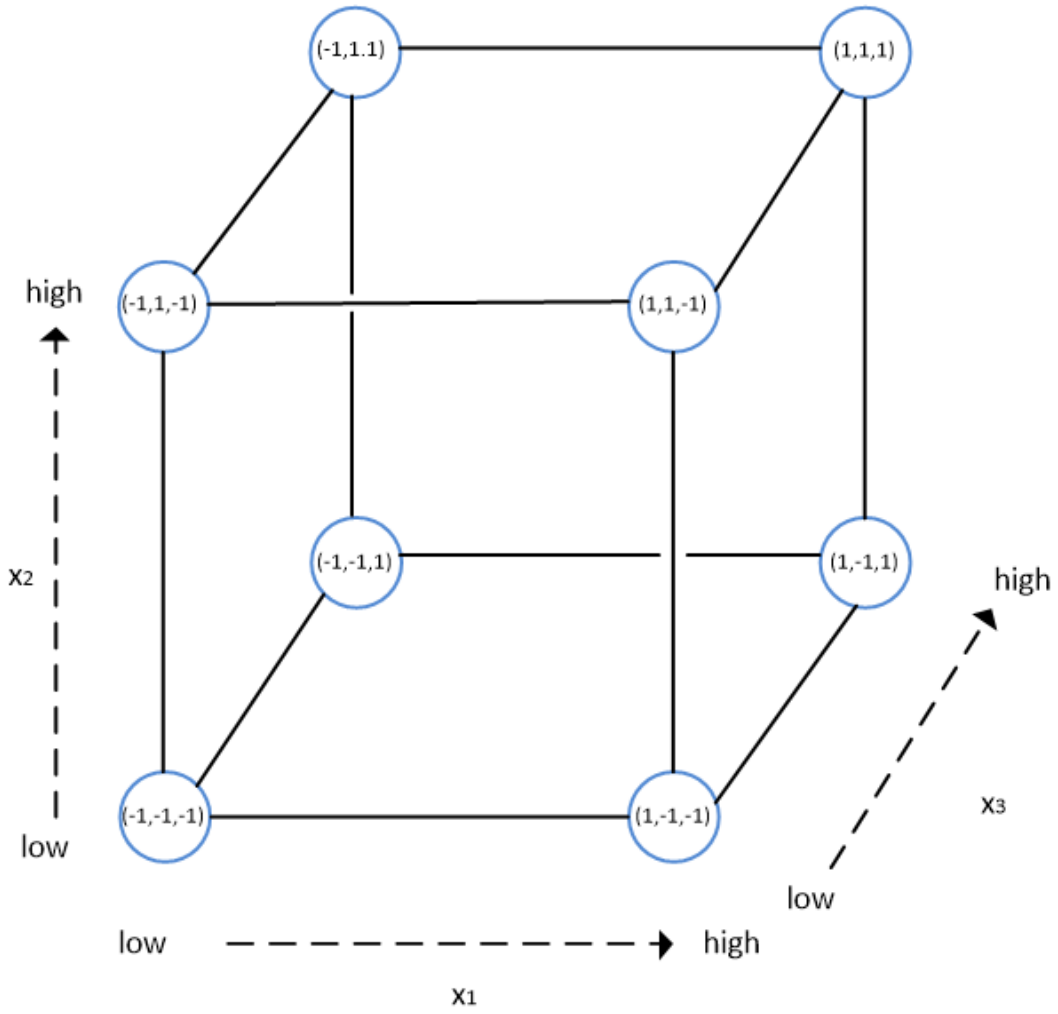

Figure 2-7 Example three factor two level (2^3) design of experiment

As more variables are added the degree increases proportionally requiring a large number of compositions to be tested. The number of repetitions also scales the number of experiments needed, but they increase the accuracy of the variance calculation. Randomizing the compositions lessens the influence of any procedural or experimental errors.

2.4 Summary

In summary this Chapter provided pertinent literature review to the thesis. These topics were: (i) gel-forming materials for MRI phantoms, (ii) MRI imaging principles, (iii) electrical and mechanical properties of gels, and (iv) design of experiments. While the information provided in this Chapter is not comprehensive, an effort was made to ensure that seminal works and significant research findings were included with minimal bias.

2.5 Bibliography

[1] Hoffman AS. Hydrogels for biomedical applications. Adv Drug Deliv Rev 2012;64:18–23. doi:10.1016/j.addr.2012.09.010.

[2] Stupp SI, Braun P V. Molecular Manipulation of Microstructures: Biomaterials, Ceramics, and Semiconductors. Science 2011;277:1242–8.

[3] Patel PK, King CR, Feldman SR. Biologics and biosimilars. J Dermatolog Treat 2015;26:299–302. doi:10.3109/09546634.2015.1054782.

[4] Mao R, Tang J, Swanson BG. Texture properties of high and low acyl mixed gellan gels. Carbohydr Polym 2000;41:331–8. doi:10.1016/S0144-8617(99)00108-3.

[5] Coutinho DF, Sant S V., Shin H, Oliveira JT, Gomes ME, Neves NM, et al. Modified Gellan Gum hydrogels with tunable physical and mechanical properties. Biomaterials 2010;31:7494–502. doi:10.1016/j.biomaterials.2010.06.035.

[6] Miyoshi E, Takaya T, Nishinari K. Rheological and thermal studies of gel-sol transition in gellan gum aqueous solutions. Carbohydr Polym 1996;30:109–19. doi:10.1016/S0144-8617(96)00093-8.

[7] Paulsson M, Hägerström H, Edsman K. Rheological studies of the gelation of deacetylated gellan gum (Gelrite(®)) in physiological conditions. Eur J Pharm Sci 1999;9:99–105. doi:10.1016/S0928-0987(99)00051-2.

[8] Chen RK, Shih AJ. Multi-modality gellan gum-based tissue-mimicking phantom with targeted mechanical, electrical, and thermal properties. Phys Med Biol 2013;58:5511–25. doi:10.1088/0031-9155/58/16/5511.

[9] Hiroki A, Sato Y, Nagasawa N, Ohta A, Seito H, Yamabayashi H, et al. Preparation of polymer gel dosimeters based on less toxic monomers and gellan gum. Phys Med Biol 2013;58:7131–41. doi:10.1088/0031-9155/58/20/7131.

[10] Warren H, Gately RD, O'Brien P, Gorkin R, In Het Panhuis M. Electrical conductivity, impedance, and percolation behavior of carbon nanofiber and carbon nanotube containing gellan gum hydrogels. J Polym Sci Part B Polym Phys 2014;52:864–71. doi:10.1002/polb.23497.

[11] Ascención Y, Dietrich J, Mequanint K, Penev KI. Tetrazolium salt monomers for gel dosimetry II: Dosimetric characterization of the ClearView^{TM} 3D dosimeter. J Phys Conf Ser 2017;847. doi:10.1088/1742-6596/847/1/012049.

[12] Shungu D, Valiant M, Tutlane V. GELRITE as an agar substitute in bacteriological media. Appl Environ Microbiol 1983;46:840–5.

[13] Keenan KE, Ainslie M, Barker AJ, Boss MA, Cecil KM, Charles C, et al. Quantitative magnetic resonance imaging phantoms: A review and the need for a system phantom. Magn Reson Med 2018;79:48–61. doi:10.1002/mrm.26982.

[14] In E, Naguib HE, Haider M. Fabrication and characterization of polymer gel for MRI phantom with embedded lesion particles. Proc SPIE - Int Soc Opt Eng 2012;8348. doi:10.1117/12.915034.

[15] Schnack HG, Van Haren NEM, Hulshoff Pol HE, Picchioni M, Weisbrod M, Sauer H, et al. Reliability of brain volumes from multicenter MRI acquisition: A calibration study. Hum Brain Mapp 2004;22:312–20. doi:10.1002/hbm.20040.

[16] IEC 60601–2-33:2010, Medical Electrical Equipment – Part 2–33: Particular requirements for the basic safety and essential 398 W.T. Sobol performance of magnetic resonance equipment for medical diagnosis. International Standard, Edition 3.0. n.d.

[17] Kato H, Kuroda M, Yoshimura K, Yoshida A, Hanamoto K, Kawasaki S, et al. Composition of MRI phantom equivalent to human tissues. Med Phys 2005;32:3199–208. doi:10.1118/1.2047807.

[18] Price RR, Axel L, Morgan T, Newman R, Perman W, Schneiders N, et al. Quality assurance methods and phantoms for magnetic resonance imaging: report of AAPM nuclear magnetic resonance Task Group No. 1. Med Phys 1990;17:287–95.

[19] Chen CC, Wan YL, Wai YY, Liu HL. Quality assurance of clinical MRI scanners using ACR MRI phantom: Preliminary results. J Digit Imaging 2004;17:279–84. doi:10.1007/s10278-004-1023-5.

[20] Gordon MJ, Chu KC, Margaritis A, Martin AJ, Ethier CR, Rutt BK. Measurement of Gd-DTPA diffusion through PVA hydrogel using a novel magnetic resonance imaging method. Biotechnol Bioeng 1999;65:459–67. doi:10.1002/(SICI)1097-0290(19991120)65:4<459::AID-BIT10>3.0.CO;2-O.

[21] Chu KC, Rutt BK. Polyvinyl alcohol cryogel an ideal phantom material for MR studies of arterial flow and elasticity. Magn Reson Med 1997;37:314–9.

[22] Blechinger JC, Madsen EL, Frank. GR. Tissue-mimicking gelatin–agar gels for use in magnetic resonance imaging phantoms. Med Phys 1988;15:629–36.

[23] Kamel H, Syms RRA, Kardoulaki EM, Rea M. Surgical wound monitoring by MRI with a metamaterial-based implanted local coil. EPJ Appl Metamaterials 2018;5:1–7.

[24] Bucciolini M, Ciraolo L, Lehmann B. Simulation of biological tissues by using agar gels at magnetic resonance imaging. Acta Radiol 1989;30:667–9. doi:10.3109/02841858909174735.

[25] Gossuin Y, Burtea C, Monseux A, Toubeau G, Roch A, Muller RN, et al. Ferritin-induced relaxation in tissues: An in vitro study. J Magn Reson Imaging 2004;20:690–6. doi:10.1002/jmri.20152.

[26] Mitchell MD, Harold KL, Axel L, Joseph PM. Agarose as a tissue equivalent phantom material for NMR imaging. Magn Reson Imaging 1986;4:263–6.

[27] Christoffersson JO, Olsson LE, Sjöberg S. Nickel-doped agarose gel phantoms in MR imaging. Acta Radiol 1991;32:426–31. doi:10.1177/028418519103200519.

[28] Hattori K, Ikemoto Y, Takao W, Ohno S, Harimoto T, Kanazawa S, et al. Development of MRI phantom equivalent to human tissues for 3.0-T MRI. Med Phys 2013;032303:0–11. doi:10.1118/1.4790023.

[29] Yoshimura K, Kato H, Kuroda M, Yoshida A, Hanamoto K, Tanaka A, et al. Development of a Tissue-Equivalent MRI Phantom Using Carrageenan Gel. Magn Reson Med 2003;50:1011–7. doi:10.1002/mrm.10619.

[30] Ikemoto Y, Takao W, Yoshitomi K, Ohno S, Harimoto T, Kanazawa S, et al. Development of a human-tissue-like phantom for 3.0-T MRI. Med Phys 2011;38:6336–42. doi:10.1118/1.3656077.

[31] Luca DF, Maraviglia B, Mercurio A. Biological tissue simulation and standard testing material for MRI. Magn Reson Med 1987;4:189–92.

[32] Mazzara PG, Briggs RW, Wu Z, Steinbach BG. Use of a Modified Polysaccharide Gel in Developing a Realistic Breast Phantom for MRI. Magn Reson Imaging 1996;14:639–48. doi:10.1016/j.jemermed.2016.09.002.

[33] Hellerbach A, Schuster V, Jansen A, Sommer J. MRI Phantoms - Are There Alternatives to Agar? PLoS One 2013;8. doi:10.1371/journal.pone.0070343.

[34] Brzozowski P, Penev KI, Martinez FM, Scholl TJ, Mequanint K. Gellan gum-based gels with tunable relaxation properties for MRI phantoms. Magn Reson Imaging 2019;57:40–9. doi:10.1016/j.mri.2018.10.017.

[35] Qiu K, Haghiashtiani G, McAlpine MC. 3D Printed Organ Models for Surgical Applications. Annu Rev Anal Chem 2018;11:annurev-anchem-061417-125935. doi:10.1146/annurev-anchem-061417-125935.

[36] Lorenzo G, Zaritzky N, Califano A. Rheological analysis of emulsion-filled gels based on high acyl gellan gum. Food Hydrocoll 2013;30:672–80. doi:10.1016/j.foodhyd.2012.08.014.

[37] Cheng B, Chatzinoff Y, Szczepanski D, Bing C, Shaikh S, Wyman O, et al. Remote acoustic sensing as a safety mechanism during exposure of metal implants to alternating magnetic fields. PLoS One 2018;13. doi:10.1371/journal.pone.0197380.

[38] Rabiet M, Brissaud F, Seidel JL, Pistre S, Elbaz-Poulichet F. Positive gadolinium anomalies in wastewater treatment plant effluents and aquatic environment in the Hérault watershed (South France). Chemosphere 2009;75:1057–64. doi:10.1016/j.chemosphere.2009.01.036.

[39] Hanns-Joachim W, Brasch RC, Press W-R, Wesbey GE. Characteristics of Gadolinium-DTPA Complex: A Potential NMR Contrast Agent. Am J Roentgenol 1983;142:619–24. doi:10.2214/ajr.142.3.619.

[40] Gale EM, Atanasova IP, Blasi F, Ay I, Caravan P. A Manganese Alternative to Gadolinium for MRI Contrast. J Am Chem Soc 2015;137:15548–57. doi:10.1021/jacs.5b10748.

[41] Morgan LO, Nolle AW. Proton Spin Relaxation in Aqueous Solutions of Paramagnetic Ions. II. Cr+++, Mn++, Ni++, Cu++, and Gd+++. J Chem Phys 1959;31:365–8. doi:10.1063/1.1730360.

[42] Tiwari A, Verma NC, Singh A, Nandi. CK, Randhawa JK. Carbon coated core-shell

multifunctional fluorescent SPIONs. Nanoscale 2018. doi:10.1039/C8NR01941J.

[43] Brown GC, Cowin GJ, Galloway GJ. A USPIO doped gel phantom for R2* relaxometry. Magn Reson Mater Physics, Biol Med 2017;30:15–27. doi:10.1007/s10334-016-0576-x.

[44] Mohammed L, Ragab D, Lin S, Said S, Gomaa H, Mequanint K. Preparation and Characterization of Glycol Chitosan-Fe 3 O 4 Core–Shell Magnetic Nanoparticles for Controlled Delivery of Progesterone. J Biomater Tissue Eng 2017;7:561–70. doi:10.1166/jbt.2017.1603.

[45] Villafranca JJ, Yost FJ, Fridovich I. Magnetic Resonance Studies of Manganese and Iron (III) Superoxide Dismutases. J Biol Chem 1974;249:3532–6.

[46] Chang S, Lamm SH. Human health effects of sodium azide exposure: a literature review and analysis. Int J Toxicol 2015;22:175–86. doi:10.1080/10915810390201145.

[47] Andersen AF. Final amended report on the safety assessment of Methylparaben, Ethylparaben, Propylparaben, Isopropylparaben, Butylparaben, Isobutylparaben, and Benzylparaben as used in cosmetic products. Int J Toxicol 2008;27 Suppl 4:1–82. doi:10.1080/10915810802548359.

[48] Nalawade T, Sogi SP, Bhat K, Bhat K, Sogi SHP, Sogi SHP, et al. Bactericidal activity of propylene glycol, glycerine, polyethylene glycol 400, and polyethylene glycol 1000 against selected microorganisms. J Int Soc Prev Community Dent 2015;5:114. doi:10.4103/2231-0762.155736.

[49] Bottomley PA, Hardy CJ, Argersinger RE, Allen moore G. A review of 1H nuclear magnetic resonance relaxation in pathology: Are T1 and T2 diagnostic? Med Phys 1987;14:1–37. doi:10.1118/1.596111.

[50] Lauffer RB. Paramagnetic Metal Complexes as Water Proton Relaxation Agents for NMR Imaging: Theory and Design. Chem Rev 1987;87:901–27. doi:10.1021/cr00081a003.

[51] Solomon I. Relaxation Processes in a System of Two Spins. Phys Rev 1955;99:559.

[52] Bloembergen N. Proton relaxation times in paramagnetic solutions. J Chem Phys 1957;27:572–3. doi:10.1063/1.1743771.

[53] Roch A, Muller RN, Gillis P. Theory of proton relaxation induced by superparamagnetic particles. J Chem Phys 1999;110:5403–11. doi:10.1063/1.478435.

[54] Boni A, Bardi G, Bertero A, Cappello V, Emdin M, Flori A, et al. Design and optimization of lipid-modified poly(amidoamine) dendrimer coated iron oxide nanoparticles as probes for biomedical applications. Nanoscale 2015;7:7307–17. doi:10.1039/C5NR01148E.

[55] Gossuin Y, Serhan Z, Sandiford L, Henrard D, Marquardsen T, de Rosales RTM, et al. Sample Shuttling Relaxometry of Contrast Agents: NMRD Profiles above 1 T with a Single Device. Appl Magn Reson 2016;47:237–46. doi:10.1007/s00723-015-0751-7.

[56] Merbach A, Helm L, Toth E. The Chemistry of Contrast Agents in The Chemistry of Contrast Agents in. John Wiley & Sons; 2013.

[57] Chan KWY, Wong WT. Small molecular gadolinium(III) complexes as MRI contrast agents for diagnostic imaging. Coord Chem Rev 2007;251:2428–51. doi:10.1016/j.ccr.2007.04.018.

[58] Ananta JS, Godin B, Sethi R, Moriggi L, Liu X, Serda RE, et al. Geometrical confinement of gadolinium-based contrast agents in nanoporous particles enhances T1contrast. Nat Nanotechnol 2010;5:815–21. doi:10.1038/nnano.2010.203.

[59] Sitharaman B, Jacobson BD, Wadghiri YZ, Bryant H, Frank J. The magnetic, relaxometric, and optical properties of gadolinium-catalyzed single walled carbon nanotubes. J Appl Phys 2013;113:1–7. doi:10.1063/1.4796183.

[60] Kowalewski J, Nordenskiold L, Benetis N, Westlund P-O. Theory of nuclear spin relaxation in paramagnetic systems in solution. Prog Nucl Magn Reson Spectrosc 1985;17:141–85.

[61] Ferreira MF, Mousavi B, Ferreira PM, Martins CIO, Helm L, Martins JA, et al. Gold nanoparticles functionalised with stable, fast water exchanging Gd3+chelates as high relaxivity contrast agents for MRI. Dalt Trans 2012;41:5472–5. doi:10.1039/c2dt30388d.

[62] Patinec V, Rolla GA, Botta M, Tripier R, Esteban-Gómez D, Platas-Iglesias C. Hyperfine coupling constants on inner-sphere water molecules of a triazacyclononane-based Mn(II) complex and related systems relevant as MRI contrast agents. Inorg Chem 2013;52:11173–84. doi:10.1021/ic4014366.

[63] Troughton JS, Greenfield MT, Greenwood JM, Dumas S, Wiethoff AJ, Wang J, et al. Synthesis and evaluation of a high relaxivity manganese(II)-based MRI contrast agent. Inorg Chem 2004;43:6313–23. doi:10.1021/ic049559g.

[64] Sled JG, Pike GB. Standing-Wave and RF Penetration Artifacts Caused by Elliptic Geometry : An Electrodynamic Analysis of MRI. IEEE Trans Med Imaging 1998;17:653–62.

[65] Collins CM, Liu W, Schreiber W, Yang QX, Smith MB. Central brightening due to constructive interference with, without, and despite dielectric resonance. J Magn Reson Imaging 2005;21:192–6. doi:10.1002/jmri.20245.

[66] Getangama NNK. Dielectric Spectroscopy of Polyvinyl Alcohol Hydrogels and Nanocomposites. 2015.

[67] Bartnikas R. Chapter Dielectric and Insulators. Electr. Eng. Handb., Boca Raton, FL, USA: CRC Press LLC; 2000.

[68] Kasap S. Principles of Electronic Materials and Devices: Safa Kasap. 2002.

[69] Bude RO, Adler RS. An easily made, low-cost, tissue-like ultrasound phantom material. J Clin Ultrasound 1995;23:271–3. doi:10.1002/jcu.1870230413.

[70] Solamen LM, McGarry MD, Tan L, Weaver JB, Paulsen KD. Phantom evaluations of nonlinear inversion MR elastography. Phys Med Biol 2018.

[71] Doyley MM, Weaver JB, Van Houten EEW, Kennedy FE, Paulsen KD. Thresholds for

detecting and characterizing focal lesions using steady-state MR elastography. Med Phys 2003;30:495–504. doi:10.1118/1.1556607.

[72] Madsen EL, Hobson MA, Shi H, Varghese T, Frank GR. Tissue-mimicking agar/gelatin materials for use in heterogeneous elastography phantoms. Phys Med Biol 2005;50:5597–618. doi:10.1088/0031-9155/50/23/013.

[73] Milas M, Shi X, Rinaudo M. On the physicochemical properties of gellan gum. Biopolymers 1990;30:451–64. doi:10.1002/bip.360300322.

[74] Montgomery DC. Design and Analysis of Experiments. 6, revised ed. New York: John Wiley & Sons; 2007.

Chapter 3

3 Gellan gum-based gels with tunable relaxation properties for MRI phantoms*

3.1 Overview

In this Chapter, the application of gellan gum gels as novel MRI phantom material with tunable relaxation properties is described. With gellan gum as the gel-forming material, a transparent, thermally stable, simple to fabricate, non-toxic, and tissue equivalent MRI phantom was anticipated to provide a useful tool for MRI verification and calibration. Gellan gum gels doped with synthesized SPIONs and a choice in T_1-modifier with either $MnCl_2$ or $GdCl_3$ at varying concentrations were prepared. Scans from 230 μT to 3 T were conducted determining the concentration effect of each contrast and inspect the magnetic field strength dependency of the contrast agents in a gel environment. The synthesis of SPIONs from a singular metal salt in a precipitation reaction are described. Nineteen gel samples were formulated with varying concentrations of contrast agents to determine the linear, quadratic, and interactive effects of the contrast agents by a central composite design of experiment. The use of various concentrations of metal salts and SPIONs enabled a range of relaxation times that could be used to model human tissue for a known magnetic field strength. Furthermore, the effect of temperature on the relaxation rates of the prepared gels was investigated. The model containing SPIONs and metal salts relaxivity was analyzed with ANOVA, and the resulting significant coefficients were tabulated. The gel material maintained physical, chemical, and biological stability for at least four months and contained controllable relaxation properties while maintaining optical clarity.

3.2 Methodology

3.2.1 Nanoparticle preparation and characterization

SPIONs were prepared by a modified co-precipitation method using a singular iron salt [1]. Briefly, 1.4 g of iron(II) sulphate heptahydrate (Sigma Aldrich, Canada) was dissolved in 50 mL

* A version of this Chapter is published: Pawel Brzozowski, Kalin I. Penev, Francisco M. Martinez, Timothy J. Scholl, and Kibret Mequanint. Gellan Gum-based Gels with Tunable Relaxation Properties for MRI Phantoms. *Magnetic Resonance Imaging*. 57, 40-49; 2019

of deionized water at 40 °C for 30 min while stirring. Next, the iron salt solution was heated to 70 °C and 20 mL of 25 % ammonium hydroxide (Caledon Laboratories, Canada) was added while continuously stirring with an overhead stirrer. The increased pH-triggered precipitation of iron oxide particles. To ensure a complete reaction, the basic ferrous suspension was heated for 90 min at 90 °C while continuously stirring. Once complete, the mixture containing nanoparticles was cooled to room temperature before being magnetically decanted, separating the iron oxide nanoparticles from the bulk liquid. The separated iron oxide nanoparticles were purified three times by washing with 30 mL deionized water, centrifugation, and decanting. The separated SPIONs were dried under vacuum for 24 h. A suspension of SPIONs was prepared in distilled water at a concentration of 0.5 g/L and ultrasonicated before use. A Philips CM 10 transmission electron microscope (TEM) with magnification 18x to 450,000x, resolution 0.5 nm (point) or 0.34 nm (line), and voltage 40 kV to 100 kV was used to determine morphology and size of the SPIONs. The size distribution was determined by estimating the diameters of 421 particles using ImageJ. X-ray Diffraction (XRD) (MiniFlex-Rigaku, The Woodlands, TX) analysis investigated the crystallite structure and the crystalline size (at 2-theta from 20 to 70^o at 0.02 step size, 40 kV x-ray). From the XRD the average crystallite size was estimated by the Scherrer equation

$$D_p = \frac{0.94\lambda}{\beta_{1/2}\cos\theta} \qquad (3\text{-}1)$$

Where D_p represents the average crystallite size, $\beta_{1/2}$ represents the line broadening in radians or the full width half maximum, θ represents the Bragg angle, and λ represents the x-ray wavelength. The magnetic properties of the dried SPIONs were analyzed with a vibrating sample magnetometer (VSM 7407) (Lake Shore cyrotonics, Westerville, OH). The dried powdered SPIONs were characterized at moment measure range of 10^{-10} to 1 J/T (10^{-7} to 10^3 emu) at room temperature and up to a maximum field of 1T (10kOe). The saturation magnetism, coercivity, and retentivity were determined and compared to literature values. Fourier-transform infrared spectroscopy (FTIR) (Bruker Vector 22 FTIR spectrometer) was used to confirm the synthesis of iron oxide and the purity. Small volumes of the dried powder SPIONs were scanned by an attenuated total reflectance (ATR) between 4000 - 500 cm^{-1} with a 4 cm^{-1} resolution and 32 total scans and was controlled by OPUS 5.1 analytical software.

3.2.2 Gellan gum gel preparation

Gellan gum gels preparation followed similar protocol as the previous publication of gellan gum gels used as tissue equivalent materials for radiation dosimetry [2]. As a biopolymer, gellan gum is susceptible to bacterial growth, so methyl 4-hydroxybenzoate (methylparaben) and propylene glycol were utilized as preservatives instead of the more common sodium azide which is undesirable due to its human toxicity [3]. Methyl 4-hydroxybenzoate is an antiseptic used in pharmaceuticals, and a preservative in the food industry [4] and propylene glycol also exhibits antibacterial properties [5] while aiding in the homogeneity and stability of the gel. To prepare the gels (per 100 mL): 1.25 g gellan gum powder (Alfa Aesar, USA) and 100 mg methyl 4-hydroxybenzoate (Sigma Aldrich, Canada) were added into 10.0 mL propylene glycol (Caledon Laboratories, Canada) to solvate the powders. Deionized water (52.5 mL) was then added with vigorous mixing at room temperature in order to disperse the powder. The resulting suspension was heated until complete dissolution. The transparent gel solution was cooled to 55 °C and mixed with the SPION solution and the metal salt solutions of gadolinium(III) chloride hexahydrate ($GdCl_3 \cdot 6H_2O$) (Alfa Aesar, USA) or manganese(II) chloride tetrahydrate ($MnCl_2 \cdot 4H_2O$) (Sigma Aldrich, Canada), and deionized water to the final volume. To form homogenous gel structures with the highly cationic gadolinium ions and avoid the crosslinking of the anionic gellan gum, diethylenetriaminepentaacetic acid (DTPA) (Sigma Aldrich, Canada) was used to chelate the gadolinium ions in 2% molar excess. The final gel composition contained 1.25% (w/v) gellan gum, 10% (v/v) propylene glycol for anti-bacterial properties and spatial stability, 7.55 mM methyl 4-hydroxybenzoate as an antiseptic; synthesized SPIONs (0-30 ppm) as T_2 modifiers; $GdCl_3$ (0 – 140 µM) or $MnCl_2$ (0 - 40 µM) as T_1 modifiers; DTPA (0 - 142.8µM) to stabilize the $GdCl_3$. The gel formulations were poured either into NMR glass tubes (10 mm diameter, 230 mm length) for NMR and MRI measurements shown in Figure 3-1 or into 4 mL poly(methyl methacrylate) (PMMA) cuvettes for optical scans. Optical scans studying the SPION distributions in the gels were performed along the height of PMMA cuvettes using a microplate reader (Infinite 200 Pro, Tecan Group Ltd., Switzerland), equipped with a horizontal cuvette adaptor. Tecan i-control software (Tecan Group Ltd., ver. 1.7.1.12) was used to define a custom plate to take optical readings at 500 nm at thirteen points (1.982 mm apart) along the long axis of the cuvette [6] over a six-week period. As an internal control, fast green FCF dye (Sigma Aldrich, Canada) at 10 µg

dye per 1 mg metal salt was added to enable the optical density of each sample to be dependent on the metal salt concentration allowing internal tracking through optical scans.

Figure 3-1 Gel samples in NMR glass tubes

3.2.3 Design of experiments and statistical analyses

To obtain tunable relaxation times for various human tissues, designs of experiments were implemented independently for both metal salts to predict the relaxation times of the samples based on the concentration of the contrast agents. A central composite design of experiment was chosen due to its simplicity and ability to determine the quadratic, linear, and interactive effects of the contrast agent concentration on the relaxation properties in the regression model. Initially, each design contained four points at two concentrations of SPIONs and metal salt [7]. The design was augmented with four intermediate points making a central composite design as shown in Figure 2-6 (Chapter 2.3). Furthermore, three centre points in the middle of the design space were used to analyze the variance of prediction and to aid the quadratic effect analysis. In total, 11 compositions were required for the design of experiments with each metal salt. The design order was randomized to ensure consistency as can be seen in Tables 3-1 and 3-2. With the data generated, the relaxation times were fitted to the concentration of SPIONs, metal salts, and the interaction between the contrast agents using the statistics program R (version 3.4.3; Vienna, Austria) regression analysis. ANOVA analyses were conducted to determine the significance of the coefficients in the regression models, and the models were refined with only the significant effects [7].

Table 3-1 MRI additives concentrations coded at three levels,

Coded		Levels		
		-1	0	1
SPIONs	ppm	0	15	30
$MnCl_2$	µM	0	20	40
$GdCl_3$-DTPA	µM	0	70	140

Table 3-2 Coded central composite design of experiment composition list

#	Order	SPION	$MnCl_2$	$GdCl_3$-DTPA
1	6	-1	-1	-1
2	5	1	-1	-1
3	3	-1	1	-1
4	2	1	1	-1
5	1	0	0	-1
6	4	0	0	-1
7	7	0	0	-1
8	8	-1	0	-1
9	10	1	0	-1
10	9	0	-1	-1
11	11	0	1	-1
12	15	-1	-1	1
13	13	1	-1	1
14	12	0	-1	0
15	14	0	-1	0
16	16	0	-1	0
17	18	-1	-1	0
18	19	1	-1	0
19	17	0	-1	1

3.2.4 NMR and MRI measurements

T_1 relaxation times were acquired at low magnetic fields from 230 µT to 1 T on a fast field-cycling NMR relaxometer (SpinMaster FFC2000 1T C/DC, Stelar, s.r.l., Mede, Italy) by changing the relaxation field in 30 steps, logarithmically distributed using an acquisition field of 380.5 mT. The measurements were conducted at three different temperatures in the relaxometer (20 °C, 25 °C, and 30 °C) to study the effects of temperature on the relaxation properties of each contrast agent in the gel. For higher field strengths, T_1 and T_2 weighted MRI images were acquired in a plane transverse to the cylindrical axis of the NMR tubes (coronal plane of the scanner) for three adjacent 10-mm-thick slices on a 1.5-T GE CVMR and a 3.0-T GE Discovery MR750 clinical scanners (General Electric Healthcare, Milwaukee, WI, USA) at room temperature (25 °C). Any misalignment among the slices was assessed and remedied during image reconstruction using the image registration tools of MATLAB (version 9.3, MathWorks, Inc., Natick, MA). In addition, edge and partial-volume effects of the air-glass-gel interface were assessed by eroding the boundaries of the region of interest (ROI) drawn around the gel in each test tube (see Appendices A and B). T_1 measurements were obtained using an Inversion Recovery Fast Spin Echo pulse sequence with 15 inversion times (TI) logarithmically distributed between 50 and 4000 ms. Other imaging parameters include repetition time (TR)=10 s, Echo time (TE)=6.5 ms, Echo Train Length (ETL)=4, slice thickness (THK)=10 mm, Field of view (FOV)=130×130 mm, matrix size of 256×256 points, and receive Bandwidth (BWr) of 125 kHz. T_2 measurements were estimated using a Spin Echo Multi-Echo pulse sequence with 62 different echo times covering a range from 9 ms to 480 ms, TR=2000 ms, THK=10 mm, BWr=83.3 kHz, with a matrix of 256×256, FOV=130×130mm (a representative data set and curve fit is shown in Appendix C). The signal intensity as a function of inversion time for the stack of images was analyzed on a pixel-by-pixel basis to give the T_1 and T_2 relaxation times of the samples. MATLAB was used to generate non-linear fits for each pixel to defined by the following equations:

$$S_{I,1} = K \cdot \left(M_0 - (M_0 - M_z(0)) \cdot e^{\left(-TI/T_1\right)} \right) \quad (3\text{-}2)$$

$$S_{I,2} = K \cdot M_{xy} \cdot e^{\left(-TE/T_2\right)} + n_{off} \quad (3\text{-}3)$$

Where $S_{I,1}$ and $S_{I,2}$ are the measured signal intensity, M_0 is the steady state longitudinal magnetization at thermal equilibrium, $M_z(0)$ is the magnitude of the inverted magnetization acquired during the readout, M_{xy} is the transverse magnetization, K is a constant from

magnetization into signal voltage, and n_{off} is any offset noise present on the images. M_0, $M_z(0)$, M_{xy}, T_1, and T_2 are found in the fitting.

3.3. Results and discussions

3.3.1 Particle-size analysis, magnetic properties, and in-gel stability of SPIONs

The prepared SPIONs characterization results are shown in Figure 3-2. The TEM image (Figure 3-2a) demonstrated that the SPIONs had agglomerated on the TEM sample grid due to electrostatic interactions in the neutral aqueous environment during the drying process. Embedded in the TEM image is the corresponding particle-size distribution histogram which displayed the average size to be 6.6 nm. A positive skew from a normal distribution indicated the formation of large sized particles. The magnetic properties of the synthesized SPIONs are shown in Figure 3-2b where the magnetization curve indicated their superparamagnetic nature with minimal hysteresis from the near-zero coercivity and retentivity. The saturation magnetism of 77.24 A·m2/kg (emu/g) is lower than the bulk magnetism of magnetite but is similar to that of other reported SPIONs [8]. The lower saturation magnetism could be accounted for by the large distribution in particle size confirmed by the TEM image and by the production of diamagnetic iron oxide minerals influencing the overall magnetic field. The nonzero retentivity (7.05 A·m2/kg [emu/g]) and coercivity (5.636 mT [56.36 G]) shown by magnifying the origin in Figure 3-2c also indicates the non-uniform size distribution of the SPIONs and formation of other iron oxide minerals. However, the concentration of diamagnetic iron structures is expected to be minimal since the XRD diffraction peaks show no indication of other mineral structures. The XRD results confirm the formation of iron oxide particles (Figure 3-2d) showing six diffraction rings (peaks) corresponding to the formation of the SPION structure. With the largest diffraction ring, the Scherrer equation (Eq. (3-1)) estimated the average crystalline size to be 27.5 nm. At this size, the SPIONs are superparamagnetic [8]. The difference in average size estimation between the TEM and XRD may be explained by the positive skew in the histogram indicating the formation of larger particles. FTIR also confirmed SPION formation seen in Appendix D. The distribution of the SPIONs in the gel with or without metal salts was studied by optical scans as shown in Figure 3-2e and 3-2f. The data indicated an even distribution of the SPIONs with no evidence of settling within the six-week period. The wavelength of 500 nm was chosen to avoid the effect of the FCF dye which does not absorb around 500 nm. Figure 3-2e contains the average optical density of the entire cuvette as a

solid line to illustrate the SPION distribution around its mean. The SPION distribution optical density profile is not significantly different from the average line, and the variation can be explained by inhomogeneities in the cuvette. Even after six weeks at room temperature, the average optical density did not change significantly. This is further supported by Figure 3-2f where the optical density of each composition is not different from the average. Collectively, Figure 3-2e and 3-2f demonstrate that no change is seen in the spatial stability of the gel over the tested period for any of the compositions.

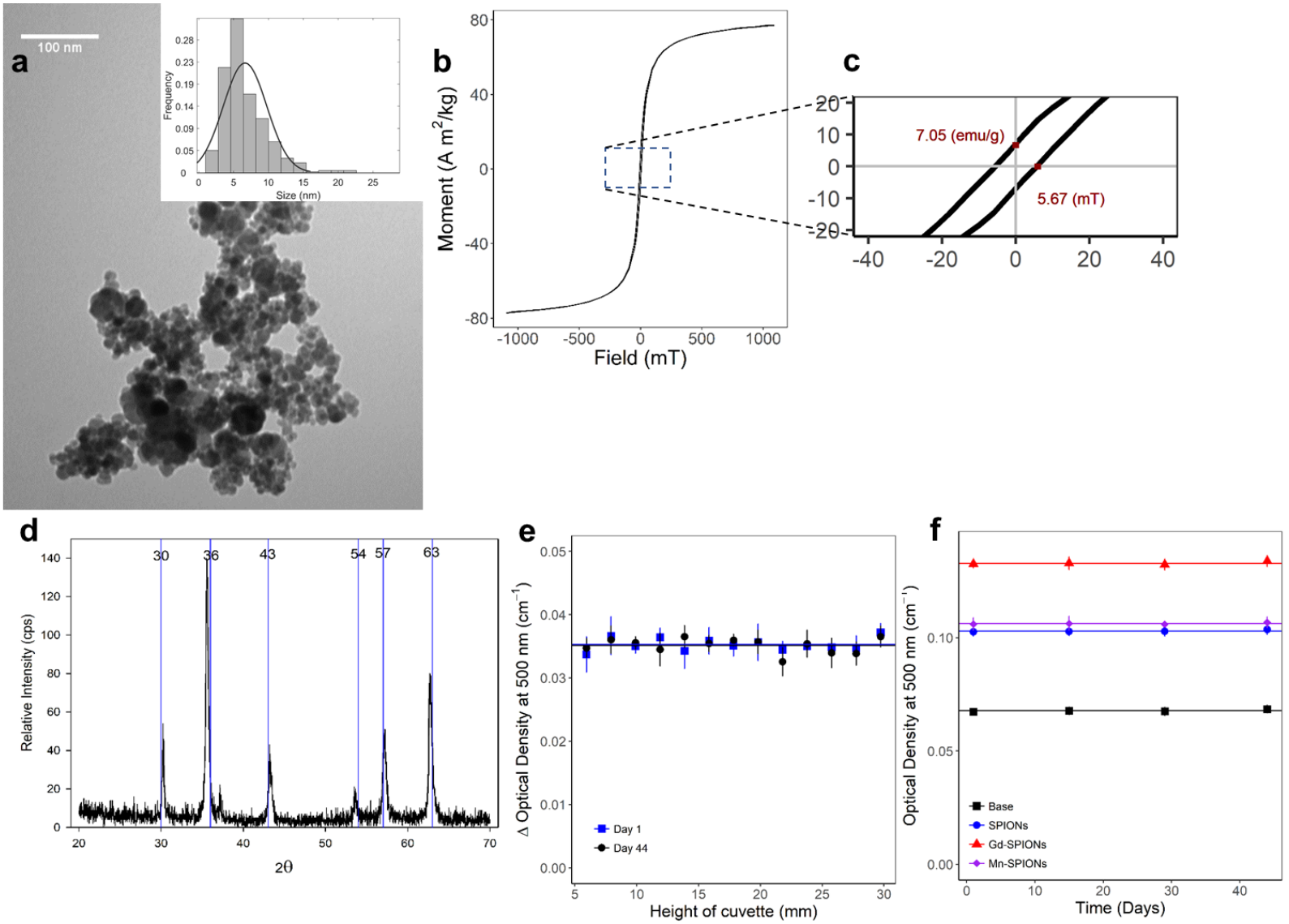

Figure 3-2 Characterization of SPIONs. (a) TEM image illustrating the size of the dried SPIONs. Included is a particle size distribution histogram. (b) Superparamagnetic properties of SPIONs. (c) Axis magnified displaying coercivity and retentivity values. (d) XRD spectrum of SPION particles. (e) Optical scans normalized to the base gel demonstrating the distribution of SPIONs in a gel at two time points indicated by "square" for the initial scans and "circle" for 44 days. Done in triplicates and plotted with average value lines. (f) Optical scans for temporal analysis of base gel ("square") points, SPION ("circle"), SPION-Mn ("diamond"), and SPION-Gd ("triangle") doped gels in triplicates and plotted with average value lines.

3.3.2 Relaxation properties of SPION and metal salts doped gel phantoms

The effect of varying magnetic field strength on the R_1 relaxation rate is plotted in Figure 3-3 for different gel compositions. Compared to the base gel (no SPIONs), the concentration of SPIONs (30 ppm and 15 ppm) had no effect on R_1 relaxation rate for all investigated magnetic field strengths (Figure 3-3a) suggesting that neither the presence of SPIONs nor their amount influenced the R_1 relaxation rate. However, the R_1 relaxation rates decreased for all the samples as the magnetic field strength increased before reaching a plateau at approximately 0.1 T. This decrease is likely caused by the higher mobility of the water protons in the gelled environment with an increased magnetic field. Figure 3-3b presented the effect of $MnCl_2$ concentration on the R_1 relaxation rates at a constant SPIONs concentration (30 ppm). At a fixed magnetic field strength, increasing $MnCl_2$ resulted in an increased R_1, as expected. Below 0.05 T, the R_1 profile follows a similar trend for all three samples. Above 0.05 T, $MnCl_2$ increased the relaxation rate greatly before reaching a maximum around 0.5 T, indicating that the gellan gum phantom material with $MnCl_2$ exhibited noticeable differences in relaxation rate when scanned at different magnetic field strengths. Figure 3-3c revealed that while $GdCl_3$ increased R_1 in a concentration-dependent manner, its effect did not pass through a minimum and maximum points. Again, the concentration of SPIONs in the $GdCl_3$ samples was kept constant (30 ppm). Below 0.01 T, the relaxation rate becomes more dependent on magnetic field strength with the relaxation rates increasing more rapidly than those of the base gel.

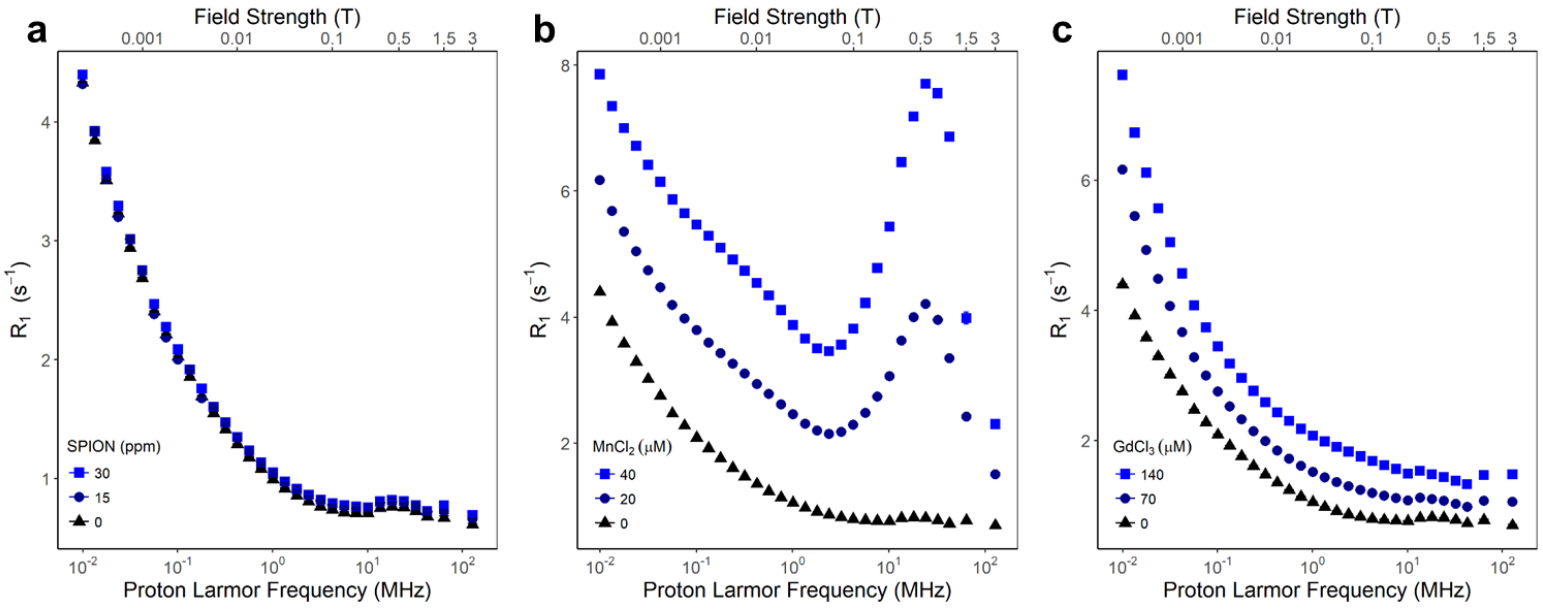

Figure 3-3 The effect of magnetic field strength at different concentration of contrast agents on relaxation rates (R_1), log-normal scale. (a) SPIONs, (b) $MnCl_2$ at 30 ppm SPIONs, and (c) $GdCl_3$ at 30 ppm SPIONs. Legend: "square" high concentration of contrast agent, "circle" medium concentration, and "triangle" low concentration.

Figure 3-4 presented the metal salt effect on both R_1 and R_2 relaxation rates for different SPION concentrations at clinically relevant magnetic field strengths. The slopes in Figure 3-4(a, b, d, and e) represent the relaxivity of the metal salt at the indicated field strength and SPION concentration. The R_1 relaxivity of $MnCl_2$ is more strongly dependent on magnetic field strength than on the SPION concentration. The dependency of field strength causes the relaxivity of $MnCl_2$-containing gels to vary considerably, indicating that a unique model at each magnetic field strength is required to have accurate relaxation properties. Figure 3-4b shows the R_2 relaxation rate at 1.5 T and 3 T for $MnCl_2$-containing gels. Similar to the R_1 relaxation rate, the R_2 relaxation rate is also dependent on magnetic field strength; however, the dependency is minor compared to the SPIONs concentration effect. Overall, adding SPIONs affected the R_2 relaxation rate while R_1 relaxation rate was unchanged, allowing an independent control of the two relaxation properties. Figure 3-4c represents the T_1–T_2 design space map for $MnCl_2$ and SPIONs containing gels at 1.5 T. Each point represents a scanned sample and its corresponding T_1 and T_2 values with a total of nine distinct concentrations. The solid line indicates an iso-metal salt concentration and the dashed line

represents iso-SPIONs concentrations. Reported human tissue relaxation times [9] are superimposed to the design space to illustrate how they fit into the design space. Tissue relaxation data plotted were colour-coded to indicate the specific tissues. Since the reported relaxation times included both healthy and pathological tissues, there is a scatter around the design space even for a specific tissue (e.g. brain tissue). The longer relaxation times seen typically in more aqueous tissues exist near the boundary of the design space seen by the cluster of data for brain tissues. Shown in Figures 3-4(d–f) are the $GdCl_3$ and SPIONs containing samples at eight distinct concentrations. Figure 3-4d plots the R_1 relaxation rate and the relaxivity of the $GdCl_3$. Both the magnetic field strength and the SPIONs concentrations effects are minor in contrast to the $MnCl_2$ plots where the magnetic field strength was the dominant effect. This result is corroborated in literature which showed stronger dependence on the field strength for the relaxivity induced by manganese-based contrast agents over gadolinium [10]. The R_2 relaxation rates for the $GdCl_3$ samples are plotted in Figure 3-4e, and again the metal salt concentration increases the R_2 relaxation rate. The results are comparable to $MnCl_2$ with the SPIONs concentration having a more substantial influence on R_2 relaxation rate than magnetic field strength. Samples with no SPIONs have higher R_2 relaxation rates at larger magnetic field strengths (3 T), but when SPIONs are introduced and their concentration is increased a larger relaxation rates is observed at 1.5 T. Therefore, the effect of SPIONs on the R_2 relaxation rate is also dependent on magnetic field strength. Similar to $MnCl_2$, a design space map for $GdCl_3$ samples is plotted at 1.5 T in Figure 3-4f with the same known human tissue relaxation times. Strong dependency of the $MnCl_2$-induced relaxivity on the magnetic field strength and temperature has been previously reported [9]; however, the $GdCl_3$-induced relaxivity is less sensitive to field strength and temperature making it more attractive. Nevertheless, $GdCl_3$ has other disadvantages including environmental and health concerns when preparing, handling and disposing [11,12]. Furthermore, the relaxivity induced by $GdCl_3$ is lower than $MnCl_2$ requiring higher concentrations of the metal salt for similar relaxation rates.

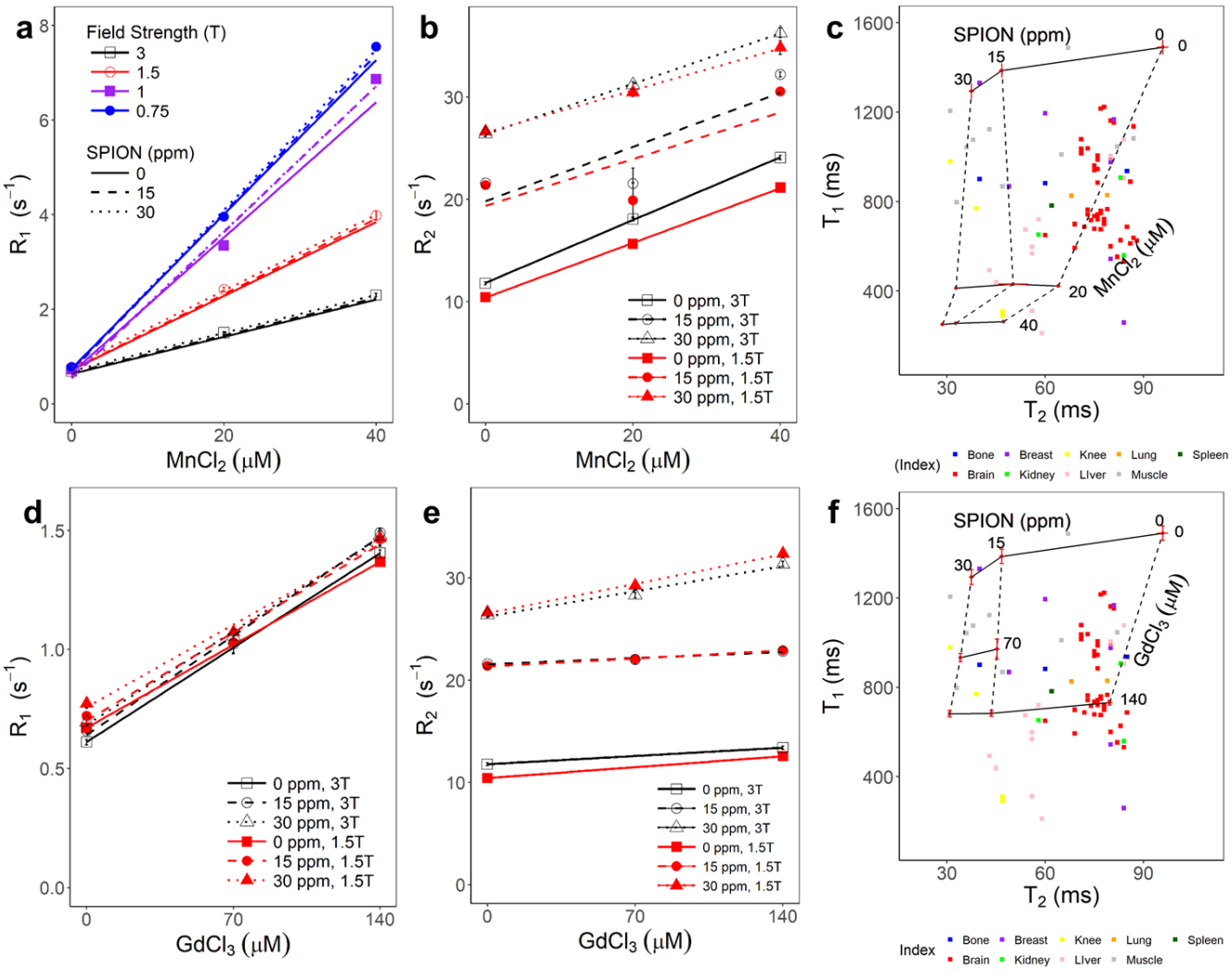

Figure 3-4 Relaxivity of the gellan gum gels at varying contrast agent concentrations and magnetic field strengths. (a) R_1 relaxation rate for $MnCl_2$ concentration with the effects of SPION indicated by the line-type ("solid" is 0 ppm, "dashed" is 15 ppm, "dotted" is 30 ppm) and field strength indicated by the colour or the point shape (black "open-square" is 3 T, red "open-circle" is 1.5 T, purple "filled-square" is 1 T, and blue "filled-circle" is 0.75 T. (b) R_2 relaxation rate versus the $MnCl_2$ concentration with the effects of SPION indicated by line-type and by point shape ("solid line and square" is 0 ppm, "dashed line and circle" is 15 ppm, "dotted line and triangle" is 30 ppm) and the field strength is indicated by the colour or point fill (black "open point" is 3 T and red "filled point" is 1.5 T). (c) T_1-T_2 map for $MnCl_2$ at 1.5 T where each "solid" point represents a concentration tested, "solid" lines represent iso-metal salt concertation, and "dashed" lines represent iso-SPION concentration. "square" points represent known relaxation times for various human tissues indexed by tissue type by colour. Error bars are indicated in red. (d) R_1 relaxation rate versus the $GdCl_3$ concentration with the effects of SPION and the field strength. (e) R_2 relaxation rate versus the $GdCl_3$ concentration with the effects of SPION and the field strength. (f) T_1-T_2 map for $GdCl_3$ at 1.5 T.

3.2.3 The effect of temperature and time on relaxation properties

To determine the effect of temperature, R_1 relaxation rates were measured at three temperatures (20 °C, 25 °C, and 30 °C) for three gel compositions (40 μM $MnCl_2$, 30 ppm SPIONs + 40 μM $MnCl_2$, and 140 μM $GdCl_3$) as shown in Figure 3-5a–c, respectively. The results indicate that temperature does have some effect on the relaxation properties of the gellan gum gel phantom regardless of contrast agent. As the temperature is decreased, the relaxation rates increased slightly, which is a typical response for gel phantoms [13]. Here, this trend was not dependent on the type of contrast agent chosen. As a further analysis of MRI signal stability, a set of samples were re-scanned after six weeks of storage at room temperature. Samples containing the same composition as the temperature study were measured but only the sample containing 30 ppm SPIONs and 40 μM $MnCl_2$ is shown in Figure 3-5d as it was hypothesized to change the most with time containing both SPIONs and $MnCl_2$. All tested composition gave similar results, and after six weeks of storage the R_1 relaxation profile is similar, but a slight increase in relaxation rates occurred. Further analysis is shown in Figure 3-5e where the relaxation rates at the two time points are compared against each other in a comparison plot where $R_{1,i}$, represents the initial scans and $R_{1,f}$ represents the scans after six weeks. A slight increase in relaxation rates occurs with time shown by the slope of 1.02 instead of 1.00, however, a linear relation exists (R^2=0.9988) between the results. The increase of relaxation rates may be explained by the loss of water from the gel, which can be prevented by careful sealing.

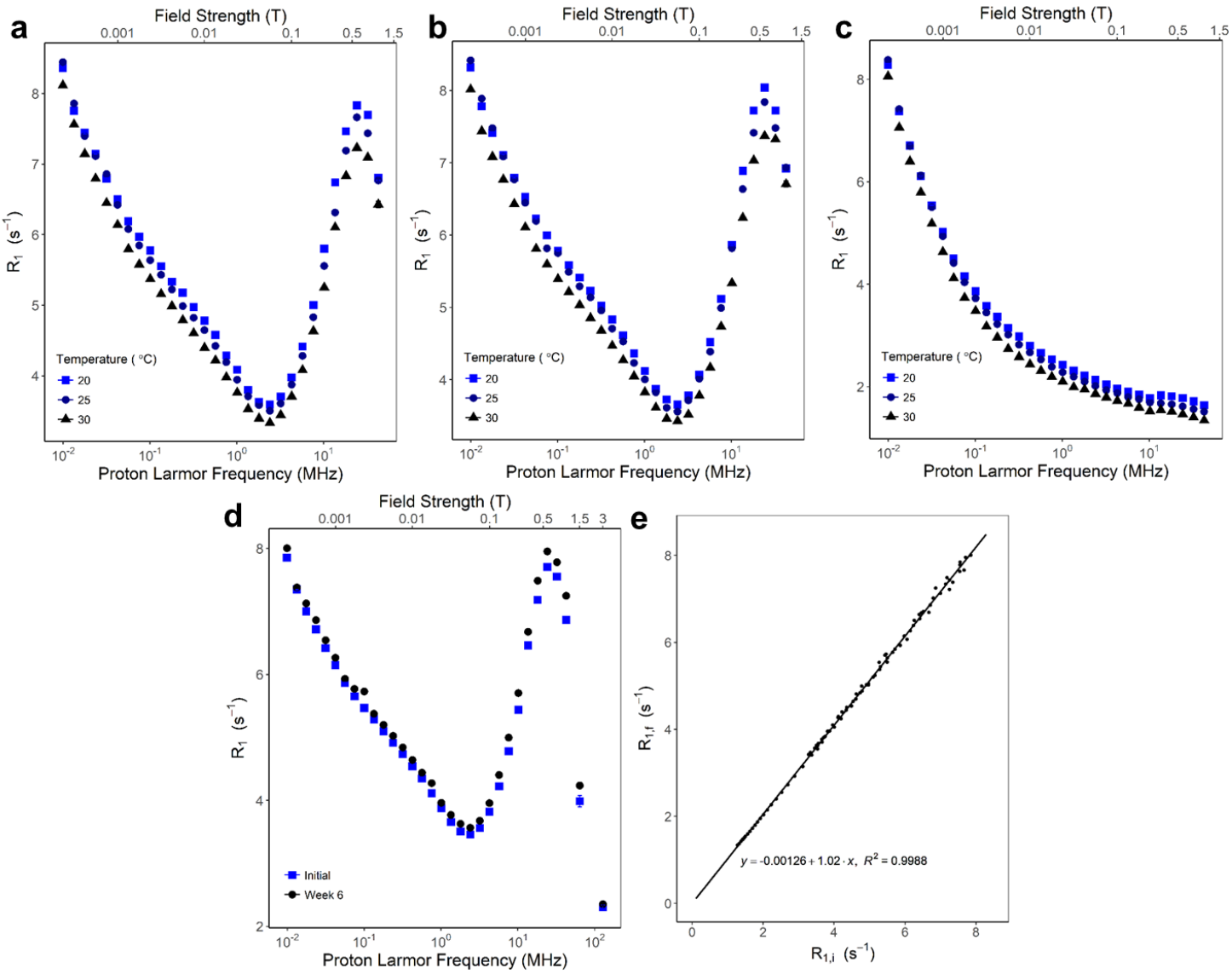

Figure 3-5 The effect of temperature on NMR R_1 relaxation rate for gellan gum phantoms. (a) $MnCl_2$, (b) SPION-$MnCl_2$, and (c) $GdCl_3$ as indicated: legend is: "square" for 20 °C, "circle" for 25 °C, and "triangle" for 30 °C). (d) Temporal analysis of R_1 relaxation rate initially "square" and after six weeks "circle". (e) Comparison plot of the initial relaxation rates and after six weeks.

3.2.4 Tunable Relaxation Rates

The central composite design was fitted to the following equation to estimate the base, linear, quadratic, and interaction concentration effects at varying field strengths for a constant temperature of 25 °C.

$$R_{i,j} = a_{i,j,0} + a_{i,j,1} \cdot C_{m,j} + a_{i,j,2} \cdot C_S + a_{i,j,3} \cdot {C_{m,j}}^2 + a_{i,j,4} \cdot {C_S}^2 + \\ + a_{i,j,5} \cdot C_{m,j} \cdot C_S \quad (3\text{-}4)$$

Where $R_{i,j}$ represents either longitudinal (R_1; $i = 1$) or transverse (R_2; $i = 2$) relaxation rates with j being 1 for $MnCl_2$ and 2 for $GdCl_3$; $a_{i,j,k}$ represents the best fit coefficients shown in Table 3-3 to 3-6 with k corresponding to the type of effect (base, linear metal salt, linear SPIONs, quadratic metal salt, quadratic SPIONs, or interactive for 0, 1, 2, 3, 4, or 5 respectively); $C_{m,j}$ is the concentration of metal salt; and C_S is the concentration of SPIONs. Using ANOVA, the significance ($p < 0.05$) of each coefficient to predicting the relaxation rate was evaluated. For R_1, the linear effect of the metal salts was significant at all field strengths. While, the linear SPION effect was significant at 1.5 and 3 T and loses significance at lower field strengths. The quadratic effect of the metal salt was significant between 0.75 and 1 T but loses significance at higher or lower field strengths. The quadratic effects of the SPION concentration and the interaction of the SPION to either metal salt were not significant. With the significance of each parameter known, the linear regression was repeated with the significance terms only. The p-values showing the significance of each term is shown in Appendices E to H. The results can be seen in Table 3-3 for $MnCl_2$ and Table 3-5 for $GdCl_3$. The adjusted R^2 values of the linear regressions indicate an excellent fit at all field strengths for $MnCl_2$ (>0.994) and $GdCl_3$ (>0.97). Adjusted R^2 value compares the explanatory power of the regression model to the number of parameters used. This way only parameters that are useful in predicting the relaxation rate increase the accuracy of the model. Therefore, the adjusted R^2 values for both metal salts indicated that the model was able of accurately predicting the R_1 relaxation rates within the design space for all magnetic field strength tested. For R_2, the base and linear effects for both metal salts and SPIONs were significant at the field strengths tested. The quadratic concentration effect of the SPIONs was significant with the $GdCl_3$ model while not significant with the $MnCl_2$ model. The quadratic effect of the metal salt and the interaction effect of the SPION to either metal salt were not significant. As with R_1, the linear regression was repeated accounting for significance terms and are shown in Table 3-4 for $MnCl_2$ and Table 3-6 for $GdCl_3$. Again, the adjusted R^2 values indicates a good fit for the $GdCl_3$ model (>0.978). The adjusted R^2 values for the $MnCl_2$ fit was lower (>0.87) but still a reasonable fit. With either set of equations, tunable relaxation properties can be targeted and achieved. Even with the 11 and 10 samples for $MnCl_2$ and $GdCl_3$ respectively, the model was accurate showing the benefit of using a design of experiments. The choice of central composite design allowed

further analysis into the quadratic effects which were important especially for the R_2 relaxation rates. The design space was limited by the lower limits of the relaxation rate of the base gel indicated in Figure 3-4c and 3-4f, where the gellan gum sample would not be able to model the tissues relaxation properties. This limitation restricts gellan gum samples from mimicking liquids within tissues or tissues with long relaxation times.

Table 3-3 Coefficient for longitudinal relaxation rates (R_1) equation for $MnCl_2$ at all field strengths tested. (ns) indicate not significant with p-value > 0.05.

Field Strength	$a_{1,1,0}$ (s^{-1})	$a_{1,1,1}$ $(\mu M \cdot s)^{-1}$	$a_{1,1,2}$ $(ppm \cdot s)^{-1}$	$a_{1,1,3}$ $(\mu M^{-2} \cdot s^{-1})$	$a_{1,1,4}$ $(ppm^{-2} \cdot s^{-1})$	$a_{1,1,5}$ $(\mu M \cdot ppm \cdot s)^{-1}$	Adjusted-R^2
3	0.62 ± 0.02	0.0397 ± 0.0005	0.0028 ± 0.0007	(ns)	(ns)	(ns)	0.998
1.5	0.68 ± 0.03	0.0795 ± 0.0009	0.0038 ± 0.0012	(ns)	(ns)	(ns)	0.998
1.0009	0.71 ± 0.13	0.1116 ± 0.0097	(ns)	0.00097 ± 0.00023	(ns)	(ns)	0.995
0.75691	0.76 ± 0.08	0.1497 ± 0.0062	(ns)	0.00042 ± 0.00015	(ns)	(ns)	0.998
0.56715	0.76 ± 0.04	0.1719 ± 0.0015	(ns)	(ns)	(ns)	(ns)	0.999
0.42505	0.78 ± 0.03	0.1603 ± 0.0012	(ns)	(ns)	(ns)	(ns)	0.999
0.31851	0.79 ± 0.03	0.1399 ± 0.0013	(ns)	(ns)	(ns)	(ns)	0.999
0.23863	0.71 ± 0.04	0.1169 ± 0.0015	(ns)	(ns)	(ns)	(ns)	0.998
0.17885	0.73 ± 0.03	0.0998 ± 0.0011	(ns)	(ns)	(ns)	(ns)	0.998
0.13403	0.73 ± 0.02	0.0868 ± 0.0008	(ns)	(ns)	(ns)	(ns)	0.999
0.10049	0.77 ± 0.02	0.0749 ± 0.0007	(ns)	(ns)	(ns)	(ns)	0.999
0.075277	0.79 ± 0.01	0.0689 ± 0.0006	(ns)	(ns)	(ns)	(ns)	0.999
0.056393	0.84 ± 0.03	0.064 ± 0.0011	(ns)	(ns)	(ns)	(ns)	0.996
0.042268	0.89 ± 0.02	0.0636 ± 0.001	(ns)	(ns)	(ns)	(ns)	0.997
0.031677	0.95 ± 0.02	0.0667 ± 0.0008	(ns)	(ns)	(ns)	(ns)	0.998
0.023729	1.03 ± 0.02	0.0698 ± 0.0008	(ns)	(ns)	(ns)	(ns)	0.998
0.017795	1.12 ± 0.02	0.0732 ± 0.0009	(ns)	(ns)	(ns)	(ns)	0.998
0.013326	1.22 ± 0.03	0.0759 ± 0.0012	(ns)	(ns)	(ns)	(ns)	0.997
0.009985	1.33 ± 0.03	0.0789 ± 0.0012	(ns)	(ns)	(ns)	(ns)	0.997
0.00748	1.46 ± 0.02	0.0807 ± 0.0008	(ns)	(ns)	(ns)	(ns)	0.999
0.0056074	1.59 ± 0.02	0.0817 ± 0.0008	(ns)	(ns)	(ns)	(ns)	0.999
0.0042075	1.72 ± 0.02	0.0838 ± 0.0009	(ns)	(ns)	(ns)	(ns)	0.998
0.0031574	1.9 ± 0.02	0.0833 ± 0.0008	(ns)	(ns)	(ns)	(ns)	0.998

0.0023638	2.06 ± 0.03	0.0846 ± 0.0012	(ns)	(ns)	(ns)	(ns)	0.998
0.0017659	2.25 ± 0.03	0.0841 ± 0.0011	(ns)	(ns)	(ns)	(ns)	0.998
0.0013252	2.38 ± 0.04	0.09 ± 0.0024	0.0025 ± 0.001	-0.00014 ± 0.00006	(ns)	(ns)	0.999
0.00099331	2.75 ± 0.03	0.0837 ± 0.0011	(ns)	(ns)	(ns)	(ns)	0.998
0.00074206	3.01 ± 0.03	0.0839 ± 0.0012	(ns)	(ns)	(ns)	(ns)	0.998
0.00055583	3.27 ± 0.04	0.0854 ± 0.0015	(ns)	(ns)	(ns)	(ns)	0.997
0.00041615	3.57 ± 0.04	0.0851 ± 0.0016	(ns)	(ns)	(ns)	(ns)	0.997
0.00031372	3.85 ± 0.04	0.092 ± 0.0025	0.0034 ± 0.0011	-0.0002 ± 0.00006	(ns)	(ns)	0.999
0.00023315	4.39 ± 0.05	0.0855 ± 0.0022	(ns)	(ns)	(ns)	(ns)	0.994

Table 3-4 Coefficient for transverse relaxation rates (R_2) equation for $MnCl_2$ at all field strengths tested. (ns) indicate not significant with p-value > 0.05

Field Strength	$a_{2,1,0}$ (s^{-1})	$a_{2,1,1}$ $(\mu M \cdot s)^{-1}$	$a_{2,1,2}$ $(ppm \cdot s)^{-1}$	$a_{2,1,3}$ $(\mu M^{-2} \cdot s^{-1})$	$a_{2,1,4}$ $(ppm^{-2} \cdot s^{-1})$	$a_{2,1,5}$ $(\mu M \cdot ppm \cdot s)^{-1}$	Adjusted-R^2
3	12.1 ± 1.5	0.27 ± 0.05	0.44 ± 0.06	(ns)	(ns)	(ns)	0.889
1.5	10.7 ± 1.7	0.23 ± 0.05	0.5 ± 0.07	(ns)	(ns)	(ns)	0.87

Table 3-5 Coefficient for longitudinal relaxation rates (R_1) equation for $GdCl_3$ at all field strengths tested. (ns) indicate not significant with p-value > 0.05.

Field Strength	$a_{1,2,0}$ (s^{-1})	$a_{1,2,1}$ $(\mu M \cdot s)^{-1}$	$a_{1,2,2}$ $(ppm \cdot s)^{-1}$	$a_{1,2,3}$ $(\mu M^{-2} \cdot s^{-1})$	$a_{1,2,4}$ $(ppm^{-2} \cdot s^{-1})$	$a_{1,2,5}$ $(\mu M \cdot ppm \cdot s)^{-1}$	Adjusted-R^2
3	0.61 ± 0.02	0.0057 ± 0.0002	0.0023 ± 0.001	(ns)	(ns)	(ns)	0.99
1.5	0.66 ± 0.03	0.0051 ± 0.0002	0.0029 ± 0.0012	(ns)	(ns)	(ns)	0.98
1.0009	0.71 ± 0.03	0.0031 ± 0.0005	(ns)	0.000009 ± 0.000004	(ns)	(ns)	0.987
0.75691	0.76 ± 0.03	0.0029 ± 0.0006	(ns)	0.000011 ± 0.000004	(ns)	(ns)	0.985
0.56715	0.77 ± 0.02	0.0046 ± 0.0003	(ns)	(ns)	(ns)	(ns)	0.972
0.42505	0.78 ± 0.02	0.0049 ± 0.0003	(ns)	(ns)	(ns)	(ns)	0.975
0.31851	0.77 ± 0.02	0.0053 ± 0.0003	(ns)	(ns)	(ns)	(ns)	0.978
0.23863	0.74 ± 0.03	0.0039 ± 0.0006	(ns)	0.00001 ± 0.000004	(ns)	(ns)	0.988
0.17885	0.73 ± 0.02	0.0057 ± 0.0002	(ns)	(ns)	(ns)	(ns)	0.985
0.13403	0.74 ± 0.02	0.0061 ± 0.0002	(ns)	(ns)	(ns)	(ns)	0.987

0.10049	0.75 ± 0.03	0.0065 ± 0.0003	(ns)	(ns)	(ns)	(ns)	0.982
0.075277	0.79 ± 0.02	0.0068 ± 0.0003	(ns)	(ns)	(ns)	(ns)	0.987
0.056393	0.82 ± 0.02	0.007 ± 0.0003	(ns)	(ns)	(ns)	(ns)	0.988
0.042268	0.89 ± 0.03	0.0059 ± 0.0006	(ns)	0.000009 ± 0.000004	(ns)	(ns)	0.993
0.031677	0.93 ± 0.03	0.0073 ± 0.0003	(ns)	(ns)	(ns)	(ns)	0.986
0.023729	1.01 ± 0.02	0.0074 ± 0.0003	(ns)	(ns)	(ns)	(ns)	0.988
0.017795	1.1 ± 0.03	0.0076 ± 0.0003	(ns)	(ns)	(ns)	(ns)	0.987
0.013326	1.2 ± 0.02	0.0077 ± 0.0003	(ns)	(ns)	(ns)	(ns)	0.988
0.009985	1.31 ± 0.02	0.0079 ± 0.0003	(ns)	(ns)	(ns)	(ns)	0.989
0.00748	1.44 ± 0.02	0.008 ± 0.0003	(ns)	(ns)	(ns)	(ns)	0.99
0.0056074	1.57 ± 0.02	0.0084 ± 0.0003	(ns)	(ns)	(ns)	(ns)	0.991
0.0042075	1.7 ± 0.03	0.0089 ± 0.0003	(ns)	(ns)	(ns)	(ns)	0.989
0.0031574	1.89 ± 0.02	0.0092 ± 0.0003	(ns)	(ns)	(ns)	(ns)	0.993
0.0023638	2.03 ± 0.03	0.0101 ± 0.0003	(ns)	(ns)	(ns)	(ns)	0.991
0.0017659	2.22 ± 0.03	0.0108 ± 0.0003	(ns)	(ns)	(ns)	(ns)	0.991
0.0013252	2.42 ± 0.03	0.0118 ± 0.0003	(ns)	(ns)	(ns)	(ns)	0.994
0.00099331	2.72 ± 0.03	0.0131 ± 0.0003	(ns)	(ns)	(ns)	(ns)	0.995
0.00074206	2.99 ± 0.03	0.0148 ± 0.0004	(ns)	(ns)	(ns)	(ns)	0.994
0.00055583	3.26 ± 0.04	0.0168 ± 0.0004	(ns)	(ns)	(ns)	(ns)	0.994
0.00041615	3.55 ± 0.04	0.0186 ± 0.0004	(ns)	(ns)	(ns)	(ns)	0.995
0.00031372	3.91 ± 0.04	0.0205 ± 0.0005	(ns)	(ns)	(ns)	(ns)	0.995
0.00023315	4.39 ± 0.05	0.0235 ± 0.0005	(ns)	(ns)	(ns)	(ns)	0.995

Table 3-6 Coefficient for transverse relaxation rates (R_2) equation for $GdCl_3$ at all field strengths tested. (ns) indicate not significant with p-value > 0.05

Field Strength	$a_{2,2,0}$ (s^{-1})	$a_{2,2,1}$ $(\mu M \cdot s)^{-1}$	$a_{2,2,2}$ $(ppm \cdot s)^{-1}$	$a_{2,2,3}$ $(\mu M^{-2} \cdot s^{-1})$	$a_{2,2,4}$ $(ppm^{-2} \cdot s^{-1})$	$a_{2,2,5}$ $(\mu M \cdot ppm \cdot s)^{-1}$	Adjusted-R^2
3	11.3 ± 1	0.019 ± 0.005	0.73 ± 0.08	(ns)	-0.0065 ± 0.0025	(ns)	0.978
1.5	9.9 ± 1.1	0.022 ± 0.006	0.82 ± 0.09	(ns)	-0.0073 ± 0.0027	(ns)	0.979

3.2.5 NMRD relaxivity modelling

The relaxivity dependency to magnetic field strength was plotted on nuclear magnetic relaxation dispersion (NMRD) profiles for each metal salt at 25 °C in the gellan gum gel environment in Figure 3-6. Plotting the linear effect from either metal salt to the magnetic field strengths generates

the NMRD relaxivity profile. The $MnCl_2$-induced relaxivity (Figure 3-6a) changes drastically at higher frequencies with a substantial change above 0.01 T; but below 0.01 T, the relaxivity is nearly constant similar to results seen in a pure aqueous environments [14]. The quadratic profile at higher magnetic field strengths was indicative of a large hindrance to the tumbling correlation time of the bounded hydrogen in the inner sphere [15]. The $GdCl_3$ NMRD is plotted in Figure 3-6b, and it shows a distinct relaxivity profile, compared to $MnCl_2$. A minor effect of field strength exists at the high magnetic field strengths where relaxivity initially decreases before increasing until the relaxivity begins to plateau. However, below 0.02 T the apparent dependency increases resulting in a large relaxivity at lower magnetic field strengths. This profile has been reported for contrast agents used in other gel structures or natural tissue [16,17]; however, the relaxivity in a pure aqueous environment approaches a constant value similar to the $MnCl_2$ profile. This suggest that the gelling structure has an influence on the relaxivity dependency for the $GdCl_3$-containing samples. Potentially the chelated gadolinium ions may still be interacting with the gellan gum structure crosslinking the gel and providing a differing relaxation environment. The movement of the hydrogens in the inner sphere near the gadolinium ions would be inhibited causing the profile to differ from aqueous environments and from the $MnCl_2$ profile thus providing a NMRD profile more typically seen in more restricted environments like tissues. Relaxivity of the SPIONs and the quadratic effect of the contrast agents were not shown as their effects were not significant through most of the magnetic field strengths tested

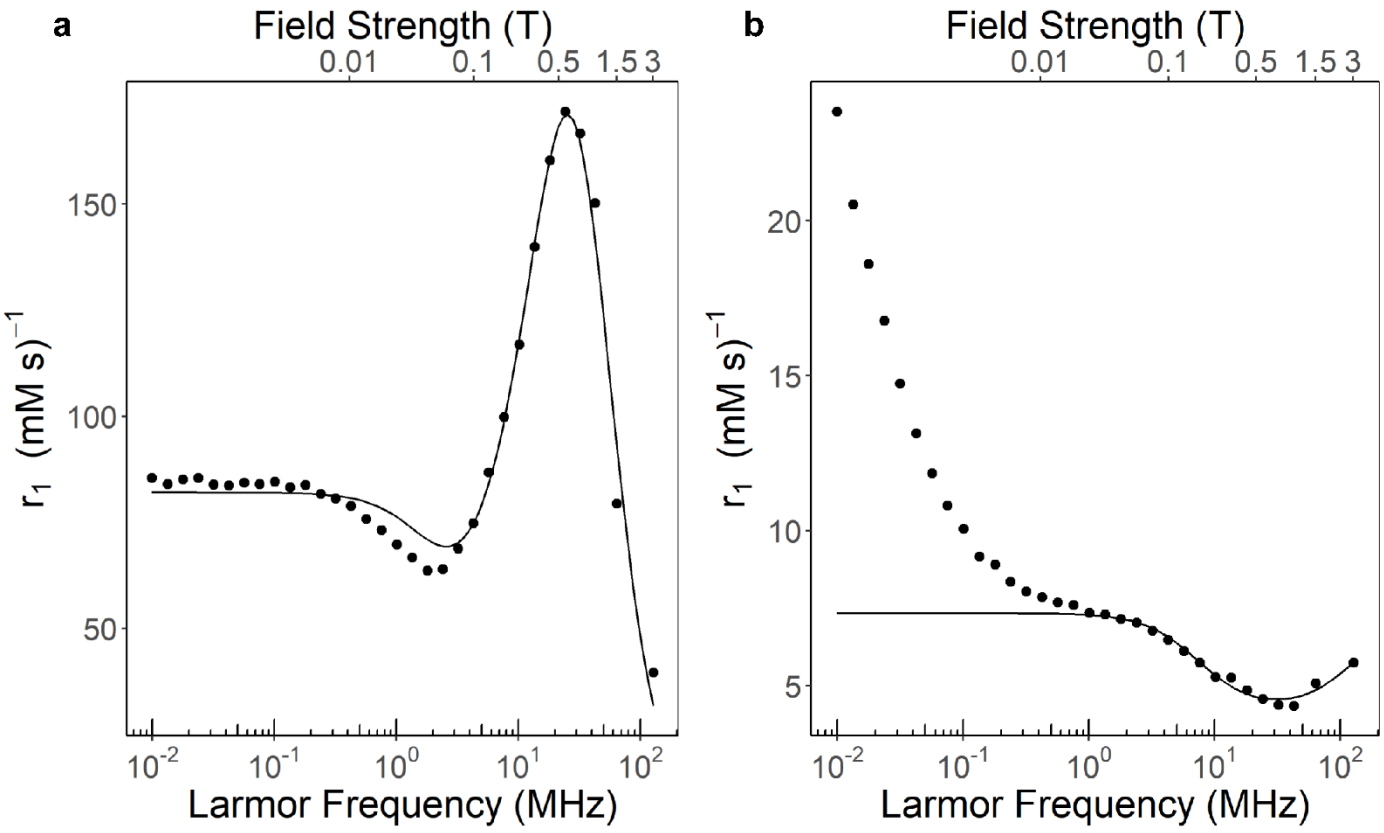

Figure 3-6 NMRD profiles modelled by Solomon-Bloembergen-Morgan theory for a) $MnCl_2$ and b) $GdCl_3$. Parameters are reported in Table 3-7.

The NMRD profiles were modelled by the Solomon-Bloembergen-Morgan (SBM) theory which fit a mathematical model to parameters relating to the physical relaxation of the inner sphere hydrogens [15]. Outer sphere relaxation effects were ignored, and focus was placed on the inner sphere relaxation due to the scope of the research and the limits in outer sphere relaxation in complexity and use of more general parameters. The SBM model coefficients are related to the relaxation characteristics of the nearby protons. However, the SBM model is not designed to properly predict low magnetic fields for slowly rotating objects [18], and the gel environment may have caused the protons to rotate slowly. The model was able to approximate the $MnCl_2$ system well as shown in Figure 3-6a, but since the $GdCl_3$ sample fails to reach a plateau, the model fails to fit the relaxivity at lower magnetic field strengths (Figure 3-6b). This was indicative of slowly rotating protons in the gelled environment with $GdCl_3$ system. Therefore, the $GdCl_3$ was modelled down to 0.02 T to generate the best-fit parameters. Modelled best-fit parameters can be found in

Table 3-7 for both metal salt relaxivity. The values were modelled through nonlinear regression in the statistical program R.

Table 3-7 NMRD best-fit parameters. * denotes parameters taken from literature [19–21]. ** fixed in the fitting procedure

Parameter	Description	$MnCl_2$	$GdCl_3$-DTPA
S	Total electron spin	5/2*	7/2*
q	Number of bound water molecules	1*	1*
r (nm)	Proton-metal ion distance	2.9*	3.13*
$A/\hbar$ (10^6 rad/s)	Hyperfine coupling constant	-37.9*	-3.9*
τ_m (ns)	Water correlation time	32.8 ± 5.2	130 ± 40
Δ^2 (10^{19} s^{-2})	Transient ZFS interaction	629 ± 66	2.00 ± 0.46
τ_v (ps)	Fluctuation correlation time	136.1 ± 7.3	8.0 ± 1.4
τ_r (ns)	Rotational correlation time	3000**	1.18 ± 0.13

3.2.6 MRI contrast agents doped in gel dosimeters

As one intended use of the MRI gel phantom was to be incorporated with image-guided radiation therapy quality assurance, the phantoms were doped with a molecule sensitive to ionizing radiation. Previous work in our lab [2] have utilized tetrazolium salts as the radiochromic compound within gellan gum hydrogels to produce a 3D gel dosimeter with an effective sensitivity at high stability as diffusion is suppressed during the reduction to an insoluble and coloured formazan species. To test the compatibility of the contrast agents with the dosimeters, gel phantoms with the highest concentrations of $MnCl_2$ and $GdCl_3$ (40 and 140 µM) from the previous experiment were added alongside 0.1 or 0.25 mM tetrazolium salts. Additional experiments with SPIONs were also conducted. The gels were doped with a tetrazolium salt developed in our lab 3-(6-methoxybenzothiazol-2-yl)-5-phenyl-2-(3-trifluoromethylphenyl) tetrazol-3-ium chloride [MBtPFP] shown in Figure 3-7. The trifluoromethyl functional group acted as an electron withdrawing group and the methoxybenzothiazol as electron donators. These side chains may

allow for chelates to form between the metal salts used enabling a more complex dosimetry analysis and the ability for MR dosimetry.

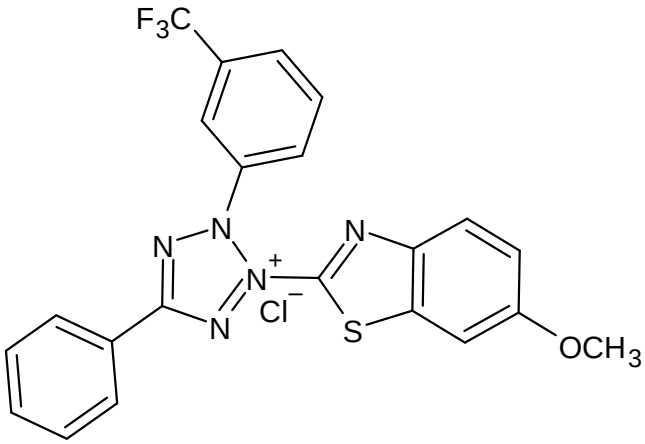

Figure 3-7 In-house developed tetrazolium salt (MBtPFP) chemical structure

The gels containing both metal salts and tetrazolium salts were then irradiated on a Cobalt-60 (^{60}Co) source at 0, 10, 20, and 40 Gy, as seen in Figure 3-8 with a peak delta absorbance at 520 nm for the MBtPFP regardless of the MRI contrast agent added.

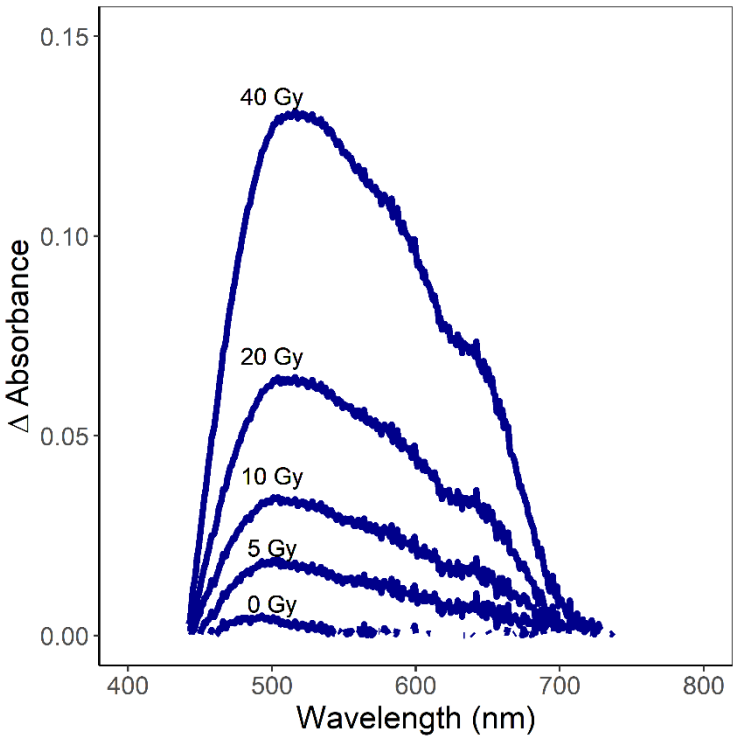

Figure 3-8 Difference in absorption profile of MBtPFP doped gels post-radiation with no MRI contrast agent present.

The results in Figure 3-9 indicate that the $MnCl_2$ reduces the sensitivity of the dosimeter. The reduction may be caused by $MnCl_2$ inhibiting the reduction of tetrazolium salts to formazan, or the results may indicate that the $MnCl_2$ is interacting with the tetrazolium species causing a chelate. $GdCl_3$ did not show any change to the absorption profile indicating that it may be used with the current system without a reduction to sensitivity.

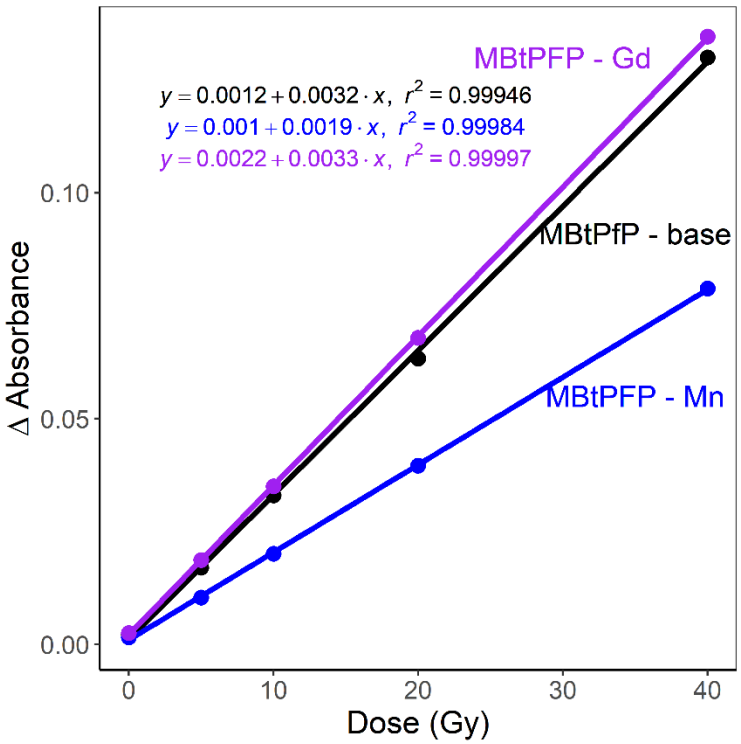

Figure 3-9 Difference in maximum absorbance (520 nm) of 0.1 mM MBtPFP doped gels at various dosage to compare the effect of metal salt additives on radiation dose sensitivity.

To compare the effect of the contrast agents to the radiation sensitivity, the contrast agents were added with both the new tetrazolium salt MBtPFP and bisnitrotetrazolium chloride (BNC) a common tetrazolium salt used in dosimetry (Figure 3-10). Both profiles had linear dose sensitivity at the dosages tested (0 to 40 Gy); however, further analysis with dose rate effects may be of interest. The difference in peak absorbance is reduced indicating a reduction in radiation sensitivity in the doped $MnCl_2$ gels regardless of tetrazolium specie. The MBtPFP resulted in a more sensitive compound compared to the BNC whether doped or not with undoped BNC sensitivity being slightly more sensitive than doped MBtPFP. The SPIONs faired similarly to the $GdCl_3$ with no large change to sensitivity which was unexpected as some research [22] suggest that SPIONs may increase the effect of radiation dose by catalyzing the radiolysis of water. However, the SPIONs may primarily be inducing reactive oxygen species (OH^-, H_2O_2, and O_2^-) to form by the acting as a catalyst either with released iron or the surface of the SPION in the Haber-Weiss cycle and therefore for the Fenton reaction [22]. The reactive oxygen species are then being scavenged by the oxidizing radical scavenger propylene glycol. Propylene glycol is needed as an oxidizing agent scavenger as oxidizing radicals may induce a backwards reaction by the oxidation of the coloured

formazan into a tetrazolium salt. This would cause a time-varying response and instability. Therefore, these scavengers are necessary to allow stability of the signal over time. However, further analysis may prove a more complete dosimetry analysis of the phantom including the effects of a magnetic field on the ionizing radiation dosimetry.

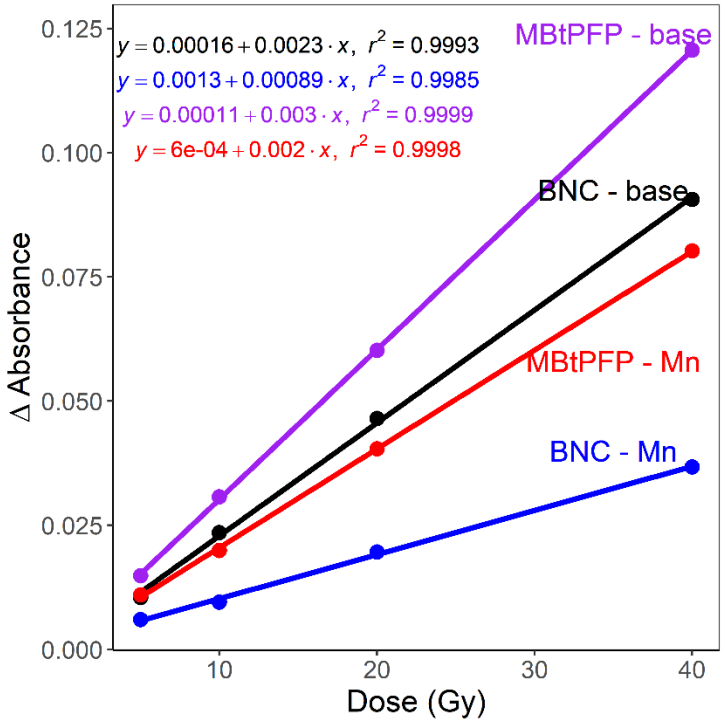

Figure 3-10 Difference in maximum absorbance of gels doped with 0.25 mM of either MBtPFP or BNC with or without $MnCl_2$ as an additive to illustrate the effect of $MnCl_2$ on dose sensitivity for two separate tetrazolium salt compounds.

As an additional test, the doped gel dosimeters were scanned within a 3 T MRI scanner to determine if any change in the local magnetic environment for the contrast agent has occurred with the presence tetrazolium or formazan salts. Again, both BNC and MBtPFP were implemented into MRI gel phantoms with $MnCl_2$ and experienced a series of radiations. BNC was used as a control because previous research in our lab showed no change in BNC magnetic environment with ionizing radiation. With MBtPFP, no large change in the T_1 relaxation times occur from total dose seen in Table 3-8. Additionally, the T_1 relaxation times for both BNC and MBtPFP are similar

indicating no change from species. These results indicate that the local magnetic environment of the metal salt has not changed with the addition of tetrazolium salt or formazan meaning the tetrazolium gel dosimeters are not capable to distinguish dose with MRI. Concluding that either the metal salt has not formed a chelate with the tetrazolium salt or an inhibited reduction pathway from the presence of $MnCl_2$.

Table 3-8 MRI results for tetrazolium gel dosimeters doped with $MnCl_2$

Tetrazolium	Dose	T_1	error
BNC	0	148.6	1.34
BNC	40	147.9	0.78
MBtPFP	0	148.7	0.11
MBtPFP	5	150.6	1.07
MBtPFP	10	149.6	0.021
MBtPFP	20	149.2	0.05
MBtPFP	40	149.0	0.18

3.9 Bibliography

[1] Mohammed L, Ragab D, Lin S, Said S, Gomaa H, Mequanint K. Preparation and Characterization of Glycol Chitosan-Fe 3 O 4 Core–Shell Magnetic Nanoparticles for Controlled Delivery of Progesterone. J Biomater Tissue Eng 2017;7:561–70. doi:10.1166/jbt.2017.1603.

[2] Penev KI, Wang M, Mequanint K. Tetrazolium salt monomers for gel dosimetry I: Principles. J Phys Conf Ser 2017;847. doi:10.1088/1742-6596/847/1/012048.

[3] Chang S, Lamm SH. Human health effects of sodium azide exposure: a literature review and analysis. Int J Toxicol 2015;22:175–86. doi:10.1080/10915810390201145.

[4] Andersen AF. Final amended report on the safety assessment of Methylparaben, Ethylparaben, Propylparaben, Isopropylparaben, Butylparaben, Isobutylparaben, and Benzylparaben as used in cosmetic products. Int J Toxicol 2008;27 Suppl 4:1–82. doi:10.1080/10915810802548359.

[5] Nalawade T, Sogi SP, Bhat K, Bhat K, Sogi SHP, Sogi SHP, et al. Bactericidal activity of propylene glycol, glycerine, polyethylene glycol 400, and polyethylene glycol 1000 against selected microorganisms. J Int Soc Prev Community Dent 2015;5:114. doi:10.4103/2231-0762.155736.

[6] Penev KI, Mequanint K. Methylthymol blue in Fricke gels. J Phys Conf Ser 2015;573:012030. doi:10.1088/1742-6596/573/1/012030.

[7] Montgomery DC. Design and Analysis of Experiments. 6, revised ed. New York: John Wiley & Sons; 2007.

[8] Wu W, He Q, Jiang C. Magnetic iron oxide nanoparticles: Synthesis and surface functionalization strategies. Nanoscale Res Lett 2008;3:397–415. doi:10.1007/s11671-008-9174-9.

[9] Kato H, Kuroda M, Yoshimura K, Yoshida A, Hanamoto K, Kawasaki S, et al. Composition of MRI phantom equivalent to human tissues. Med Phys 2005;32:3199–208. doi:10.1118/1.2047807.

[10] Villafranca JJ, Yost FJ, Fridovich I. Magnetic Resonance Studies of Manganese and Iron (III) Superoxide Dismutases. J Biol Chem 1974;249:3532–6.

[11] Rabiet M, Brissaud F, Seidel JL, Pistre S, Elbaz-Poulichet F. Positive gadolinium anomalies in wastewater treatment plant effluents and aquatic environment in the Hérault watershed (South France). Chemosphere 2009;75:1057–64. doi:10.1016/j.chemosphere.2009.01.036.

[12] Gale EM, Atanasova IP, Blasi F, Ay I, Caravan P. A Manganese Alternative to Gadolinium for MRI Contrast. J Am Chem Soc 2015;137:15548–57. doi:10.1021/jacs.5b10748.

[13] Howe FA. Relaxation times in paramagnetically doped agarose gels as a function of temperature and ion concentration. Magn Reson Imaging 1988;6:263–70. doi:10.1016/0730-725X(88)90400-6.

[14] Aime S, Anelli P, Botta M, Brocchetta M, Canton S, Fedeli F, et al. Relaxometric evaluation of novel manganese(II) complexes for application as contrast agents in magnetic resonance imaging. JBIC J Biol Inorg Chem 2002;7:58–67. doi:10.1007/s007750100265.

[15] Lauffer RB. Paramagnetic Metal Complexes as Water Proton Relaxation Agents for NMR Imaging: Theory and Design. Chem Rev 1987;87:901–27. doi:10.1021/cr00081a003.

[16] Gossuin Y, Burtea C, Monseux A, Toubeau G, Roch A, Muller RN, et al. Ferritin-induced relaxation in tissues: An in vitro study. J Magn Reson Imaging 2004;20:690–6. doi:10.1002/jmri.20152.

[17] Araya YT, Martínez-Santiesteban F, Handler WB, Harris CT, Chronik BA, Scholl TJ. Nuclear magnetic relaxation dispersion of murine tissue for development of T 1 (R 1) dispersion contrast imaging. NMR Biomed 2017;30:e3789. doi:10.1002/nbm.3789.

[18] Ferreira MF, Mousavi B, Ferreira PM, Martins CIO, Helm L, Martins JA, et al. Gold nanoparticles functionalised with stable, fast water exchanging Gd3+chelates as high relaxivity contrast agents for MRI. Dalt Trans 2012;41:5472–5. doi:10.1039/c2dt30388d.

[19] Patinec V, Rolla GA, Botta M, Tripier R, Esteban-Gómez D, Platas-Iglesias C. Hyperfine coupling constants on inner-sphere water molecules of a triazacyclononane-based Mn(II) complex and related systems relevant as MRI contrast agents. Inorg Chem 2013;52:11173–84. doi:10.1021/ic4014366.

[20] Troughton JS, Greenfield MT, Greenwood JM, Dumas S, Wiethoff AJ, Wang J, et al. Synthesis and evaluation of a high relaxivity manganese(II)-based MRI contrast agent. Inorg Chem 2004;43:6313–23. doi:10.1021/ic049559g.

[21] Merbach A, Helm L, Toth E. The Chemistry of Contrast Agents in The Chemistry of Contrast Agents in. John Wiley & Sons; 2013.

[22] Klein S, Sommer A, Distel LVR, Neuhuber W, Kryschi C. Superparamagnetic iron oxide nanoparticles as radiosensitizer via enhanced reactive oxygen species formation. Biochem Biophys Res Commun 2012;425:393–7. doi:10.1016/j.bbrc.2012.07.108.

Chapter 4

4 Mechanical and electrical properties of LiCl-doped gellan gum gels

4.1 Overview

In this Chapter, the effects of gelling agent, propylene glycol (PG), and lithium chloride (LiCl) concentrations to both mechanical and electrical properties of gellan gum gels prepared at different concentrations is described. The stress-strain curve of each composition was used to determine the compressive modulus at a defined strain, the ultimate compressive stress, and the fracture strain. For electrical properties, a dielectric spectroscopy for frequency response analysis was used to determine the complex impedance of the material housed in a built cell. The complex impedance was matched with a resistive and reactance parts in series to generate the real and imaginary components. The relative electric permittivity and conductivity of the samples were then calculated. Finally, a design of experiments was implemented to categorize and model each effect of compositions to have tailorable properties.

4.2 Methodology

4.2.1 Gel preparations

Gellan gum gels were prepared similar to the MRI phantoms discussed in the Chapter 3.2.2. However, instead of MRI contrast agents, monovalent metal salts were added at various concentrations (50 to 100 mM). Additionally, the concentrations of propylene glycol and gellan gum were varied. Gellan gum was used as the sole gelling agent thus the integrity of the hydrogel depends on its concentrations, also as propylene glycol is added to better homogenize the final gel it may also affect the mechanical and electrical properties. From preliminary experiments, it was determined that a stable hydrogel capable for testing existed from gellan gum concentrations above 0.5 % (w/v). When the gellan gum concentrations is more than 1 % (w/v), addition of salt caused immediate crosslinking and inhomogeneity during gelling. The propylene glycol concentration varied from 5 to 10 % (v/v) based on preliminary experiments as hydrogels below 5 % (v/v) caused inhomogeneity when filled in the molds and the upper limit was set at 10 % (v/v) to maintain a

high-water content. The final gel solutions were poured into their respective molds for either electrical, mechanical, or optical measurements.

4.2.2 Experimental sample preparation for mechanical testing

For mechanical tests, the final gel solutions were poured into cylindrical polypropylene molds fabricated from disposable polypropylene syringes (Figure 4-1). The syringes were cut such that the diameter was equivalent to the height (13x13 mm). The gel solutions were poured into the molds and were left to set for 12 h at room temperature.

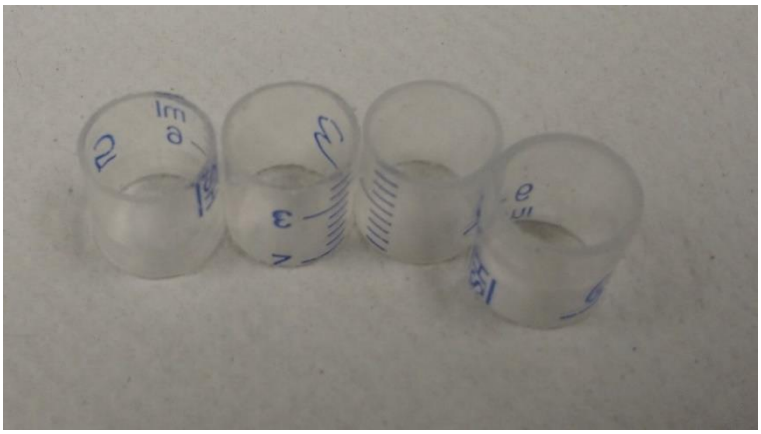

Figure 4-1 Cut cylindrical molds to prepare gel specimens for mechanical experiments

Uniaxial compression test was conducted using an Instron Universal Mechanical testing machine equipped with either a 10 N (for preliminary) or 50 N (for the full analysis) load cells (Instron model 3345, Canton, MA) at 20 mm/min. Stress was calculated from the applied force per initial cross-sectional area of the cylindrical specimen. Strain was calculated as the change in height over the initial height of the cylindrical gel. The diameter and height of the gel were measured by a digital caliper with an average of multiple measurements after removing the mold. The gels were compressed without their mold in unconstrained compressive tests until fracture. A crosshead speed of 20 mm/min was chosen to stimulate the compressive deformation. For preliminary experiments, a base gel was used as a control with compositions similar to the MRI phantoms developed in Chapter 3 with 1.25 % (w/v) gellan gum and 10 % (v/v) PG. Additional compositions tested the extent of gellan gum and PG concentrations to determine the compositions for a design of experiments. Furthermore, the experiments included lithium chloride (LiCl), lithium formate (Li-formate), and tetramethylammonium chloride (TMA-Cl) at 50 mM to examine the effect of

each salt. Li-formate may provide additional benefits apart from increasing conductivity, if the gels are to be used in tetrazolium dosimetry [1] and TMA-Cl has been used previously to crosslink gellan gum phantoms [2]. For the design of experiments, eight distinct compositions (each with six repetitions) were utilized and can be seen in Table 4-1 based off Figure 2-7. The gels were left in their molds overnight and during transport to maintain the high-water content for consistent measurements and were removed immediately prior to mechanical testing.

Table 4-1 Gel compositions for designed electrical and mechanical analysis

#	Gellan gum %	PG %	LiCl (mM)
1	0.6	5	50
2	1	5	50
3	0.6	10	50
4	1	10	50
5	0.6	5	100
6	1	5	100
7	0.6	10	100
8	1	10	100

4.2.3 Sample preparations and cell fabrication for electrical testing

For electrical measurements, the gels were poured into in-house fabricated cells. The cells main structure were plastic plotting boxes typically used in the designing of circuits and electrical analysis (enclosure - plastic potting box, part no. 1596B101; Hammond Manufacturing Ltd., Guelph Ontario, Canada). Two conductive electrodes of graphite sheet [0.6 x 105 x 160 mm] (reference number: 02.06.060; NOVOTEC; Cincinnati, Ohio) were attached with epoxy glue to the ends of the plotting box. The electrodes were chosen as they are a highly conductive surface and are a form of carbon paper useful in fuel cells due to the high surface area, thin thickness, and high mechanical stability. The area of the electrode was equal to the area of the plotting box side (18 x 14 mm)), and the distance between the load cells were measured for the calculations (21.8 mm). The final cell schematic can be seen in Figure 4-2.

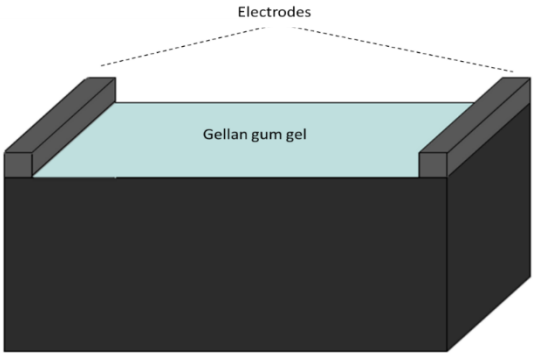

Figure 4-2 Manufactured cell holder schematic with gels filled between two electrodes

As indicated by Figure 2-4 (Chapter 2), a waveform generator (Wavetek FG3B sweep function generator, Wavetek San Diego, USA) was set in series with a known resistor of 100 kΩ and the fabricated cell filled with gel. A voltage of approximately 1 V was provided by the waveform generator at a multitude of frequencies. To measure the voltage drop and the phase separation, an oscilloscope (PicoScope PC Oscilloscope, Pico Technology, Cambridgeshire, UK) was used. The oscilloscope contained two channels, enabling the voltage drop across the circuit and the voltage drop across the dielectric material to be calculated independently. With the two voltage drops and the phase separation between them, and assuming an equivalent circuit design for the dielectric material, the real and imaginary parts of the impedance for the dielectric material can be calculated, allowing for the relative permittivity and conductivity to be found. The same compositions listed in Table 4-1 were used in the electrical analysis to relate the electrical tests with mechanical properties. The frequency range tested varied from 10 Hz to 2 MHz; however, at lower frequencies due to the polarization of the interface of the electrode and dielectric material large relative permittivity may arise [3]. At higher frequencies (greater than 500 kHz) the copper wires used to make the circuit and other electronic components will generate inductance effects increasing the current flow. By contrast, at high frequencies, the change in electric properties in some tissues become more stagnant [4,5].

4.3 The effect of gel composition on mechanical properties

A typical stress-strain curve of the hydrogels is plotted in Figure 4-3 indicating a combined elastic and plastic deformation seen in typical viscoelastic materials including tissues [6,7]. The stress-

strain curve was fitted by a polynomial equation of degree 3 by regression and resulted in an R^2 (>0.99) for all compositions tested.

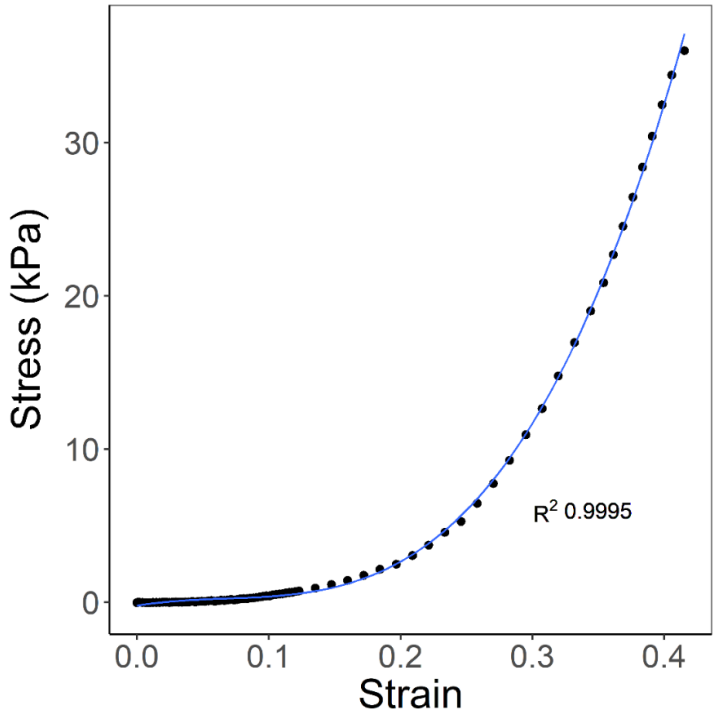

Figure 4-3 Typical stress-strain curve for the base gel with 1.25 % (w/v) gellan gum and 10 % (v/v) PG with a third-degree polynomial fit.

With the fitted equation, the compressive modulus of a viscoelastic material at a particular strain can be found by taking the derivative of the polynomial equation. Once the derivative equation is found the value for strain can be inserted to evaluate for compressive modulus at the particular strain. The compressive modulus was evaluated at 0.25 strain as a common point among all gels, as all gels were capable of strains up to 0.25 without fracturing and the gels are not expected to experience strains greater than 25 % in practical use. The ultimate compressive stress and fracture strain were taken at a point where the stress-strain curve reached a maximum value and fractured. The mechanical properties of the gels at different compositions are shown in Figures 4-4a-c. The base gel (1.25 % (w/v) gellan gum and 10 % (v/v) PG) is compared to other compositions containing a crosslinking salt (LiCl, Li-Formate, and TMA-Cl) at lowered gellan gum concentrations which still enabled a homogenous gel. A sample size of six for each composition was implemented.

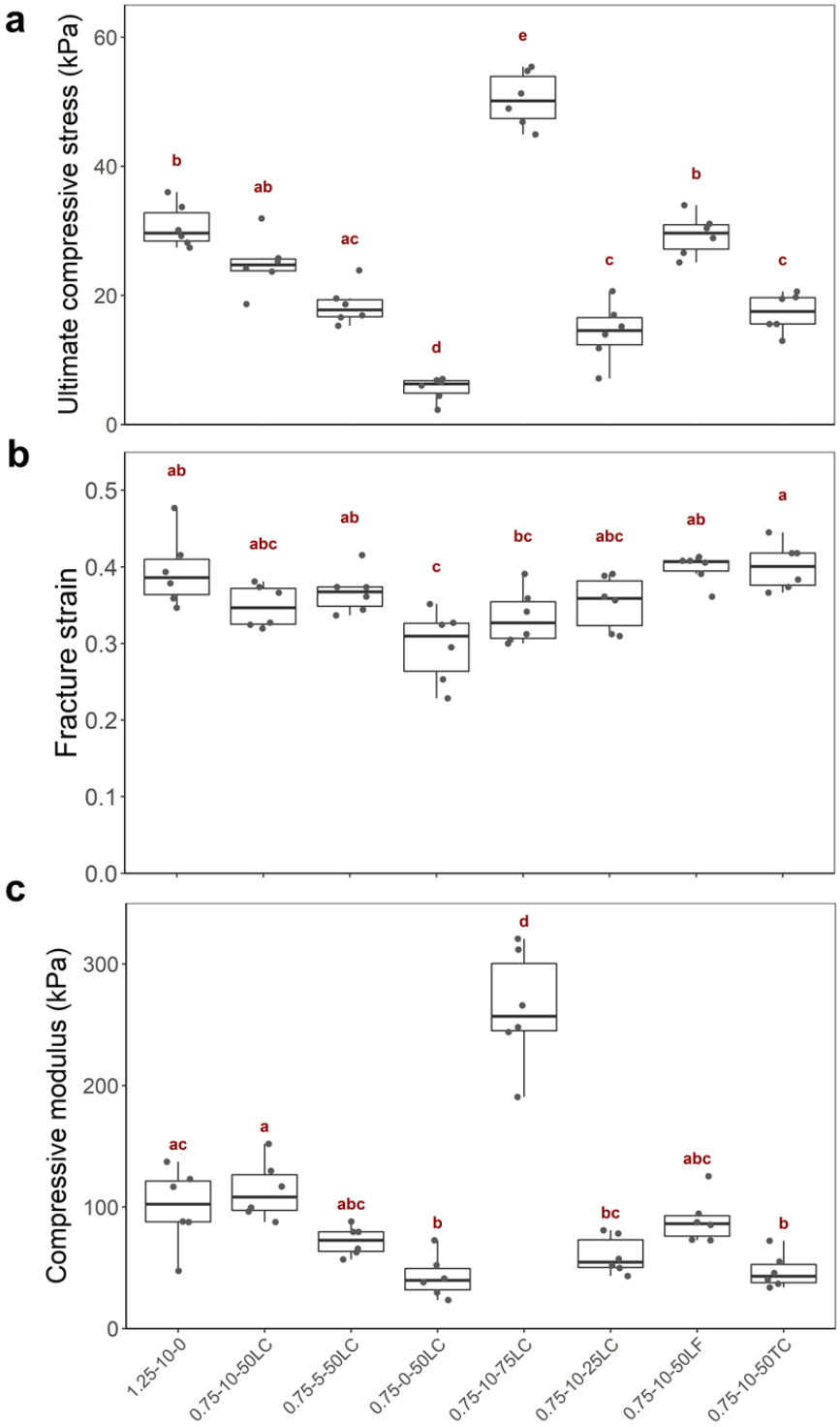

Figure 4-4 Mechanical properties of doped gellan gum gels plotted at various compositions with the x-axis denoted by % gellan gum, % PG, and mM ion (LC is LiCl, LF is Li-formate, and TC is TMA-Cl) respectively. Where (a) is ultimate compressive stress, (b) is the fracture strain, and (c) is the compressive modulus at 0.25 strain. Significance is denoted with unique characters

Figure 4-4a demonstrated the ultimate compressive stress of the gel phantoms with varying compositions. By decreasing the PG concentration, the gels ultimate compressive stress decreased with the weakest gel occurring at 0% PG. Increasing the salt had the largest positive effect on the resulting ultimate compressive stress. The cation used had an effect where TMA-Cl had a lowered ultimate compressive stress on average. Additionally, TMA-Cl is toxic, and therefore was excluded from further studies. Since the effect of Li-formate was similar to that of LiCl further studies were conducted using LiCl due to ease of availability. The fracture strain for the same compositions is shown in Figure 4-4b where no distinct relation can be determined with salt type, PG concentration, or salt concentrations. Therefore, the material fracture strain is not strongly dependent on the concentrations tested. The compressive moduli are plotted in Figure 4-4c showing a similar relation as the ultimate compressive stress with the salt type and concentration, and PG concentration, all affecting the compressive modulus of the gels. These results indicated that LiCl as a suitable salt due to its solubility in an aqueous environment and minimal toxicity, lower cost, and is still able to induce crosslinking. The PG concentrations below 5 % (v/v) showed heterogeneities when poured into the mechanical testing molds; and therefore, concentrations were constrained from 5 to 10 % (v/v) for future tests. Increasing the propylene glycol amount also decreases the water concentration lowering the tissue equivalency; therefore, a limit to 10% propylene glycol was used. The gellan gum concentration was set between 0.6 to 1 % (w/v) to analyze the effect of gelling agent. Gels doped with monovalent salts begin to flow at gelling agent concentrations at 0.5% and gels above 1% instantly became rigid gels and may form heterogeneous systems. Lastly, the LiCl was ranged from 50 to 100 mM to ensure sufficient crosslinking. At these concentrations, we expect to find similar tissue equivalency for electrical properties to match the electrolyte compositions in tissues. The plot also indicates that gels with similar mechanical properties to the gels used previously in our lab may be reached with a lower concentration of gelling agent by adding monovalent salts. The mechanical properties data shown from Figures 4-4 provided useful trends on the role of each constituent.

Building on these, design of experiments approach was taken to optimize the effects of each constituent. Data collectively presented in Figure 4-5a-c showed the effects of gellan gum, propylene glycol, and LiCl concentrations for the design of experiments.

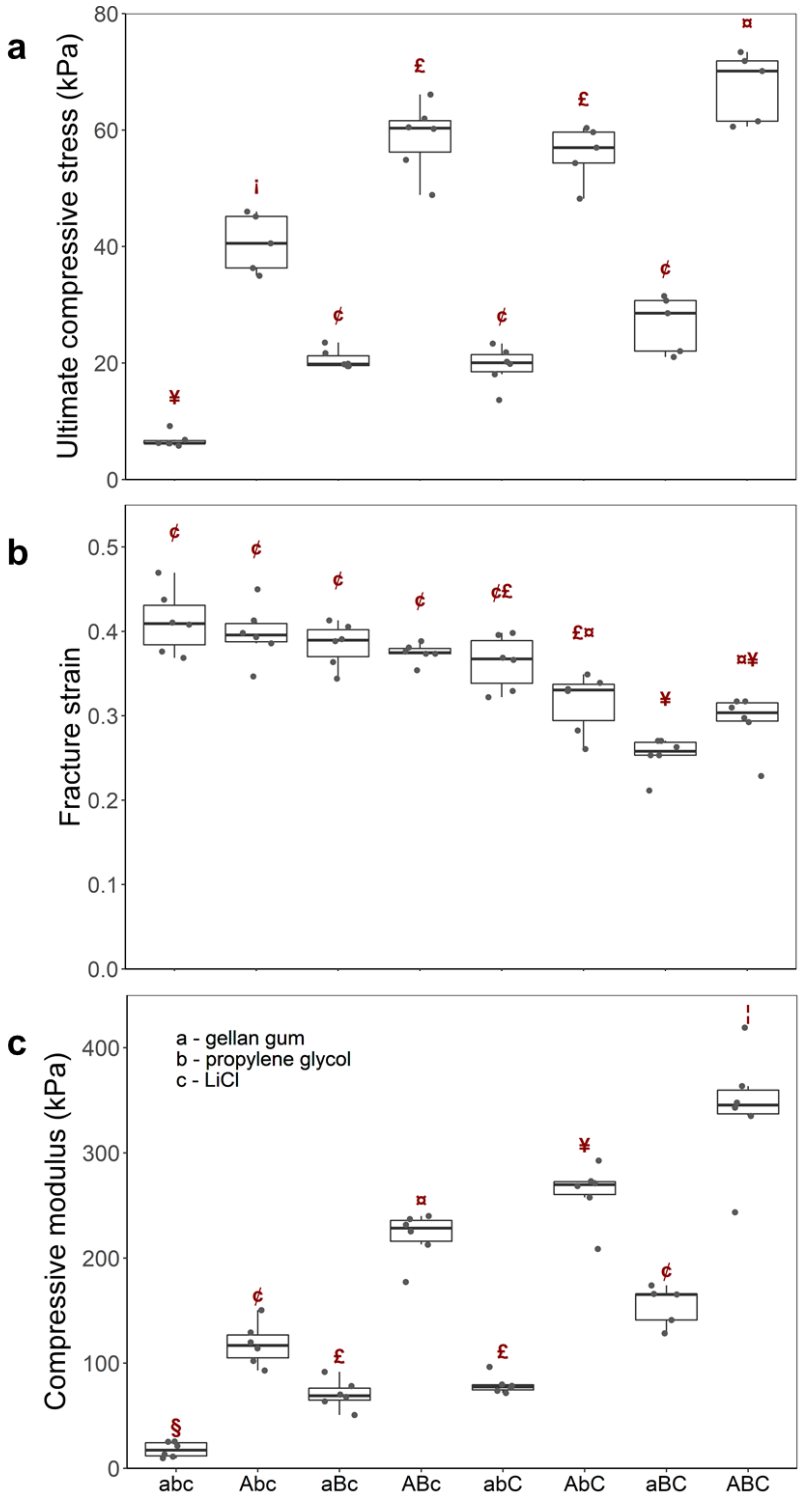

Figure 4-5 Mechanical properties of the designed experiment with (a) for the ultimate compressive stress, (b) for the strain at fracture, and (c) for the compressive modulus at 0.25 strain for different compositions where lower case letters denote low concentration and capital letters denote high concentration. Significance is denoted with unique characters.

The box plots indicate that the three compositions all have a positive effect on gels ultimate compressive stress and compressive modulus. However, the fracture strain does not appear to follow a distinct pattern with the gel's compositions with a minor reduction with ion concentration. For the design experiment, outliers (failed Dixon's Q-test at a 95% confidence) were removed. To quantify the effects, a regression was made containing the base, linear, and interactive effects of all compounds for the ultimate compressive stress, fracture strain, and compressive modulus. ANOVA was used to determine the significant parameters, shown in Appendix I, and the model was rebuilt through regression with only the significant terms. The resulting terms can be found in equations (4-1) and (4-2) for ultimate compressive stress and compressive modulus. The strain is not shown as the model failed to accurately predict the variance and the effects of composition to fracture strain.

$$\sigma_m = -86.8 + 93.1 \cdot C_{gn} + 4.47 \cdot C_{PG} + 0.41 \cdot C_{LiCl} - 0.026 \cdot C_{PG} \cdot C_{LiCl} \quad \text{[kPa]} \tag{4-1}$$

Where σ_m is the ultimate compressive stress C_{gn} is the gellan gum concentration in % (w/v), C_{PG} is the propylene glycol concentration in % (v/v), and C_{LiCl} is the LiCl concentration in mM.

$$E_{\varepsilon=0.25} = -135 + 18.4 \cdot C_{gn} + 3.42 \cdot C_{PG} - 0.75 \cdot C_{LiCl} + 15 \cdot C_{gn} \cdot C_{PG} + 3.7 \cdot C_{gn} \cdot C_{LiCl} \quad \text{[kPa]} \tag{4-2}$$

Where $E_{\varepsilon=0.25}$ is the compressive modulus at 0.25 strain.

For the ultimate compressive stress, the base effect was significant as were the linear parameters of all compositions tested (gellan gum, PG, and LiCl) as expected. The only significant interaction was between PG and LiCl and was negative suggesting that at higher concentrations of PG and LiCl, the interactions between the materials will weaken the gel. The adjusted R^2 value for the ultimate compressive stress model was 0.957 indicating a close approximation of the model. When testing the model, the system fails to accurately characterize the effects of low concentrations of gellan gum (at or below 0.5 % (w/v)) which is likely caused by the unstability to remain a rigid gel and is in the process of transitioning into a solution with flow. For the compressive modulus, again the base effect and all linear parameters were significant. However, the effect of LiCl without any other parameter is negative meaning that LiCl reduces the gellan gums compressive modulus at 0.25 strain. This seems counterintuitive from the general trends seen in Figure 4-5 with gels containing higher concentrations of LiCl leading to stiffer gels. However, the linear component is

only one aspect, and the interaction of LiCl to the other parameters may explain this discrepancy. From the yields stress, the interaction between the gellan gum and the PG and the interaction between the gellan gum and LiCl was significant and positive indicating that the gellan gum interactions with PG or LiCl will increase the compressive modulus of the material. Therefore, the general increase in mechanical properties from LiCl can be attributed to the interaction between LiCl and gellan gum. Again, the adjusted R^2 value indicated a reasonable fit with 0.970. To better characterize the fracture strain, a more elaborate experiment may be required determining additional effects or a nonlinear regression may produce significant terms. However, if the effects are minor, no form of modelling will provide a definitive answer indicating that the fracture strain is not dependent on the compositions.

The gellan gum concentration and LiCl concentration will directly impact the gel matrix and the degree of crosslinking strengthening the gel [8], and therefore their effects were expected. However, PG acts as a co-solvent and is not directly related to the gel matrix when compared to the other parameters, so the large contribution seen in the results must be generated by other interactions. Previous research with high acyl gellan gum phantoms for ultrasound applications also indicated the significant effect of PG [9]. A possible reason why PG showed a noticeable effect may be due to the change of free water and bound water in the hydrogel by PG. Bound water refers to primary or secondary bounded water molecules onto sites on the gel network [10]. The gel matrix will continue to absorb water even after all sites are filled due to an osmotic driving force of the network chain and is eventually opposed by the crosslinking which causes an elastic retraction force. Therefore, an equilibrium swelling point occurs between the forces. Any additional water absorbed after the polymer matrix is fully bounded is referred to as the free water or bulk water that exist in the space between the network chains, pores, or voids. As PG concentrations increase, the total amount of water (bound or free) is reduced. However, PG may also bind to the polymer matrix and also will account for some of the free liquid existing between the polymer matrix as PG is slightly less polar than water. The total free liquid molecules may provide some incompressibility in the hydrogels. PG will not only displace some water it may also decrease the water activity due to cohesive linking between PG and water, a negative deviation from Raoult's law. Therefore, the water is bound to the gellan gum and also contains

intermolecular forces with PG in solution explaining the increase in mechanical integrity of the gels and the significant positive interactive effect between gellan gum and PG seen in the compressive modulus model. Previous research have investigated the intermolecular forces and electrostatic interactions between macromolecules in a dual liquid phase hydrogel system, also called coacervate, as a method to increase and tune mechanical properties [11,12]. An additional explanation may be related to the change in viscosity, as PG will increase the viscosity of solutions. A more viscous unbounded free-liquid molecules trapped within the gel matrix will require more stress to reach the same deformation leading to a stiffer material. Previous research comparing the gel strength and viscosity to the concentration of gel polymer or co-solvent polymer (polyethylene glycol), showed an increase of mechanical properties and viscosity [13,14]. The positive and linear effects of concentration whether PG, LiCl, or gellan gum seem to be true within the tested concentrations, but a limit may exist beyond the concentrations tested.

4.4 The effect of gel composition on electrical properties

Figure 4-6 to 4-8 illustrates the results from the dielectric spectroscopy of gellan gum gels doped at various LiCl concentrations. Figure 4-6 plots the calculated total impedance of the dielectric material based on an equivalent circuit with a resistive and a reactive part in series. The plot indicated three materials at two different LiCl concentrations and the base gel used similarly in the MRI phantoms. In the plot, the electrode polarization interference of the test cell can be seen with the large impendence values at low frequencies. At low frequencies, the dielectric material has sufficient time to create an interface at the electrodes causing polarization which in turn causes the apparent impedance to increase. However, the negative dependency of impedance to increasing frequency was expected and follows similar trends of other dielectric materials [15]. At higher frequencies, the impendence values reach a plateau where frequency change causes little change to the total impedance. At the extremes, large frequencies create induction effects for the copper circuitry adding electrical energy into the system and reducing the apparent impedance. However, the results indicated that the higher the salt concentration is, the lower the impedance will be, as the dielectric material allows greater current flow.

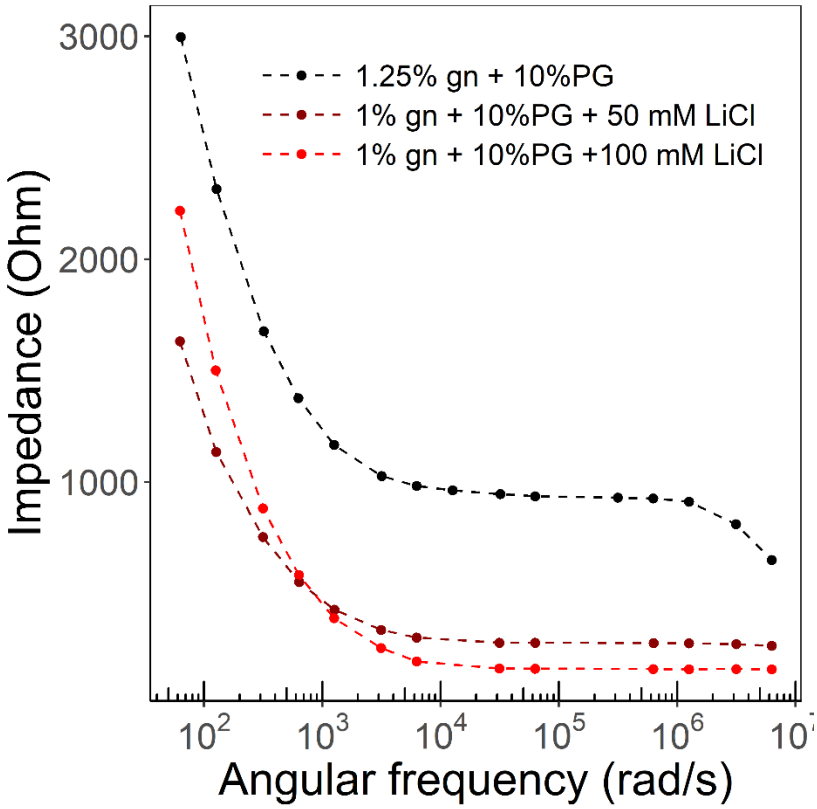

Figure 4-6 The total impedance of the dielectric material with differing LiCl concentrations at a range of frequencies showing some polarization and inductance effects.

The relative permittivity of the same compositions is plotted in Figure 4-7. The polarization has caused the low-frequency values to contain error, but the permittivity is a function of frequency and follows similar trends observed in tissues with a decrease in permittivity with frequencies in similar ranges [4,5]. Additionally, as the salt concentration increases the relative permittivity of the material seems to increase. The increase of relative permittivity is expected as the material is no longer storing the electrical energy in the polarization of the material and instead allows greater current flow through the material from the increased number of total ions.

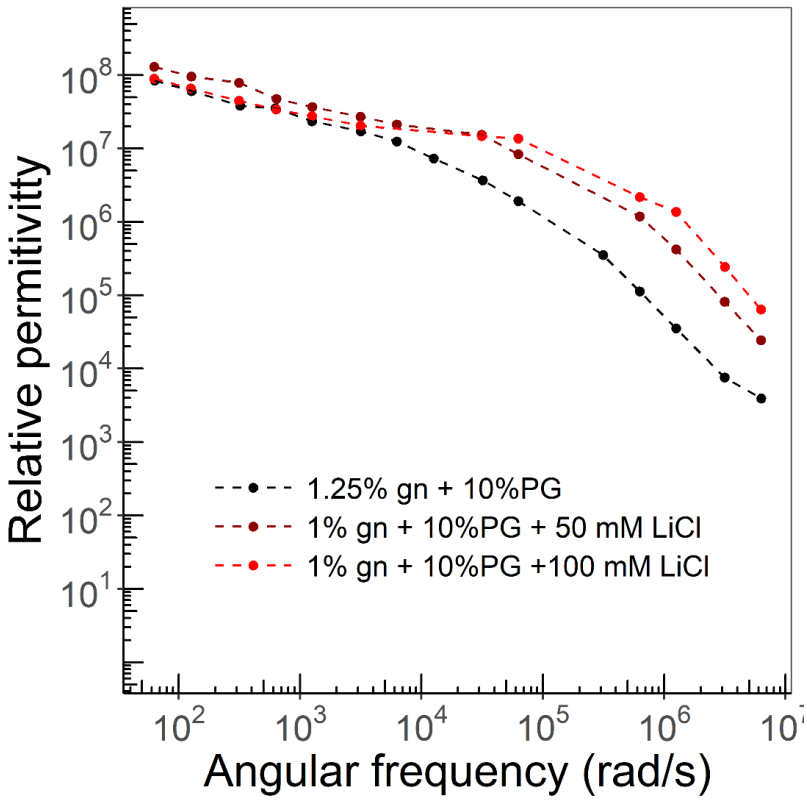

Figure 4-7 Relative permittivity of three gellan gum gels with differing LiCl concentrations at a range of frequencies.

The conductivity of the same compositions is plotted in Figure 4-8 and it demonstrated the large effect of LiCl on conductivity. The conductivity of a dielectric can also be stated as how "lossy" the material is to charges and is unable to store the energy by polarization and instead can convert the electrical energy to other forms of energy. The conductivity became three and five times larger with 50 and 100 mM LiCl, respectively. The trend with frequency also indicated an initial large increase which is compounded by interface polarization errors. At a certain frequency dependent on ion concentration, the conductivity begins to plateau to a relative constant value, and again at larger frequencies the apparent conductivity increases due to the inductance effects in the circuitry. A similar profile can be observed in previous hydrogel measurements [9] and tissues [5] with higher frequencies the conductivity is relatively consistent with less frequency variation.

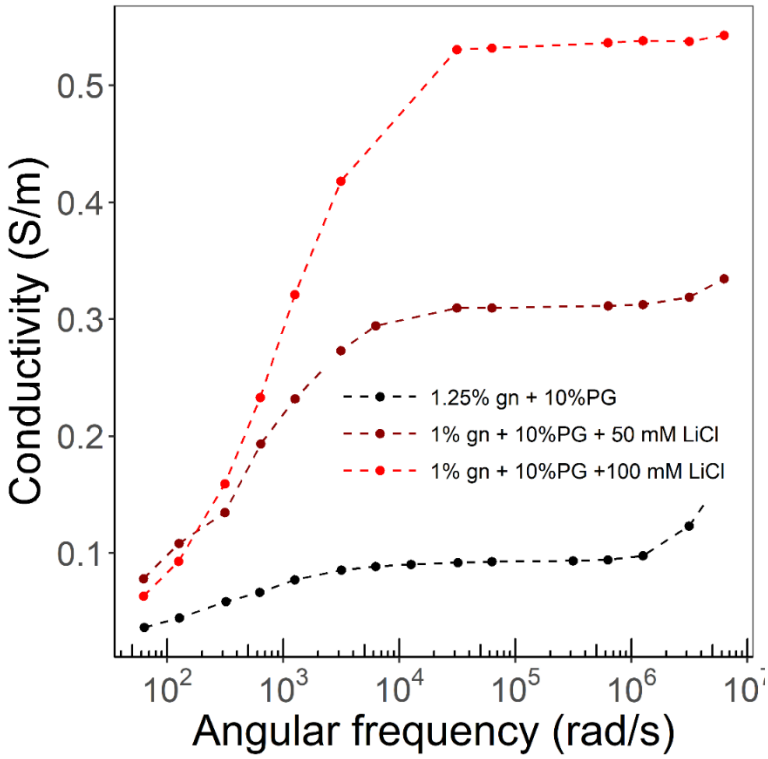

Figure 4-8 Conductivity of the dielectric material at a range of frequencies with differing LiCl concentrations.

To better characterize the hydrogels at a higher frequency, a more elaborate system is required that will not cause inductance in the circuitry. Comparing the results to tissues showed that the tissue also reaches a plateau at high frequency and any change is minor [5]. Often, the values are compared at one specific frequency at the plateau and is often depended on the intended application. Therefore, a bar graph with the conductivity at a frequency of 100 kHz with the eight compositions tested for the mechanical properties and the base gel as a point of comparison is shown in Figure 4-9. The only composition to have a large and positive effect is the LiCl. The PG and gellan gum concentrations did not appear to affect the conductivity of the gels greatly. Typical values for liver tissues are also plotted on the bar graph as a constant line. The difference from the base gel to tissues is large, but when gels are doped with LiCl the conductivity reaches values similar to tissues.

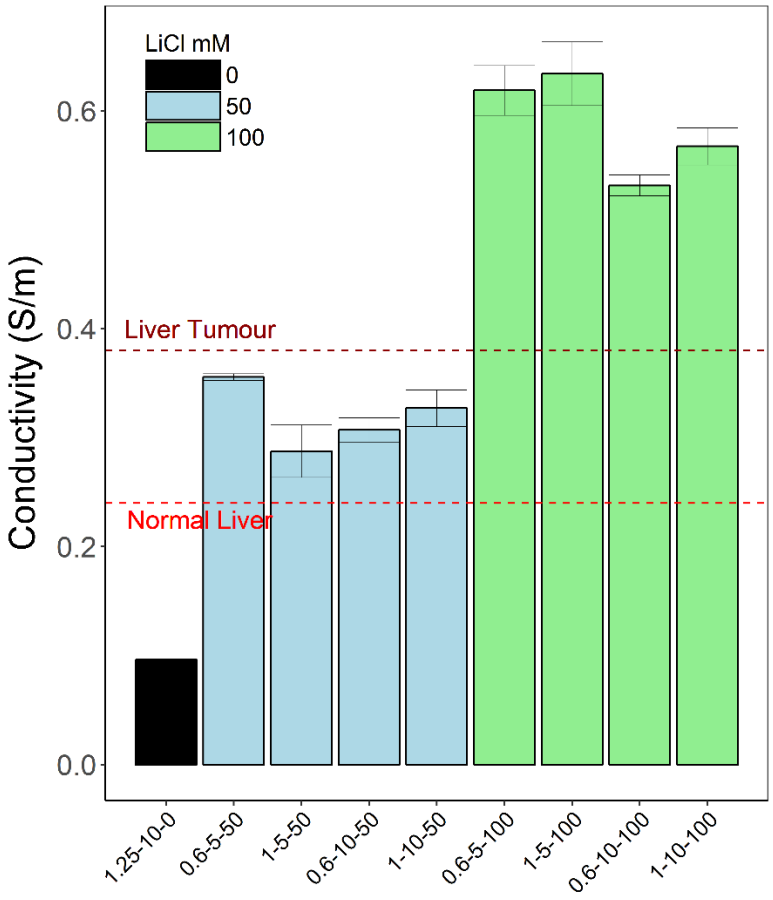

Figure 4-9 Conductivity of various gel samples compared to tissue conductivity. Where x-axis is coded by % gellan gum, % PG, and mM LiCl. The healthy and tumor liver conductivity values are plotted as dashed lines for comparisons and were found in [16].

To provide a quantitative analysis on the effects from compositions, the model was fit by a regression similar to the mechanical tests. ANOVA was used to determine significant terms from the base, linear effects of each additive, and the interaction between all additives. The model was refined to only include the significant terms, seen in Appendix J. The system is limited to the linear effects, but the results indicate a good fit (R^2 = 0.986).

$$\sigma_e = 0.16 - 0.0062 \cdot C_{PG} + 0.0044 \cdot C_{LiCl} \quad [\mathrm{S/m}] \qquad (4\text{-}3)$$

Where σ_e represents the conductivity in S/m of the dielectric material at 100 kHz, C_{PG} represents the % (v/v) of PG and C_{LiCl} represents the concentration of LiCl in mM. The base effect was significant as were the LiCl concentration linear effects as expected. The PG effect is less

significant and has a lower impact. The gellan gum concentration and any interaction terms were not significant. Indicating that the degree of crosslinking or the interaction between the metal ions and the gel matrix did not affect the electrical properties of the gel. The resulting model was able to accurately fit the data (R^2 = 0.986) even with only one repetition of the test. A higher number of repetitions may allow for greater modelling of the parameters. The conductivity of the gels at 100 kHz was not affected by interface polarization meaning that cell variability is minimal which is shown by the adjusted R^2 value. Also, at 100 kHz no inductance effect should be produced in the copper circuitry. The reasoning that the PG effect is significant and also negative may be caused by the lower overall water content in the gels reducing the mobility of the ions as PG will increase the viscosity. Additionally, PG is less conductive than deionized water resulting in a lower total conductivity of the hydrogel when PG concentrations are increased with a conductivity of 0.1×10^{-6} S/m compared to 5.5×10^{-6} S/m respectively.

4.5 Bibliography

[1] Penev KI, Wang M, Mequanint K. Tetrazolium salt monomers for gel dosimetry I: Principles. J Phys Conf Ser 2017;847. doi:10.1088/1742-6596/847/1/012048.

[2] Milas M, Shi X, Rinaudo M. On the physicochemical properties of gellan gum. Biopolymers 1990;30:451–64. doi:10.1002/bip.360300322.

[3] Getangama NNK. Dielectric Spectroscopy of Polyvinyl Alcohol Hydrogels and Nanocomposites. 2015.

[4] Gabriel C, Peyman A, Grant EH. Electrical conductivity of tissue at frequencies below 1 MHz. Phys Med Biol 2009;54:4863–78. doi:10.1088/0031-9155/54/16/002.

[5] Gabriel S, Lau RW, Gabriel C. The dielectric properties of biological tissues: II. Measurements in the frequency range 10 Hz to 20 GHz. Physiol Med Biol 1996;41:2251–69. doi:10.1088/0031-9155/41/11/002.

[6] Fung Y. Elasticity of soft tissues in simple elongation. Am J Physiol Content 1967;213:1532–44. doi:10.1152/ajplegacy.1967.213.6.1532.

[7] Krouskop TA, Wheeler TM, Kallel F, Garra BS, Hall T. Elastic moduli of breast and prostate tissues under compression. Ultrason Imaging 1998;20:260–74.

[8] Miyoshi E, Takaya T, Nishinari K. Rheological and thermal studies of gel-sol transition in gellan gum aqueous solutions. Carbohydr Polym 1996;30:109–19. doi:10.1016/S0144-8617(96)00093-8.

[9] Chen RK, Shih AJ. Multi-modality gellan gum-based tissue-mimicking phantom with targeted mechanical, electrical, and thermal properties. Phys Med Biol 2013;58:5511–25. doi:10.1088/0031-9155/58/16/5511.

[10] Hoffman AS. Hydrogels for biomedical applications. Adv Drug Deliv Rev 2012;64:18–23. doi:10.1016/j.addr.2012.09.010.

[11] Elbert DL. Liquid-liquid two-phase systems for the production of porous hydrogels and hydrogel microspheres for biomedical applications: A tutorial review. Acta Biomater 2011;7:31–56. doi:10.1016/j.actbio.2010.07.028.

[12] Hunt JN, Feldman KE, Lynd NA, Deek J, Campos LM, Spruell JM, et al. Tunable, high modulus hydrogels driven by ionic coacervation. Adv Mater 2011;23:2327–31. doi:10.1002/adma.201004230.

[13] Corbin EA, Millet LJ, Pikul JH, Johnson CL, Georgiadis JG, King WP, et al. Micromechanical properties of hydrogels measured with MEMS resonant sensors. Biomed Microdevices 2013;15:311–9. doi:10.1007/s10544-012-9730-z.

[14] Hackl E V., Khutoryanskiy V V., Tiguman GMB, Ermolina I. Evaluation of water properties in HEA-HEMA hydrogels swollen in aqueous-PEG solutions using thermoanalytical techniques. J Therm Anal Calorim 2015;121:335–45. doi:10.1007/s10973-015-4446-y.

[15] Warren H, Gately RD, O'Brien P, Gorkin R, In Het Panhuis M. Electrical conductivity,

impedance, and percolation behavior of carbon nanofiber and carbon nanotube containing gellan gum hydrogels. J Polym Sci Part B Polym Phys 2014;52:864–71. doi:10.1002/polb.23497.

[16] Haemmerich D, Staelin ST, Tsai JZ, Tungjitkusolmun S, Mahvi DM, Webster JG. In vivo electrical conductivity of hepatic tumours. Physiol Meas 2003;24:251–60. doi:10.1088/0967-3334/24/2/302.

Chapter 5

5 Conclusions and suggested future directions

This chapter concludes on the main results and topics of the thesis and ends with a list of possible future work to expand upon the knowledge gained.

5.1 Summary of thesis

In this thesis a gellan gum MRI phantom with tailorable magnetic relaxation properties was developed. SPIONs were prepared and their MRI relaxivity confirmed their possible use as an effective T_2 modifier with the potential for further modification with coating and preparation optimization. Using a central composite design of experiments (Figure 2-6), a mathematical model capable of linear, quadratic, and interactive effects was developed capable of predicting spin-lattice and spin-spin relaxation properties for a range of concentration of dopants. The model was shown to provide an accurate fit for both R_1 and R_2 relaxation rates (Tables 3-3 to 3-6). Adjusting the contrast agent concentrations would enable a wide range of tissue equivalent relaxation properties for the gellan gum samples (Figure 3-4c and f). The effect of temperature on the relaxation rate was found to be minimal. No measurable changes to the appearance of the gel or its optical density profile were observed after six weeks of storage at room temperature demonstrating that methyl 4-hydroxybenzoate and propylene glycol were effective preservatives (Figure 3-5). A unique central composite design was developed for either $MnCl_2$ or $GdCl_3$ in the gel phantom allowing a choice in relaxation modifier. The $MnCl_2$ phantom was more susceptible to magnetic field variation but requires lower concentrations to reach targeted relaxation times. The $GdCl_3$ phantom is less dependent on magnetic field variations but is associated with environment and health concerns. A major limitation to the use manganese-based contrast agents is the relaxivity dependency to magnetic field strength. This limitation was offset by building a unique model at each magnetic field strength allowing the fabrication of magnetic field strength specific material for MRI phantom use. The significant parameters in the relaxation rate regression model were discussed and shown allowing the fabrication of MRI phantoms with predetermined relaxation properties. Finally, the contrast agents relaxivity dependency on magnetic field strength was examined through SBM theory illustrating the effects the gel structure may have on to the proton's magnetic environment (Figure 3-6).

3D gel dosimeters with a radiochromic tetrazolium salt and metal salts ($MnCl_2$ and $GdCl_3$) were prepared based on previous research and were irradiated at different doses to determine the effect to dose sensitivity. The metal salt concentrations did not alter the linear dose sensitivity in the dose range tested (Figure 3-10); however, sensitivity was reduced for gel dosimeters doped with $MnCl_2$. It was hypothesized that the $MnCl_2$ limits the reduction of tetrazolium salts to formazan. However, $GdCl_3$ doped gels did not experience the same reduction in sensitivity indicating that $GdCl_3$ may be incorporated into tetrazolium gel dosimeters without modifying sensitivity. However, as stated before $GdCl_3$ contains environmental and health concerns causing limitations if incorporated. It was also shown that the magnetic environment of $MnCl_2$ is not altered with the presence of either tetrazolium salts or formazans.

To better characterize the gel phantoms, mechanical and electrical tests were conducted. With the implementation of another design of experiments, a 2^3 multifactorial design of experiment model was able to determine the significant terms and characterize the effects by a regression model. The mechanical tests focused on compressive forces as a phantom could experience indentations during use. The results indicate that the base gels properties are able to withstand stress up to 30 kPa, and with the addition of crosslinking agents may form stronger gels or conversely gels with similar strength but lower gelling concentration. The type of crosslinking agent used can be manipulated for additional applications outside of mechanical tests with Li-formate acting as an oxidizing scavenger in dosimetry, or electrical conductivity with other monovalent metal salts. Results indicated that the effect of concentration for gellan gum, PG, and LiCl all were significant to the ultimate compressive stress and compressive modulus of the material (Figure 4-5). However, fracture strain was unable to be modelled likely requiring a more sophisticated modelling of parameters, but gellan gum concentration seem to have little to no affect on strain. The mechanical property models are useful for gels, but it fails to characterize the properties as the gel begins to flow and the is in the process of transitioning from a gel to a solution. However, gels with compressive modulus and strength larger than the base gel currently used at lowered gellan gum concentrations can be made with confidence as seen by the adjusted R^2 values.

The electrical properties were evaluated by dielectric spectroscopy by assuming the dielectric material acts similarly to an equivalent circuit with resistive and reactive components (Figure 2-4) allowing for the real and imaginary components of the electric permittivity to be calculated along with the conductivity of the dielectric materials. The existence of low and high-frequency errors occurs due to interface polarization between the electrodes and dielectric material and due to the copper circuitry having an inductance effect at high frequencies, respectively. However, at a constant frequency accurate comparison of electrical properties was made with little variability in the individual cells indicated by the adjusted R^2 value (>0.98) with the regression model. Greater accuracy could be achieved with increase sample size for each composition, low-frequency values could be calibrated prior for better evaluation, and a more sophisticated circuitry could be used to remove the inductance effects. The conductivity values at 100 kHz were evaluated to tissues (Figure 4-9), and with the mathematical model, tailorable conductivity values could be made.

5.2 Future directions

Additional experiments may provide further detail on the magnetic relaxation properties of gellan gum as a gel phantom. Both the gelling agent and PG concentrations will affect the magnetic properties of the hydrogel; and therefore, further studies to characterize their effect on the magnetic relaxation times could be conducted to expand the modelling of parameters. As the gels are crosslinked by monovalent salts used to modify conductivity, it may also be an interesting factor for modelling tissue equivalency for magnetic properties while also simulating similar electrical properties. Additional studies with ^{17}O NMR or EPR would confirm the magnetic relaxation properties developed in the NMRD model and provide a better fit to the modelling. Additionally, expanding the model to include the effects outside the inner sphere may create a more accurate model. The analysis of the NMRD profile may allow for low field strength measurements which is becoming an interesting field to explore because at larger magnetic field strengths the intrinsic difference in relaxation times between tissues is reduced limiting the contrast difference between tissues [1]. If the focus was placed at lower field strengths, one could exploit the inherent differences in tissues to produce enhanced contrast images and may implement the NMRD modeled hydrogels as a tool for comparison [2,3]. To properly develop gel dosimeters further research and experiments would be required to determine how the sensitivity is affected by the

additives chosen for magnetic, electrical, or mechanical modification. The tetrazolium salts effect to the mechanical and electrical properties could also be studied. Mechanical studies could be expanded to include large volume samples to coincide with tissue sized phantoms. Improving upon the electrical experiment setup could alleviate the low and high frequency errors discussed. Once corrected, the electric properties of the gel could be fitted by known mathematical models (Cole-Cole equations) to gain additional information of the electrical properties of the gel including the dielectric relaxation change and to build a predictive model of relative permittivity as a function of frequency [4–6]. Gels then doped with MRI contrast agents and radiochromic compounds for dosimetry could also be tested for mechanical and electrical tests to relate their properties together. Other research has focused gellan gum phantoms for MRI hyperthermia applications [7–9] due to the high thermal stability of gellan gum gels. Therefore, further studies into the thermal conductivity of the gels in addition to the electrical studies could relate the characteristics of the SPIONs within the gel environment when heated and could allow our system to be implemented in hyperthermia studies [10]. Therefore, further optimization and scale up production of the SPIONs may be of interest.

.

5.3 Bibliography

[1] Coffey AM, Truong ML, Chekmenev EY. Low-field MRI can be more sensitive than high-field MRI. J Magn Reson 2013;237:169–74. doi:10.1016/j.jmr.2013.10.013.

[2] Araya YT, Martínez-Santiesteban F, Handler WB, Harris CT, Chronik BA, Scholl TJ. Nuclear magnetic relaxation dispersion of murine tissue for development of T 1 (R 1) dispersion contrast imaging. NMR Biomed 2017;30:e3789. doi:10.1002/nbm.3789.

[3] Koenig S, Brown RI, Adams D, Emerson D, Harrison C. Magnetic field dependence of 1/T1 of protons in tissue. Invest Radiol 1984;9:76–81.

[4] Haemmerich D, Staelin ST, Tsai JZ, Tungjitkusolmun S, Mahvi DM, Webster JG. In vivo electrical conductivity of hepatic tumours. Physiol Meas 2003;24:251–60. doi:10.1088/0967-3334/24/2/302.

[5] Yuan Y, Wyatt C, MacCarini P, Stauffer P, Craciunescu O, MacFall J, et al. A heterogeneous human tissue mimicking phantom for RF heating and MRI thermal monitoring verification. Phys Med Biol 2012;57:2021–37. doi:10.1088/0031-9155/57/7/2021.

[6] Yoshida A, Kato H, Kuroda M, Hanamoto K, Yoshimura K, Shibuya K, et al. Development of a phantom compatible for MRI and hyperthermia using carrageenan gel - Relationship between T1and T2values and NaCl concentration. Int J Hyperth 2004;20:803–14. doi:10.1080/0265673042000199268.

[7] Wu H, Song L, Chen L, Zhang W, Chen Y, Zang F, et al. Injectable Magnetic Supramolecular Hydrogel with Magnetocaloric Liquid-Conformal Property Prevents the Post-operative Recurrence in a Breast Cancer Model. Acta Biomater 2018. doi:10.1016/j.applthermaleng.2010.04.033.

[8] Tay ZW, Chandrasekharan P, Chiu-Lam A, Hensley DW, Dhavalikar R, Zhou XY, et al. Magnetic Particle Imaging-Guided Heating in Vivo Using Gradient Fields for Arbitrary Localization of Magnetic Hyperthermia Therapy. ACS Nano 2018;12:3699–713. doi:10.1021/acsnano.8b00893.

[9] Ma M, Zhang Y, Gu N. Estimation the tumor temperature in magnetic nanoparticle hyperthermia by infrared thermography: Phantom and numerical studies. J Therm Biol 2018;76:89–94. doi:10.1016/j.jtherbio.2018.07.004.

[10] Kandasamy G, Sudame A, Luthra T, Saini K, Maity D. Functionalized Hydrophilic Superparamagnetic Iron Oxide Nanoparticles for Magnetic Fluid Hyperthermia Application in Liver Cancer Treatment. ACS Omega 2018;3:3991–4005. doi:10.1021/acsomega.8b00207.

Appendices

Supplementary Information

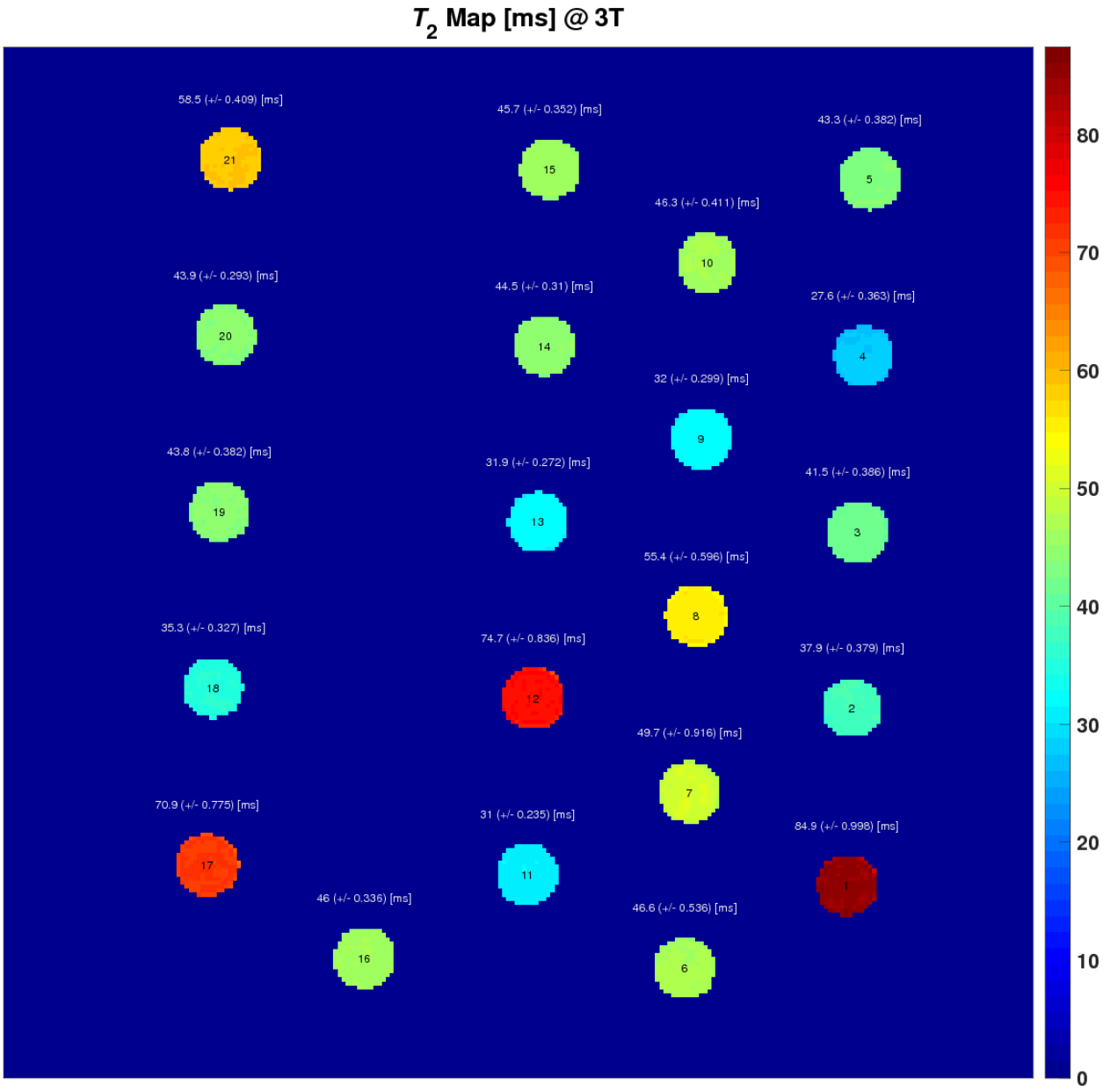

Appendix A: T_2 map at 3 T after eroding one voxel around the gel region of interest (ROI) boundary

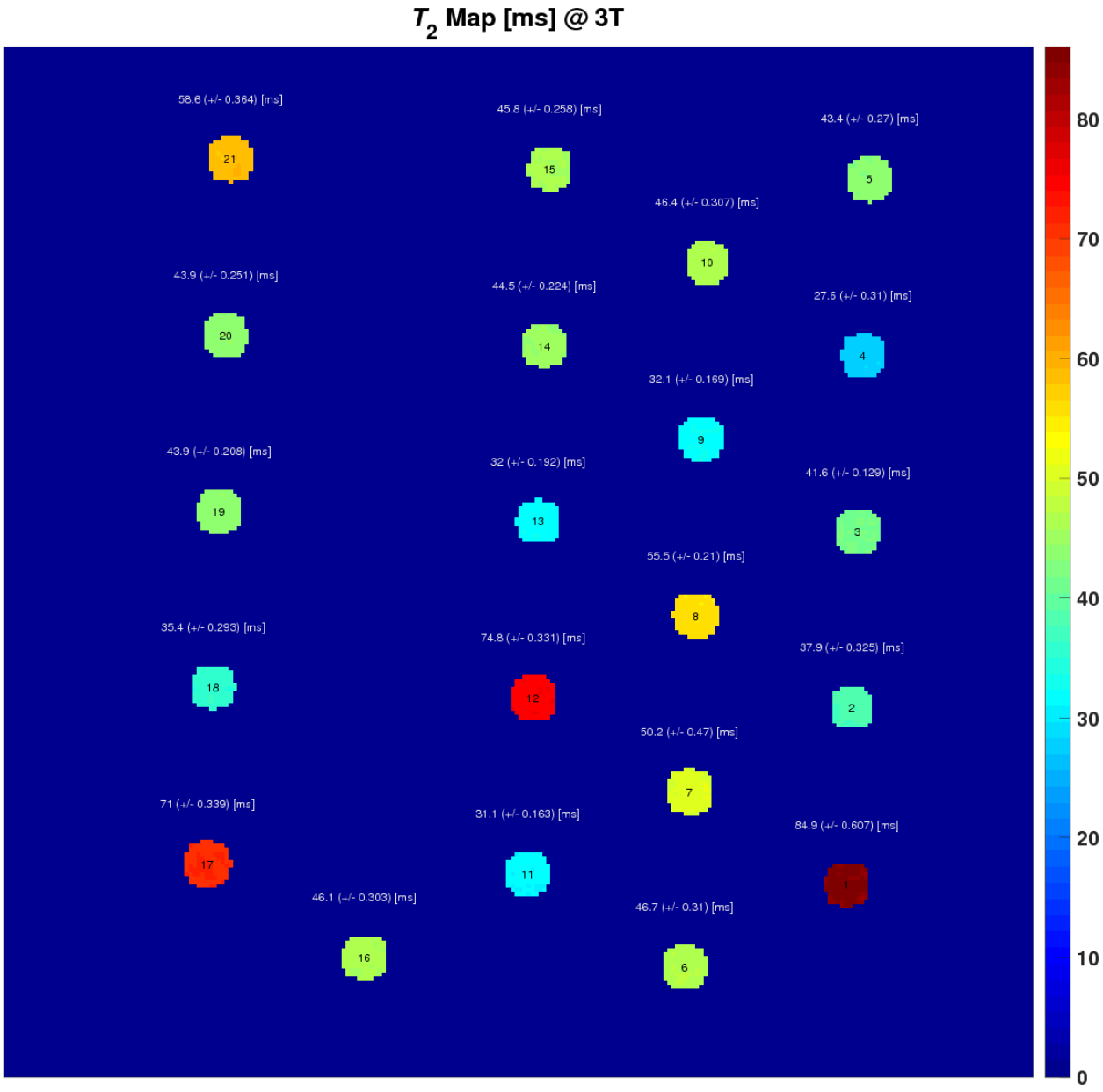

Appendix B: T_2 map at 3 T after eroding three voxels around the gel ROI boundary

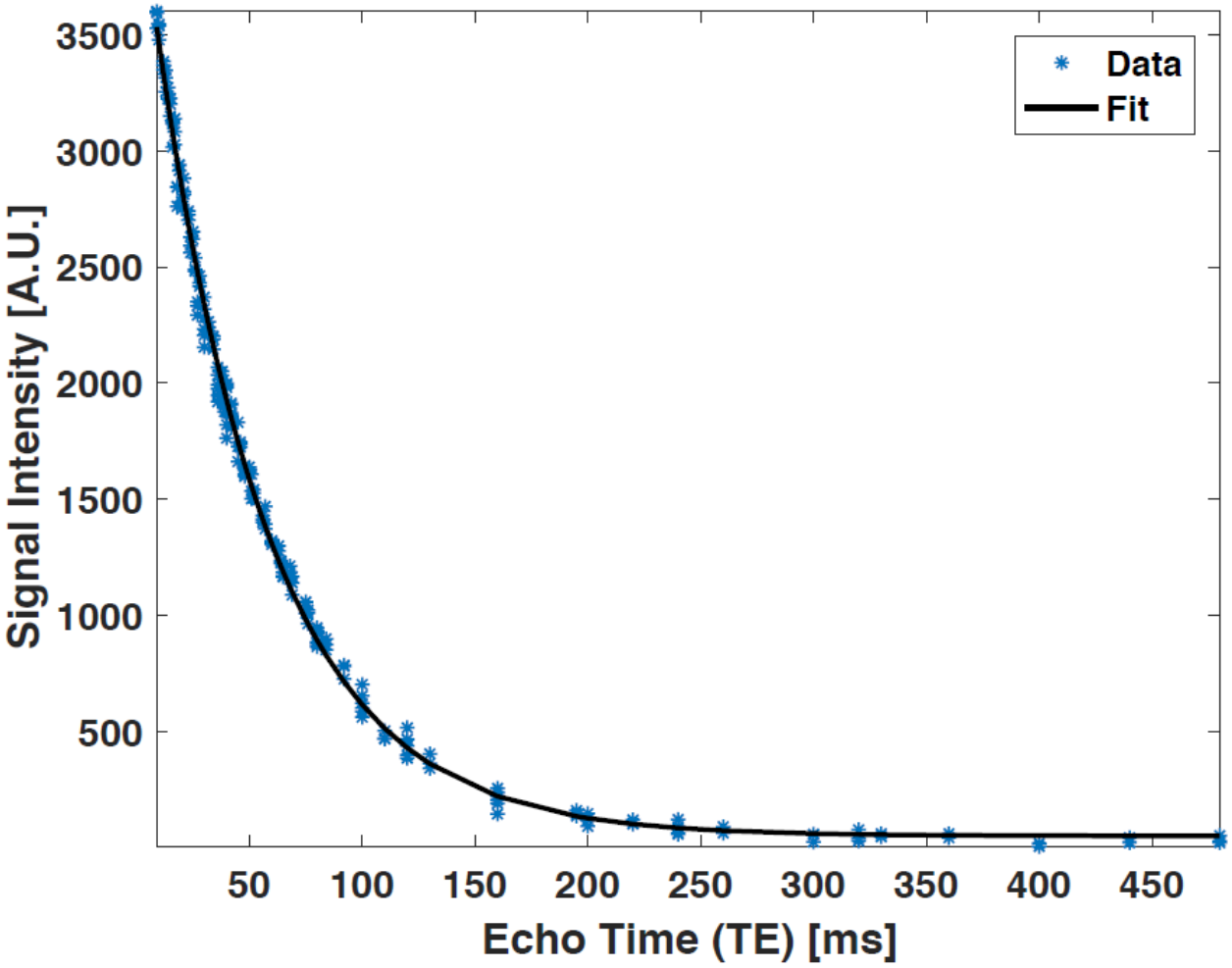

Appendix C: T_2 decay curve with fit

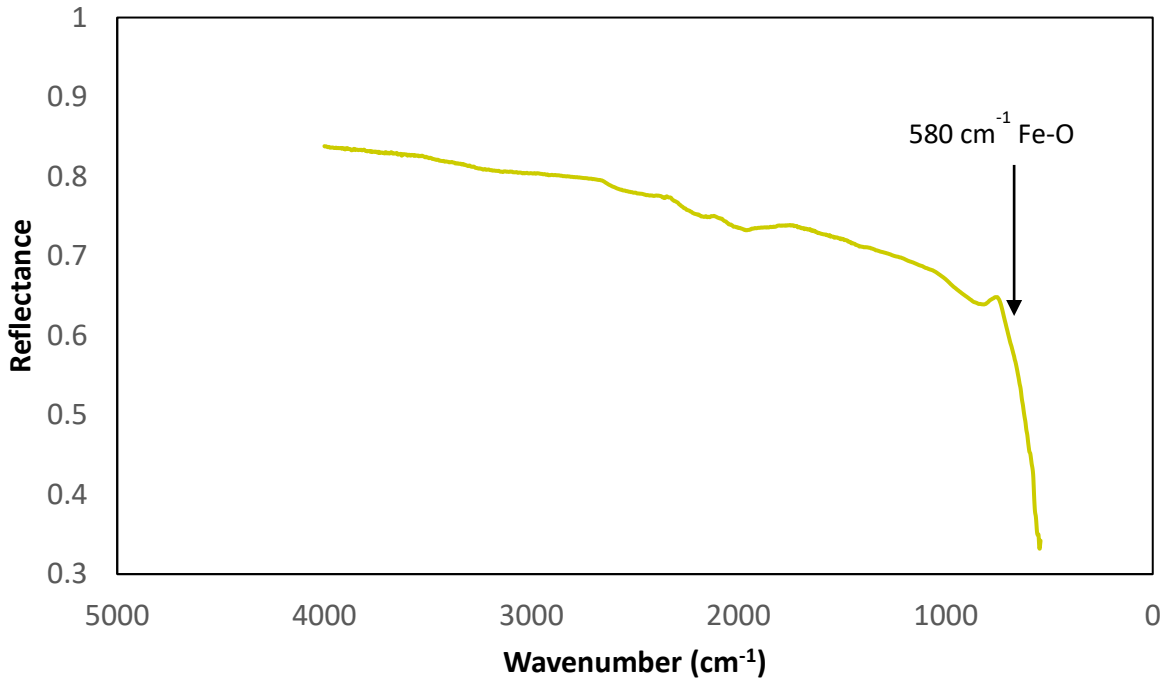

Appendix D: FTIR of dried powder SPIONs

Appendix E: P-values for longitudinal relaxation rates (R_1) for $MnCl_2$

Field Strength	$a_{1,1,0}$	$a_{1,1,1}$	$a_{1,1,2}$	$a_{1,1,3}$	$a_{1,1,4}$	$a_{1,1,5}$
3	<0.001	<0.001	0.011	0.553	0.271	0.48
1.5	<0.001	<0.001	0.018	0.124	0.301	0.357
1.0009	<0.001	<0.001	0.344	0.009	0.924	0.221
0.75691	<0.001	<0.001	0.293	0.041	0.553	0.244
0.56715	<0.001	<0.001	0.821	0.295	0.117	0.942
0.42505	<0.001	<0.001	0.646	0.526	0.163	0.3
0.31851	<0.001	<0.001	0.214	0.814	0.672	0.337
0.23863	<0.001	<0.001	0.28	0.258	0.708	0.493
0.17885	<0.001	<0.001	0.161	0.377	0.924	0.399
0.13403	<0.001	<0.001	0.287	0.136	0.7	0.649
0.10049	<0.001	<0.001	0.062	0.86	0.427	0.416
0.075277	<0.001	<0.001	0.195	0.15	0.6	0.518
0.056393	<0.001	<0.001	0.121	0.922	0.756	0.305
0.042268	<0.001	<0.001	0.058	0.71	0.877	0.209
0.031677	<0.001	<0.001	0.14	0.818	0.906	0.503
0.023729	<0.001	<0.001	0.086	0.658	0.634	0.396
0.017795	<0.001	<0.001	0.07	0.513	0.646	0.259
0.013326	<0.001	<0.001	0.062	0.478	0.952	0.145
0.009985	<0.001	<0.001	0.116	0.882	0.696	0.307
0.00748	<0.001	<0.001	0.058	0.502	0.578	0.399
0.0056074	<0.001	<0.001	0.073	0.396	0.626	0.368
0.0042075	<0.001	<0.001	0.125	0.425	0.636	0.531
0.0031574	<0.001	<0.001	0.065	0.455	0.942	0.366
0.0023638	<0.001	<0.001	0.149	0.283	0.879	0.408
0.0017659	<0.001	<0.001	0.062	0.061	0.414	0.313
0.0013252	<0.001	<0.001	0.044	0.032	0.224	0.265
0.00099331	<0.001	<0.001	0.062	0.106	0.981	0.258
0.00074206	<0.001	<0.001	0.061	0.14	0.799	0.286
0.00055583	<0.001	<0.001	0.137	0.142	0.973	0.326
0.00041615	<0.001	<0.001	0.092	0.084	0.762	0.308
0.00031372	<0.001	<0.001	0.02	0.02	0.787	0.157
0.00023315	<0.001	<0.001	0.16	0.161	0.726	0.261

Appendix F: P-values for transverse relaxation rates (R_2) for $MnCl_2$

Field Strength	$a_{2,1,0}$	$a_{2,1,1}$	$a_{2,1,2}$	$a_{2,1,3}$	$a_{2,1,4}$	$a_{2,1,5}$
3	<0.001	0.001501	0.001	0.115	0.852	0.595
1.5	<0.001	0.004608	0.001	0.1	0.959	0.619

Appendix G: P-values for longitudinal relaxation rates (R_1) for $GdCl_3$

Field Strength	$a_{1,2,0}$	$a_{1,2,1}$	$a_{1,2,2}$	$a_{1,2,3}$	$a_{1,2,4}$	$a_{1,2,5}$
3	<0.001	5.7865E-06	0.047	0.123	0.39	0.881
1.5	<0.001	1.82762E-05	0.039	0.099	0.532	0.977
1.0009	<0.001	7.81475E-06	0.111	0.031	0.293	0.981
0.75691	<0.001	5.51628E-06	0.059	0.015	0.187	0.914
0.56715	<0.001	4.05091E-05	0.208	0.103	0.381	0.984
0.42505	<0.001	2.22426E-05	0.162	0.07	0.331	0.974
0.31851	<0.001	1.9788E-05	0.152	0.083	0.345	0.921
0.23863	<0.001	5.37311E-06	0.083	0.031	0.337	0.904
0.17885	<0.001	1.35446E-05	0.185	0.139	0.462	0.963
0.13403	<0.001	8.80855E-06	0.165	0.121	0.405	0.936
0.10049	<0.001	2.03898E-05	0.24	0.126	0.471	0.968
0.075277	<0.001	8.48963E-06	0.183	0.104	0.275	0.962
0.056393	<0.001	6.26222E-06	0.172	0.085	0.285	0.971
0.042268	<0.001	1.52678E-06	0.076	0.035	0.257	0.99
0.031677	<0.001	1.2222E-05	0.211	0.133	0.473	0.983
0.023729	<0.001	1.02319E-05	0.227	0.178	0.477	0.99
0.017795	<0.001	7.85899E-06	0.197	0.09	0.29	0.989
0.013326	<0.001	5.36343E-06	0.146	0.085	0.274	0.904
0.009985	<0.001	4.90277E-06	0.153	0.093	0.268	0.974
0.00748	<0.001	5.05879E-06	0.157	0.129	0.358	0.992
0.0056074	<0.001	3.6092E-06	0.157	0.139	0.203	0.933
0.0042075	<0.001	1.2566E-05	0.253	0.357	0.742	0.964
0.0031574	<0.001	2.69376E-06	0.141	0.201	0.205	0.999
0.0023638	<0.001	1.23052E-05	0.297	0.551	0.672	0.91
0.0017659	<0.001	1.12969E-05	0.308	0.588	0.755	0.941
0.0013252	<0.001	5.07581E-06	0.271	0.826	0.712	0.948
0.00099331	<0.001	1.51338E-06	0.15	0.39	0.306	0.94
0.00074206	<0.001	2.72992E-06	0.2	0.644	0.335	0.998
0.00055583	<0.001	3.77747E-06	0.357	0.803	0.625	0.961
0.00041615	<0.001	2.19732E-06	0.293	0.816	0.582	0.959
0.00031372	<0.001	2.02045E-06	0.246	0.907	0.386	0.933
0.00023315	<0.001	1.57389E-06	0.304	0.328	0.698	0.969

Appendix H: P-values for transverse relaxation rates (R_2) for $GdCl_3$

Field Strength	$a_{2,2,0}$	$a_{2,2,1}$	$a_{2,2,2}$	$a_{2,2,3}$	$a_{2,2,4}$	$a_{2,2,5}$
3	4.21E-07	0.009027	<0.001	0.54	0.028	0.068
1.5	6.38E-07	0.006682	<0.001	0.804	0.033	0.071

Appendix I: P-values for mechanical tests

Compositions	Stress	Strain	Compressive modulus
(Intercept)	<0.001	<0.001	<0.001
gn	<0.001	0.75	<0.001
PG	<0.001	<0.001	<0.001
ion	<0.001	<0.001	<0.001
gn-PG	0.116	0.016	0.012
gn-ion	0.339	0.598	<0.001
PG-ion	0.018	0.088	0.582
gn-PG-ion	0.993	0.006	0.157

Appendix J: P-values for electrical measurement

Compositions	Conductivity
(Intercept)	<0.001
gn	0.624
PG	0.039
ion	<0.001

Appendix K: Copyright permission

ELSEVIER LICENSE
TERMS AND CONDITIONS

Dec 13, 2018

This Agreement between Pawel Brzozowski ("You") and Elsevier ("Elsevier") consists of your license details and the terms and conditions provided by Elsevier and Copyright Clearance Center.

License Number	4487271298426
License date	Dec 13, 2018
Licensed Content Publisher	Elsevier
Licensed Content Publication	Coordination Chemistry Reviews
Licensed Content Title	Small molecular gadolinium(III) complexes as MRI contrast agents for diagnostic imaging
Licensed Content Author	Kannie Wai-Yan Chan,Wing-Tak Wong
Licensed Content Date	Sep 1, 2007
Licensed Content Volume	251
Licensed Content Issue	17-20
Licensed Content Pages	24
Start Page	2428
End Page	2451
Type of Use	reuse in a thesis/dissertation
Portion	figures/tables/illustrations
Number of figures/tables/illustrations	1
Format	electronic
Are you the author of this Elsevier article?	No
Will you be translating?	No
Original figure numbers	Figure 1
Title of your thesis/dissertation	Development of Tissue Equivalent Materials for Medical Physics Applications
Expected completion date	Dec 2018
Estimated size (number of pages)	90
Requestor Location	Pawel Brzozowski

Curriculum Vitae

Name: Pawel Brzozowski

Post-secondary Education and Degrees:

The University of Western Ontario
London, Ontario, Canada
Master of Engineering Science (M.E.Sc)
Biomedical Engineering, Biomaterials
2017 - 2019

The University of Western Ontario
London, Ontario, Canada
Bachelor of Engineering Science (B.E.Sc)
Chemical and Biochemical Engineering
2012 - 2016

Honours and Awards:

11th Annual Capstone Competition in the Sarnia-Lambton Research Park
First Place in Specialty Chemicals
2016

Dean's Hour List
The University of Western Ontario
2013 - 2016

Western Scholarship of Excellence Admission Scholarship for Academic Recognition
The University of Western Ontario
2012

Related Work Experience

Teaching Assistant
Chemical Engineering courses
The University of Western Ontario
2017 - 2018

Publications:

Pawel Brzozowski, Kalin I. Penev, Francisco M. Martinez, Timothy J. Scholl, and Kibret Mequanint. Gellan Gum-based Gels with Tunable Relaxation Properties for MRI Phantoms. *Magnetic Resonance Imaging.* 57, 40-49; 2019.